Delft University of Technology

Stall and vortex induced vibrations in large wind turbines

Master of Science thesis

By

M.J.T. (Max) Bouwmeesters

Student number: 4545788
To be defended on: November 28th, 2023

Committee member	Role	Affiliation
Prof. Dr. Ir. C.J. (Carlos) Simao Ferreira	Chair	TU Delft
Dr. Ir. J. (Jurij) Sodja	Examiner	TU Delft
Dr. Ir. W. (Wei) Yu	Supervisor	TU Delft
Dr. Ir. K. (Koen) Boorsma	Supervisor	TNO

Acknowledgements

Despite almost all meetings having been online, I am very grateful for the guidance of my supervisors who were always ready to help out with problems and give me weekly feedback. Firstly, I would like to express my gratitude to dr. Ir. Koen Boorsma. I thank him for giving me the opportunity to work on this research project at TNO and for his guidance and feedback during the thesis. I also want to thank Dr. Ir. Wei Yu for her great guidance during this project. Besides the greatly insightful comments regarding SVIV, I received great support from her when I was struggling mentally during the thesis. For this, I am greatly thankful for her thoughtful guidance.

Apart from my supervisors, I am also very thankful for the support from my fellow colleagues at TNO, who were willing to help out with any questions I might have. Special thanks to Nirav with whom I've worked together since my internship before the thesis. He was a great friend, both when discussing our theses and outside of the office, for example, while playing tennis. Lastly, I would like to thank my friends from my studies for some, sometimes much-needed, distraction from my thesis. And my parents for all of their support throughout this entire process.

Abstract

Wind turbines experience a wide variety of load cases, both when in operation and when parked. While a turbine in operating conditions often experiences larger loads than in parked conditions, uniquely large inflow angles may occur in parked conditions resulting in less well-understood aeroelastic conditions. Vibrations under these conditions are referred to as stall and vortex-induced vibrations (SVIV). While there has been some success in simulating these conditions, there has been a lack of experimental studies in the literature.

To address this gap, this study analyses the experimental data obtained from a 3.8 MW research wind turbine. This turbine was equipped with strain gauges at the root of 2 blades and in the tower, as well as pressure sensors on one blade and accelerometers in the nacelle and tower. Several experiments were performed with a focus on simulating various conditions where SVIV may occur. This included pitch traverses of a single blade, yaw traverses, and a traverse of the azimuth angle at a yaw angle of 90 degrees to determine the effect of the inclination angle.

Severe stall-induced vibrations were identified at the yaw angle of 110 degrees, when a single blade pointing up in the sky was pitched 180 degrees, and the other two blades were in vane positions at 85 degrees pitch. The severity of these vibrations strongly varied with the wind speed, at an average wind speed of 19.5 m/s the test needed to be stopped early for the safety of the wind turbine, while at 16.6 m/s, the vibrations appeared to reach a limit that was still considered to be safe. The first tower mode experienced the most severe increase in magnitude during these conditions of SIV. In other conditions, no severe case of SIV was identified. However, under several conditions, smaller increases in vibration magnitude were identified. These are likely the result of slightly reduced aerodynamic damping.

No vortex shedding was identified in the data obtained from these experiments. This means that the tested turbine/blade design either did not experience vortex shedding or that it simply could not be measured by the installed instruments. Having pressure sensors installed in multiple locations along the blade would likely help in identifying vortex shedding for future experiments.

Simulations from the experimental conditions were performed using the aeroelastic software PHATAS together with the aero module from ECN (now part of TNO). This simulation used beam-based structural modeling with either a BEM or free vortex wake aerodynamic model. These simulations confirmed the need for realistic turbulent inflow conditions and the need for a good dynamic stall model. However, the structural model failed to simulate all the natural frequencies with the expected accuracy. This should be improved upon for future use of this structural model in parked conditions.

Contents

Nomenclature

α	Angle of Attack
$\dot{m}$	Mass flow rate
ρ	Density
θ	Phase angle difference between the oscillations normal and parallel to the flow
ζ	Structural damping ratio
A	Amplitude
a	Axial induction velocity factor
a'	Tangential induction velocity factor
AoA	Angle of Attack
b	Damping term
b_a	Added damping term
BEM	Blade Element Momentum
c	Chord length
C_D	Drag coefficient
C_L	Lift coefficient
c_{xy}	Damping coefficient in direction of x due to the influence of motion in the direction of y
D	Diameter
DLC	Design Load Case
DTU	Technical University of Denmark
ECN	Energy research center of the Netherlands
$Edgewise$	The direction in the local blade's cross-section parallel to the chord
f	Frequency at which the structure is vibrating
f_n	Natural frequency of structure
f_v	Vortex shedding frequency
FA	Fore-Aft direction of the turbine (also referred to as the normal direction)
FFT	Fast Fourier Transform
$Flapwise$	The direction in the local blade's cross-section normal to the chord
FVW	Free Vortex Wake
I_{ils}	Integral lenght scale of the flow

I_{rotor}	Moment of inertia of the rotor at the shaft
IEC	International Electrotechnical Commission
k	Spring constant
L	Length
m	Mass
m_a	Added mass
PSD	Power Spectral Density
q_{shaft}	Torsional stiffness of the shaft
Re	Reynolds number
RMS	Root Mean Squared
SIV	Stall Induced Vibrations
Sp	Schewe parameters
SS	Side-Side direction of the turbine (also referred to as the lateral direction)
St	Strouhal number
$SVIV$	Stall and Vortex Induced Vibrations
Ti	Turbulence intensity
$TIADE$	Turbine Improvements for Additional Energy)
TNO	Netherlands Organisation for Applied Scientific Research
V	Velocity
V_r	Reduced velocity
$Vane$	Vane position refers to weather vanes, i.e. pitched at an angle of least resistance (85)
VIV	Vortex Induced Vibrations
W	Local inflow velocity

List of Figures

List of Tables

Chapter 1

Introduction

With the world under an ever bigger threat of global warming, it has been evident for quite a while that we need to transition to renewable sources of electricity. Wind energy will have to play a crucial role in the energy production of the future. Over the past few decades, wind turbines have shown a trend to become increasingly larger. This resulted in very long and slender blades. One of the structural consequences of these long and slender blades is that they become more sensitive to vibrations at lower frequencies.

One of the critical load cases for wind turbines is found during standstill or idle conditions. In these conditions, turbine blades may experience high angles of attack where stall and vortex shedding can occur. This can cause the loads on a wind turbine blade to have a periodic variation, which in turn causes oscillations. These vibrations are due to two distinct phenomena: Stall induced vibrations (SIV) and vortex induced vibrations (VIV). This project aims to investigate both phenomena and will refer to them together as SVIV. A visualization of a wind turbine suffering from this is represented in Figure 1.1. This phenomenon will be analyzed by processing and interpreting the bending moment and pressure data obtained from a large testing turbine in parked conditions.

When certifying a wind turbine according to the IEC standard, yaw misalignment of up to ±180° should be taken into account[1], but depending on the model used for this analysis SVIV may or may not become problematic[2]. This phenomenon has only become problematic with the increasing size of wind turbines through the years, resulting in the need for more accurate modeling of SVIV. Besides analyzing the force oscillations in an actual wind turbine, this project will therefore also aim to simulate these conditions and discuss their performance.

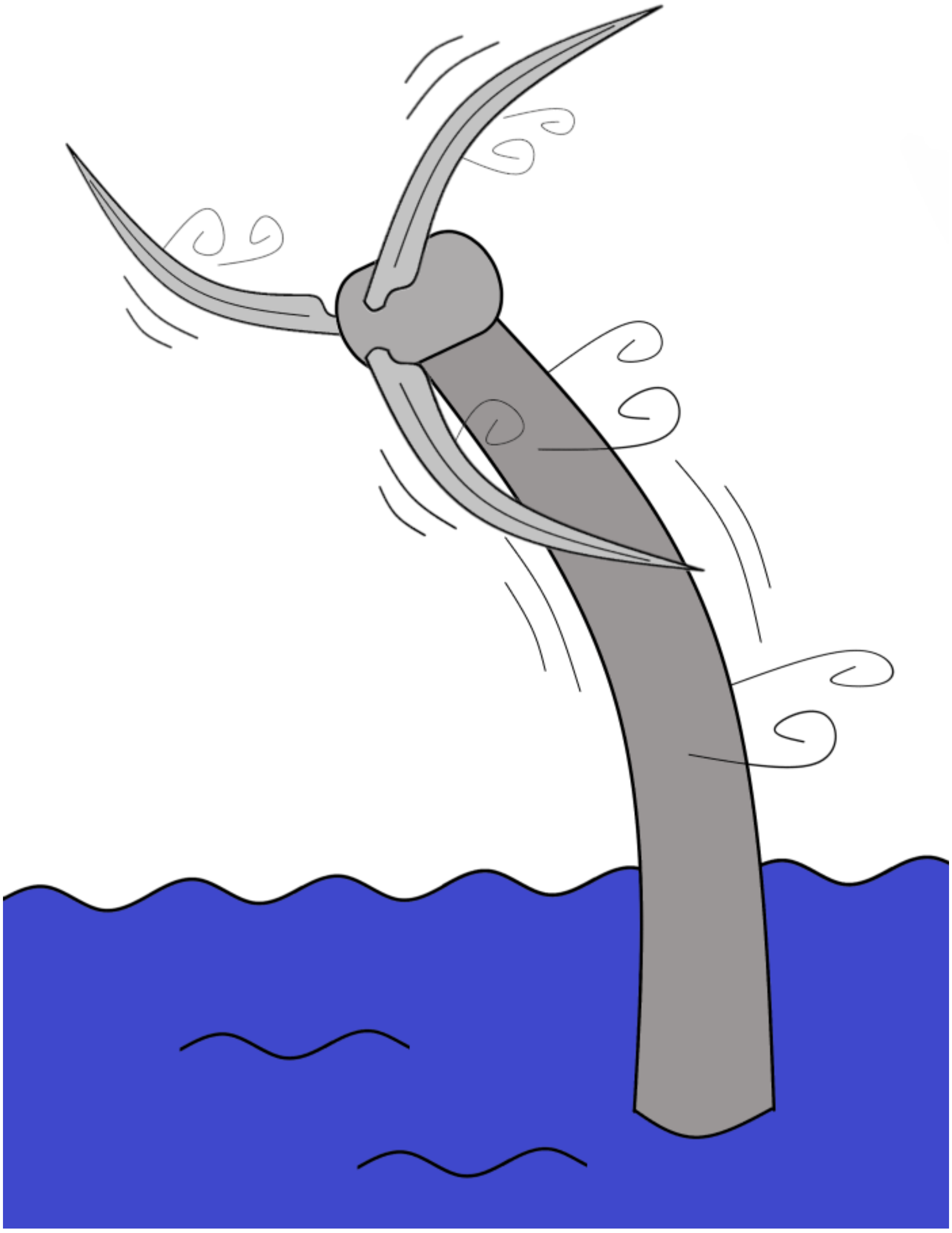

Figure 1.1: Visualization of a turbine suffering from SVIV

Chapter 2

Literature study

Before performing any experiments to gain a better understanding of SVIV, a general understanding should be obtained from the literature. After gaining insight into the phenomenon of SVIV and understanding the state of the art, a gap in current understanding can be identified. Research questions have been formed based on this gap in the state of the art.

2.1 Vortex induced vibrations

Vortex Induced Vibration (VIV), is "the aero-elastic instability a structure undergoes when the cross-flow oscillating lift force, due to shedding of vortices, resonates with one of the system's natural frequencies" [3]. This phenomenon is not unique to wind turbines, as it can happen to almost any structure. Some examples where it may cause problems are: bridges, transmission lines, aircraft control surfaces, offshore structures, tethered structures, mooring cables, and other hydro-dynamic applications[4].

In the past few decades, most research has been performed on circular cylinders with limited degrees of freedom in a three-dimensional separated flow, dominated by large-scale vortical structures [4]. The degrees of freedom have mostly been limited from 6 to 1 or sometimes 2, due to the inherent complexity of this self-induced motion.

Parameter dependencies

When discussing VIV, there are 3 important frequencies needed to describe the behavior. First of all, there is the actual frequency at which the body is vibrating (f). Then there is the vortex shedding frequency (f_v). This frequency describes the rate of vortex shedding that would have happened if the structure is not vibrating due to the flow. Lastly, there is the natural frequency of the structure itself (f_n). There does not seem to be a singular consensus within academia on how to refer to these vibrations, hence you may find that some of the cited figures use different naming conventions.

Some of the other non-dimensional parameters used to describe a VIV problem are the Strouhal number (St), the Reynolds number (Re), the reduced velocity (V_r), and the reduced amplitude ($\frac{A}{D}$) where D is the diameter for a cylinder. $\frac{A}{D}$ is generally an unknown value of interest, while the other parameters mentioned are defined in equations 2.1,2.2 and 2.3 below.

$$St = \frac{f_v D}{V} \qquad (2.1) \qquad\qquad Re = \frac{VD}{v} \qquad (2.2) \qquad\qquad V_r = \frac{V}{f_n D} \qquad (2.3)$$

While these are the most common nondimensional parameters to describe a problem, they fail to describe everything about the VIV problem. A more comprehensive dimensional analysis can be performed on this problem. Equation 2.4 shows the result of such an analysis performed for a cylinder [4]. Where ζ is the structural damping ratio, ρ_f is the fluid density, U is the flow velocity, D is the cylinder diameter, L is the cylinder length, k is the spring constant, k_s is the mean roughness height of the surface, m is the mass, ε_t is the turbulence intensity, I_{ils} is the integral length scale of the flow and Sp are the Schewe parameters. The Schewe parameters encompass all parameters uncontrollable in an experiment including the unknowable ones. Re_{sl} is the Reynolds number where the transition eddies in the free shear layer disappear and Re_{cr} is the Critical Reynolds number.

$$\frac{A}{D} = \left\{ \begin{array}{l} \zeta, \frac{\rho_f U D}{\mu_f}, \frac{L}{D}, \frac{4m}{\rho_f \pi L D^2}, \frac{D}{U}\left(\frac{k}{m}\right)^{1/2}, Re_{sl}, \\ Re_{cr}, \frac{D}{U_0^2}\frac{dU}{dt}, \frac{D}{U}\frac{dU}{dy}, \frac{D}{dy}, \varepsilon_t, \frac{k_s}{D}, \frac{I_{ils}}{D}, Sp \end{array} \right. \tag{2.4}$$

Example for 1 degree of freedom

As an example, consider the case with 1 degree of freedom perpendicular to the flow for a flexibly mounted rigid cylinder. Equation 2.5 is the differential equation describing this situation. The Force on the right-hand side is due to the shed vortices and is dependent on time, flow conditions, and the motion of the cylinder.

$$m\ddot{y} + b\dot{y} + ky = F\left(t, y, \dots\right) \tag{2.5}$$

If both the motion and forces are assumed to be sinusoidal (which is a rather large simplification), then the forces can be simplified to a so-called added mass (m_a) and added damping (b_a) term as shown in Equation 2.6. Despite looking like a simple equation to solve, the added mass and damping terms are dependent on many factors and aren't simple to determine. Various methods have been developed to better model this added mass and damping.

$$(m + m_a)\ddot{y} + (b + b_a)\dot{y} + ky = 0 \tag{2.6}$$

Comparison to 2 degrees of freedom

1 degree of freedom doesn't show the full picture, however, as there are other motions present as well. The largest vibrations are usually seen in the orthogonal direction of the flow, but there can also be a vibration present in the direction of the flow. This motion is usually of lower amplitude than the orthogonal direction and has a frequency twice as high. Figure 2.1 shows the characteristic figure 8 movement which follows from including the second degree of freedom. Here, θ is the phase angle between the oscillation parallel and perpendicular to the flow.

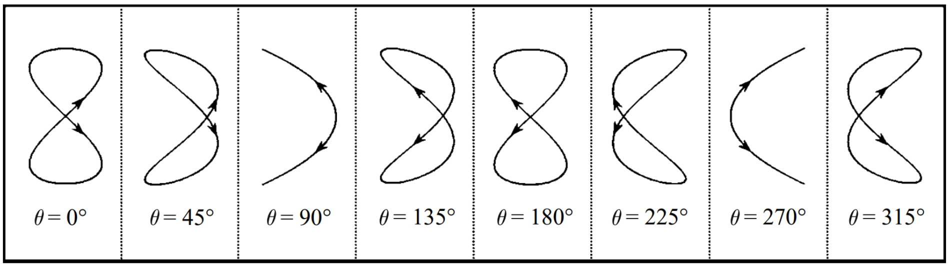

Figure 2.1: Modes of motion for a cylinder with 2 degrees of freedom in uniform free stream, as a function of the phase angle θ with flow from left to right. [5]

While the frequency of the flow-wise vibration is typically twice the orthogonal vibration, this may not be the case at the lowest reduced velocities where VIV can happen. Under these conditions, it has been identified that both frequencies may match each other [5]. Regardless, for most of the reduced velocity range of interest for a cylinder, it is fair to assume the flow-wise frequency to be twice as high as for the transverse oscillation.

Vortex shedding patterns

The oscillations are typically induced due to the systematic shedding of vortices around a cylinder. The type of vortex shedding is however strongly dependent on the flow conditions. A lot of the possible periodic vortex shedding patterns have been identified in the past. Some of the most commonly seen vortex shedding patterns are listed below.

2S 2 singular vortices shed per cycle

2P 2 pairs of counter-rotating vortices shed per cycle

P+S 1 pair of counter-rotating and 1 single vortex

2C 2 pairs of co-rotating vortices shed per cycle

2T 2 triplets of vortices shed per cycle

Figure 2.2 shows an example where the vortex shedding type was mapped for a cylinder in varying reduced velocities.

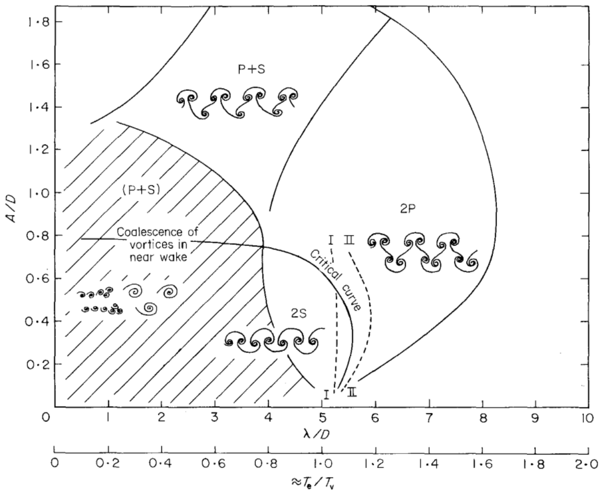

Figure 2.2: Mapping of vortex shedding patterns for a cylinder under varying reduced velocity from 1988. [6]

Interestingly, It has been found that under certain conditions, multiple vortex shedding patterns were stable. These different vortex patterns can exert very different loads on the cylinder. Which pattern would happen is highly dependent on the history of conditions right before it. These different conditions are usually referred to as an upper and lower branch, and sometimes there is even a middle branch.

Lock-in phenomena

The frequency f at which the body will vibrate is closely related to the vortex shedding frequency f_v and the natural frequency of the body f_n. At low reduced velocities, the body tends to vibrate with the same frequency as the steady vortex shedding frequency f_v. The amplitude of said vibration will be very small. The vortex shedding frequency increases as V_r increases, and when assuming a constant Strouhal number, this happens with a linear trend.

Once f_v approaches the natural frequency, the body will start to vibrate with the same frequency. Oscillating with the natural frequency naturally also comes with a higher amplitude. The body will however continue to vibrate at this frequency even as the reduced velocity is increased further. This continues until a certain velocity after which the frequency of the body will return to the vortex shedding frequency and the amplitude will again reduce. This phenomenon of continued vibration near the natural frequency for a range of reduced velocities is known as lock-in.

Figure 2.3 presents lock-in nicely for a cylinder in air at a Reynolds number of 10^4 till $5 * 10^4$. The circles represent the measurements for f/f_n and show the lock-in phenomena between U of 0.85 and 1.15, which is equivalent to V_r of about 5.25 till 7.25. The amplitude during lock-in follows two different branches, depending on whether the flow was altered in an increasing or decreasing trend. This clearly shows that the vortex shedding pattern is dependent on the past and that multiple patterns at the same parameters are possible.

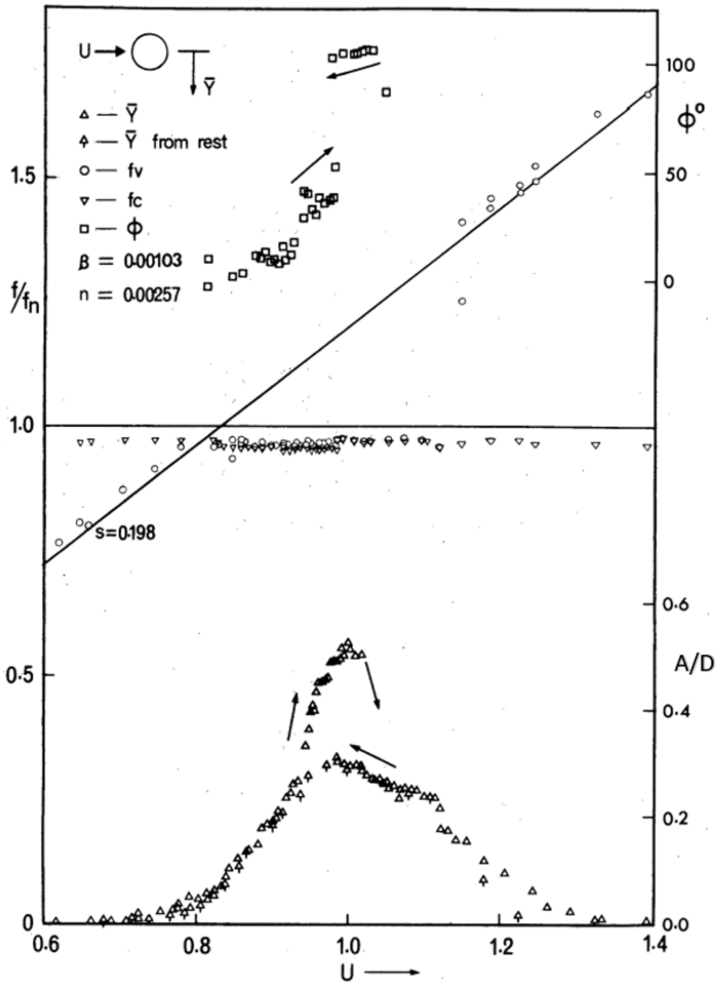

Figure 2.3: Response of a spring mounted cylinder in air at Reynolds number 10^4 till $5 * 10^4$ [7]

Limit cycle

While vortex shedding can result in induced vibrations, the amplitude of these vibrations generally does not increase indefinitely. Instead, the amplitude resulting from the vortices tends towards a limit as time goes to infinity. In mathematics, this phenomenon for a system with 2 degrees of freedom is known as a limit cycle

The aerodynamic forces can be modeled as a limit cycle, but this limit is usually not reached due to structural damping in the system. Hence the actual limit usually has a lower amplitude. It is possible that there exist multiple different limit cycles for a system. Which limit cycle is approached then depends on the initial conditions on how the vibration is triggered.

VIV for different Reynolds numbers

VIV experiments have been performed for many different flow conditions throughout the last few decades. However, most experiments have been performed at relatively low Reynolds numbers. These experiments are in the sub-critical regime where the flow has not yet transitioned to a turbulent state before separating. Some research does however exist to compare VIV of different Reynolds numbers.

Figure 2.4 shows how the Strouhal number of a circular cylinder varies under an increasing Reynolds number. Here the region between the Reynolds numbers of $2 * 10^5$ and $2 * 10^6$ is the transition region after which the flow is considered super-critical.

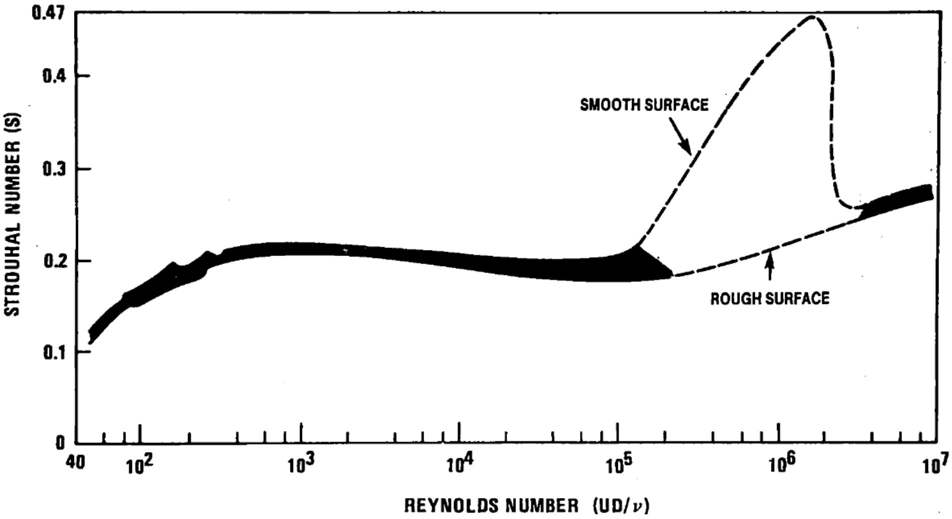

Figure 2.4: Strouhal number versus the Reynolds number for a circular cylinder. [8]

This variation of the Strouhal number as the Reynolds number is varied depends heavily on the geometry of the body. This is depicted for a variety of bodies and ranges of Reynolds numbers in Figure 2.5. Hence, one can not simply correlate the results of a cylinder and an airfoil when determining the variation with respect to the Reynolds number.

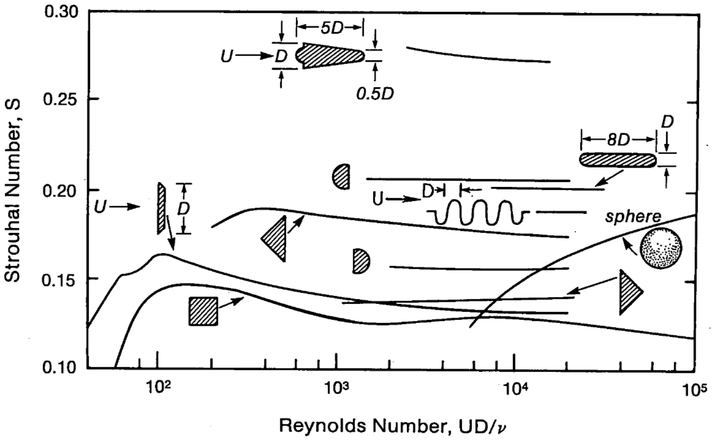

Figure 2.5: Strouhal number versus the Reynolds number for several different non-circular sections. [8]

For airfoils under a high angle of attack (30 to 130 degrees) within a super-critical flow, the Strouhal number was found to remain almost constant. For the Strouhal number, the chord segment normal to the flow is used as the length as shown in Equation 2.7. While the Strouhal number is predicted to remain close to constant for an airfoil, different airfoils may stay at different Strouhal numbers. Typically, this Strouhal number will be somewhere between 0.15 and 0.2 for an airfoil. It also holds true for the negative equivalent of these angles that the Strouhal number will remain almost constant. However, the constant Strouhal number may not be the same for positive and negative angles, depending on the shape of the airfoil. Multiple different Reynolds numbers were tested for these angles of attack, which all resulted in the same Strouhal numbers. Hence it is safe to assume that for high angles of attack and super-critical conditions, the Strouhal number of an airfoil is independent of the Reynolds numbers

$$St = \frac{f_v c \sin\alpha}{V} \tag{2.7}$$

Forced versus free vibration

The many different variations of vortex shedding which depend heavily on the flow conditions and the history of flow and movement result in a very complicated situation to analyze. While many experiments were performed for free vibrating cylinders, most experiments were performed using forced oscillation.

This allows researchers to accurately define the amplitude and frequencies of cylinders while linking them with the resulting vortex patterns and loads. This structural approach to analyzing VIV has been of great help in understanding the behavior of VIV through the past decades but is not without its flaws. The core problem lies in the fact that VIV is not a perfectly periodic phenomenon. It is inherently dependent on the shed vortices which is a somewhat chaotic process. The resulting amplitudes and frequencies will therefore not converge to a single condition, but will instead stay within a small range of amplitudes and frequencies.[4]

2.2 VIV in other structures

The consequences of VIV can be found in many different structures. This section aims to discuss a few examples where VIV resulted in significant consequences.

Bridges

Long-span flexible bridges have long been known to be sensitive to vibrations induced by the wind.

The most famous example of this phenomenon is the Tacoma Bridge collapse of 1940. This bridge experienced longitudinal oscillations which suddenly switched to torsional oscillations. These oscillations were unstable and grew rapidly, with destructive consequences. There is however no consensus on a purely aeroelastic phenomenon that fully explains this behavior. Specifically, the switch to the torsional oscillation which grew exponentially can not be explained by VIV[9]. This behavior is ultimately the reason for the collapse and is most recently explained due to the non-linear internal structural behavior of the bridge. Vortex shedding and aerodynamically induced negative damping are considered to be the onset, which induced enough energy into the bridge after which the unstable structural mode took over.

More recent examples of VIV for bridges include the Volgograd Bridge [10], the Jindo Bridge [11], and most recently the Humen Bridge [12]. VIV is clearly still an ongoing issue, as new cases with problematic vibrations due to VIV still show up from time to time. The Jindo Bridge is an example where the vibration was due to twin parallel bridges interacting with the vortices from one another. This interference resulted in VIV vibrations with greatly amplified amplitudes that exceeded the serviceability limitations. Some cases of VIV did not prove to be a safety risk, but would still greatly impact the serviceability and fatigue life of bridges.

Tall buildings

Tall buildings can suffer from large amplitude vibrations due to the wind. New materials and construction techniques can result in taller, lighter, and more flexible buildings that are increasingly sensitive to VIV[13]. This requires engineers to design said buildings while carefully considering VIV. Figure 2.6 summarises most of the methods used to prevent a building from swinging too much due to the wind.

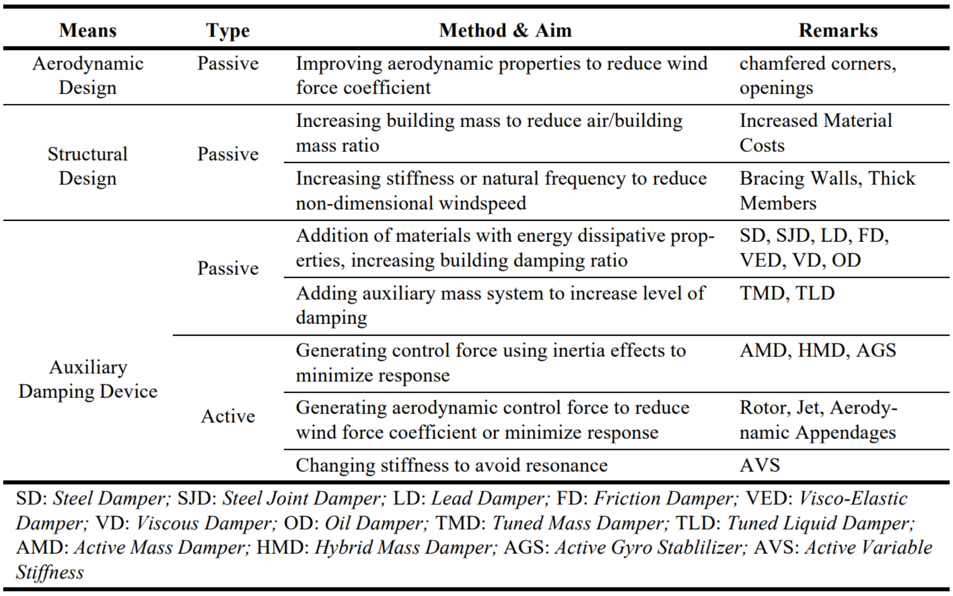

Means	Type	Method & Aim	Remarks
Aerodynamic Design	Passive	Improving aerodynamic properties to reduce wind force coefficient	chamfered corners, openings
Structural Design	Passive	Increasing building mass to reduce air/building mass ratio	Increased Material Costs
		Increasing stiffness or natural frequency to reduce non-dimensional windspeed	Bracing Walls, Thick Members
Auxiliary Damping Device	Passive	Addition of materials with energy dissipative properties, increasing building damping ratio	SD, SJD, LD, FD, VED, VD, OD
		Adding auxiliary mass system to increase level of damping	TMD, TLD
	Active	Generating control force using inertia effects to minimize response	AMD, HMD, AGS
		Generating aerodynamic control force to reduce wind force coefficient or minimize response	Rotor, Jet, Aerodynamic Appendages
		Changing stiffness to avoid resonance	AVS

SD: *Steel Damper;* SJD: *Steel Joint Damper;* LD: *Lead Damper;* FD: *Friction Damper;* VED: *Visco-Elastic Damper;* VD: *Viscous Damper;* OD: *Oil Damper;* TMD: *Tuned Mass Damper;* TLD: *Tuned Liquid Damper;* AMD: *Active Mass Damper;* HMD: *Hybrid Mass Damper;* AGS: *Active Gyro Stablilizer;* AVS: *Active Variable Stiffness*

Figure 2.6: VIV mitigation methods for high rise buildings[14]

An example of a high-rise building that required special means to reduce wind-induced oscillations is PAFC, a 600-meter-high building in the center of Shenzhen, China[15]. This building has an aspect ratio of 10.6 and is built in a region that is prone to typhoons, hence it may not come as a surprise that wind-induced oscillations could become problematic. To resolve VIV, a special damper system was installed on the 113th floor. This consisted of two damper masses with a driving device, allowing for actively controlled damping.

2.3 Stall induced vibrations

Stall induced vibrations (SIV) are unlike the VIV discussed before, not a self-initiated phenomenon. At its core, SIV relates to varying aerodynamic damping as an airfoil is exposed to different angles of attack. This aerodynamic damping may become negative, and therefore further excite any already existing oscillation[16].

An airfoil under vibration may constantly experience a slightly different angle of attack. Hence the variation of the forces exerted by said airfoil with respect to the angle of attack may either dampen or excite the vibration further. This holds true for both pitching vibrations and lateral vibrations.

For example, consider the situation of an airfoil vibrating in the perpendicular direction of the flow. When said wing moves up (in the direction of lift), the experienced angle of attack with respect to the flow will reduce. Hence, a positive C_L/α curve would result in a reduction of lift and therefore a damping effect on the wing. Under high angles of attack, airfoils tend to have a negative lift slope[17] and therefore may experience negative aerodynamic damping. Some examples of lift curves for airfoils with this behavior are shown in Figure 2.7.

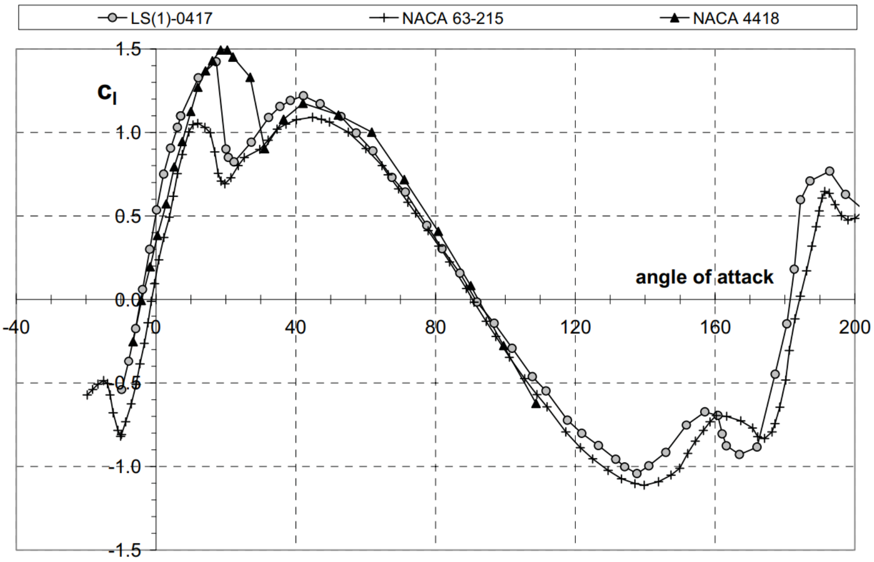

Figure 2.7: The lift coefficient of three airfoils plotted against high angles attack[18]

Both lift and drag should be taken into account when determining aerodynamic damping due to a change in the angle of attack, as vibrations are not simply defined in the direction of the lift. If after combining the drag and Lift, the force variation with respect to the angle of attack is negative, then there is negative aerodynamic damping.

When taking both drag and lift into account, more comprehensive equations can be created by linearizing the aerodynamic force equations using Tayler-series and assuming Equation 2.8 to hold true around a steady state condition where the resultant force is equal to 0. Resulting from these assumptions, Equation 2.9,2.10,2.11 and 2.12 are the four damping coefficients (c_{xx}, c_{xy}, c_{yx} and c_{yy}) which can be obtained for a wind turbine with respect to the rotor reference frame[16]. The first subfix defines the direction of damping, and the second subfix defines the direction of movement that causes said damping

$$\begin{bmatrix} F_x^R \\ F_y^R \end{bmatrix} = \begin{bmatrix} C_{xx}^R & C_{xy}^R \\ C_{yx}^R & C_{yy}^R \end{bmatrix} \begin{bmatrix} \dot{x}^R \\ \dot{y}^R \end{bmatrix} \tag{2.8}$$

$$c_{xx}^R(r,V) = \frac{1}{2}\rho c \frac{r\Omega}{W}\left[\left(\frac{2r^2\Omega^2 + V^2}{r\Omega}\right) C_D - V\frac{\partial C_D}{\partial \alpha} - VC_L + \frac{V^2}{r\Omega}\frac{\partial C_L}{\partial \alpha}\right] \tag{2.9}$$

$$c_{xy}^R(r,V) = \frac{1}{2}\rho c \frac{r\Omega}{W}\left[-VC_D - r\Omega\frac{\partial C_D}{\partial \alpha} + \left(\frac{2V^2 + r^2\Omega^2}{r\Omega}\right) C_L + V\frac{\partial C_L}{\partial \alpha}\right] \tag{2.10}$$

$$c_{yx}^R(r,V) = \frac{1}{2}\rho c \frac{r\Omega}{W}\left[-VC_D + \frac{V^2}{r\Omega}\frac{\partial C_D}{\partial \alpha} - \left(\frac{2r^2\Omega^2 + V^2}{r\Omega}\right) C_L + V\frac{\partial C_L}{\partial \alpha}\right] \tag{2.11}$$

$$c_{yy}^R(r,V) = \frac{1}{2}\rho c \frac{r\Omega}{W}\left[\left(\frac{2V^2 + r^2\Omega^2}{r\Omega}\right) C_D + V\frac{\partial C_D}{\partial \alpha} + VC_L + r\Omega\frac{\partial C_L}{\partial \alpha}\right] \tag{2.12}$$

Where the velocities and forces are defined as in Figure 2.8.

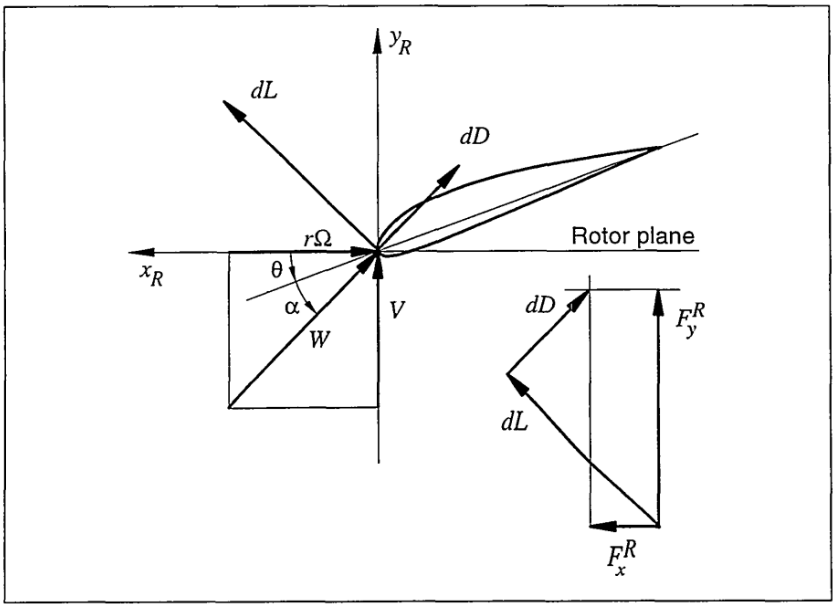

Figure 2.8: Velocities and forces of a rotating turbine as used in Equation 2.9-2.12 from [16]

Negative damping in the x-direction can thus occur at standstill conditions ($\Omega = 0$) if $\frac{\partial C_L}{\partial \alpha} + C_D < 0$, which confirms what was discussed previously. If another reference frame needs to be used, the equations can be transformed. For example, if reference frame B is not parallel to the rotor plane but rotated by an angle θ around a blade axis, just like the pitch in Figure 2.8. Equation 2.13 can be used to determine the new 'local' damping coefficients. Which can be multiplied with the accelerations in reference frame B ($\dot{x}^B; \dot{y}^B$) to get the forces in that reference frame.

$$\begin{bmatrix} C^B_{xx} & C^B_{xy} \\ C^B_{yx} & C^B_{yy} \end{bmatrix} = \begin{bmatrix} \cos\theta & -\sin\theta \\ \sin\theta & \cos\theta \end{bmatrix} \begin{bmatrix} C^R_{xx} & C^R_{xy} \\ C^R_{yx} & C^R_{yy} \end{bmatrix} \begin{bmatrix} \cos\theta & -\sin\theta \\ \sin\theta & \cos\theta \end{bmatrix}^{-1} \tag{2.13}$$

Negative aerodynamic damping does not inherently create vibration but may cancel out against the structural damping of the blade. This could allow for any already existing perturbations to vibrate freely or be exited further. If the structural damping is not completely canceled out, it would still allow for smaller forces to create bigger perturbations. This may therefore further enhance the consequences of the loads induced by VIV.

2.4 SVIV for wind turbines

There are two critical situations where a wind turbine may experience SVIV. First of all, the tower may experience VIV due to the wind. Secondly, wind turbine blades may experience SVIV when encountering inflow at a high angle of attack. Failing to take this phenomenon into account can result in critical failure of the wind turbine. Hence the certification requirements also take the conditions into account where this may occur.

Certification

Relevant conditions for SVIV would be when high angles of attack can occur for (some of) the blades. In the standard, any condition relating to a high yaw angle is thus relevant. The design load cases (DLC) from the IEC standard that are relevant will be discussed below[1].

In the design requirements, section 7 specifies the structural design requirements a wind turbine needs to consider. These requirements originate from possible situations the turbine may encounter and what would be an acceptable safety level. The appropriate calculations and tests should be performed to prove that the components are structurally sound for both ultimate and fatigue load cases.

SVIV conditions would only ever occur outside of the regular operational domain. Typically when the turbine is in parked or idle states. The IEC standard treats these conditions in section 7.4.6. Here DLC 6.2 and 6.3 describe design load cases in which SVIV could occur.

DLC 6.2 describes a situation where there is a loss of power, resulting in yaw misalignment of up to ±180° using the 50-year extreme wind speed model. This load case can be circumvented if there is a power backup present with sufficient energy to supply the control and yaw systems for at least 6 hours.

DLC 6.3 describes the condition of a 1-year extreme wind speed with a yaw misalignment of ±30° when using a steady wind model, or ±20° when using a turbulent wind model.

$$V_{e50}(z) = 1.4V_{ref}\left(z/z_{hub}\right)^{0.11} \tag{2.14}$$

$$V_{e1}(z) = 0.8V_{e50}(z) \tag{2.15}$$

Section 7.4.7 from the IEC requirements further elaborates on these requirements with DLC 7.1. It specifies the conditions that need to be tested in case of any other possible fault conditions that do not originate from a loss of power. In case of a fault in the yaw system, yaw angles of up to ±180° have to be considered. This should be combined with an extreme wind speed model for 1 year. Either turbulent or quasi-steady conditions with corrections for gusts and dynamic response should be used.

These requirements in DLC 6.2, 6.3, and 7.1 are all in relation to an ultimate load strength. DLC 6.4 discusses fatigue damage broadly for parked wind turbines. All expected hours where fatigue damage may occur outside of operating conditions should be taken into account

Generally, the conditions where SVIV can occur and any fatigue are therefore accounted for in the IEC requirements. However, this is clearly treated with a broad-brush approach. The methods used to prove compliance with the standards are not discussed, nor anything regarding failure due to SVIV. Depending on the method used to simulate these conditions, one may have varying success with correctly modeling this phenomenon[2], which could result in problematic wind turbines or costly redesigns.

Wind turbine modes

This section will give an overview of some of the modes a wind turbine may experience. Figure 2.9 shows the degrees of freedom and the appropriate terminology for wind turbines discussed in this section. The asymmetric modes are visualized in Figure 2.10 for a 600 kW turbine with its Campbell diagram.

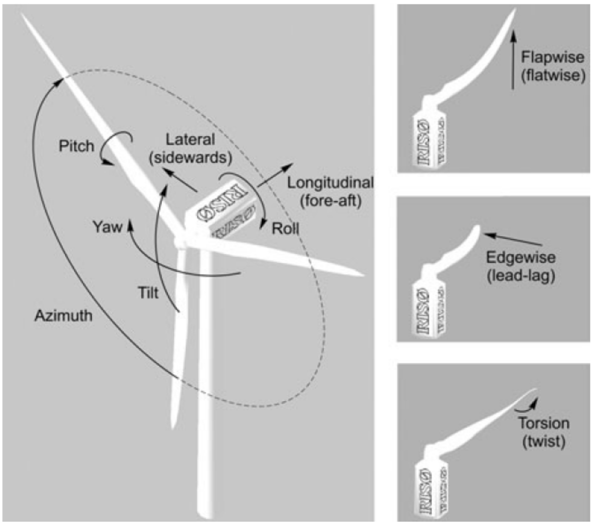

Figure 2.9: Degrees of freedom of a wind turbine[19]

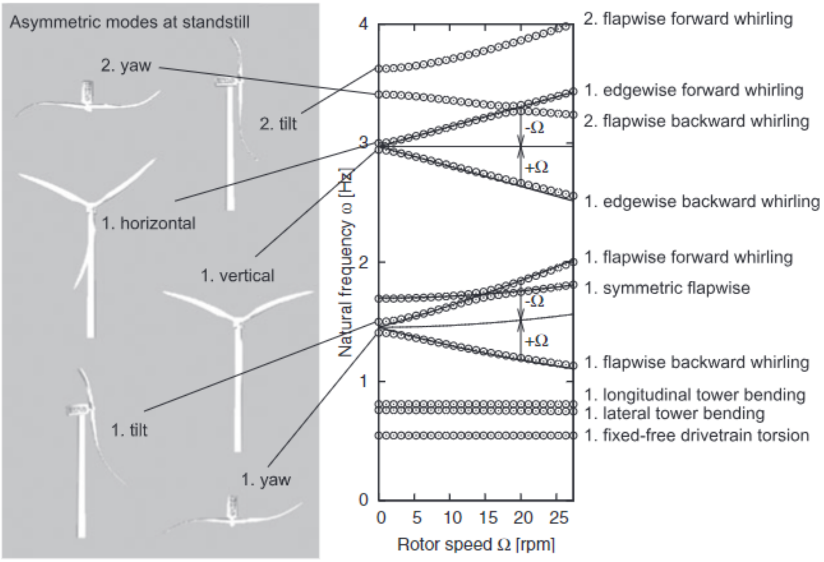

Figure 2.10: An example of the asymmetric modes at standstill with a Campbell diagram of the natural frequencies for a 600 kW three-bladed turbine[19]

First of all, there are the bending instabilities in the individual blades. These are in blade edgewise and flapwise direction. Edgewise is approximately in line with the chord of the blade, while flapwise is usually perpendicular to this. These bending modes may become a problem when dealing with SVIV as discussed previously in section 2.3.

Stall flutter is a purely torsional mode that can occur in stall when the aerodynamic center is in front of the center of twist. When there is a negative $\delta C_L/\delta\alpha$, the torsional deformation will reduce at an increased angle of attack, and vice versa.

Flap-lag flutter is an instability caused by the coupling of the flap and the edgewise motion. It is generally a rather mild instability but may become destructive after a few cycles if nothing is done[20].

Pitch-lag instability is a coupling between the pitching and edgewise modes. This may occur for wind turbines if the stiffness in the lead-lag direction is very small or a large twist is present.

Pitch-flap flutter and divergence for wind turbines are very similar to the flutter and divergence for fixed-wing aircraft, with the key difference being an increased stiffness due to centrifugal forces. Pitch-flap flutter is due to the coupling between pitching and flapping modes. Divergence is only possible when there is a very low torsional stiffness, such that the increase in torsional load at increasing angles of attack exceeds the increase in structural restoring force.

Lead-lag and tower instability is a coupling between asymmetric lead-lag modes of the blades and the tower sideways bending. The asymmetric bending mode of the blades results in movement of the center of gravity and can thus induce vibration in the tower.

Whirl flutter is a coupling in the out-of-plane modes in yaw and tilt direction. If this whirling motion is in the same direction as the rotation of the turbine it is known as forward whirl. If it is in the opposite direction then it is known as backward whirl. This mode is initiated by something that causes a change in the angle of attack, which results in a yawing motion. The sideslip induced by this can result in a tilting motion. This process can then continue in a whirling motion.

Lastly, advancing lead-lag mode coupled with tower mode instabilities can be a problematic coupling for wind turbines. Here, the edgewise mode will be enticed by gravitational forces in a 1P excitation. This excitation can then be transformed to 2P when going into the reference frame of the tower. The response of the tower can then be felt by the blades as 1P and 3P again. This transformation in frequency is therefore key to this instability[20].

Recent research on SVIV

Most recent research have been summarised in Table 2.1, and clearly, most of it was purely based on numerical simulations. The research based on simulations can be useful for insight into what parameters may be significant and what behavior is expected. The exceptions to this are for VIV in a wind tunnel experiment[21] and a study into SIV which used an on-site turbine as validation[22]. However, as seen in

Table 2.2, there is a lack of experimental data from in-field tests for VIV. This proposed study fills this gap using a full-scale on-site testing turbine for analysis of VIV and also intends to extend the research into SIV. This will be based on a more extensive field experiment for various pitch and yaw angles. In the paragraphs below, some further insight will be given on a few of the references shown in Table 2.1 with particular interest for this project

	2D	3D blade	3D turbine	experiment
Fixed wing/airfoil	[23] [24]	[25]		
Prescribed motion	[25] [17]	[26]		
Full aero-elastic	[3]	[27] [2] [28] [29] [30]	[31] [22]	[21] [22]

Table 2.1: Overview of reference research

	SIV	VIV
Model	-	[21]
full-scale	[22]	-

Table 2.2: Overview of experimental studies performed

Stettner et al.[2] analyzed SIV for the AVATAR blade of the EU FP7 project, which is a scaled-up version of the 10MW DTU reference turbine blade. This research clearly identified that different aero-elastic tools could result in drastically different results, showing the need for greater validation of simulation tools for SIV. The researchers aimed to identify the cause of said discrepancy and found the choice of the dynamic stall model to be the driving factor. The limitation identified by this research is a clear driving factor for greater validation of models for SIV. To be fully confident in the results of a model, a realistic test case is needed. This project aims to gain a better understanding of SVIV by testing a large wind turbine and comparing the results with the aero-elastic software PHATAS[32]. Various dynamic stall methods can be tested with this approach.

Khan et al.[21] analyzed results from the New MEXICO wind tunnel experiments[33] to identify the behavior of VIV on a wind turbine model. The goal of this study was to create experimental data supporting ongoing research into VIV. This data is obtained for a model under controlled conditions and should thus be an interesting point of comparison when compared to the more chaotic conditions of a field test. This study found bluff body vortex shedding and low Strouhal number shedding to be present in the experiment. For angles of attack beyond 50 degrees, no dominant shedding frequencies were found. Key differentiating points with the proposed project would be the size of the turbine model, the wind tunnel corrective effects, and the rather unsteady wind field for a large wind turbine outside. The Reynolds number and the flexibility of the blades may also vary greatly.

Chen et al.[22] used a code based on a combination of blade element theory and finite element methods to analyze stall-induced vibrations for a wind turbine. The authors concluded that with a slightly altered strategy for pitching, the resulting SIV could be reduced. This was confirmed using test data from a large wind turbine equipped with strain gauges to measure the vibrations. This paper is similar to the approach suggested for this project, with both data from a large testing turbine as well as simulations using aero-elastic code. However, the results are solely focused on SIV, and the data from the turbines are limited to 2 experiments of 400 seconds each. More extensive experiments could thus prove to be very valuable and can be expanded upon to test for VIV.

Horcas et al. [30] performed a parametric study on VIV for various pitch and inclination angles of a clamped blade from the IEA 10MW reference turbine[34]. This work followed as an extension on a previous study into the effect of tip geometry on vortex shedding[29]. This study was performed using numerical methods, coupling a multibody finite-element structural solver with a computational fluid dynamics solver. Justifying this type of parametric study was the understanding that VIV for wind turbine blades is much more complex than the two-dimensional structures in transverse motion, as it is highly dependent on the 3d geometry of the blade. This study characterizes two regions of vortex shedding. One region is at inclination angles beyond 35 degrees, where for some pitch angles, VIV was identified with a wake which was characterized by a single frequency. For inclination angles below 35 degrees the situations where VIV occurred were more scattered and the wake appeared to be more broadband. The identification of these different conditions is of interest to this project as it may help to identify the situations where vortex shedding is present. However, it should be noted that the presence of VIV is highly dependent on the 3d geometry of the turbine and this clamped blade is missing any coupling with the rest of the turbine. A direct comparison is thus unlikely to match.

In line with the gaps found in the literature, the next subsection will list the research questions of this study.

Research question

This project aims to extend the knowledge of SVIV through the analysis of experimental data from a large wind turbine and comparing these results to an equivalent situation simulated using the aeroelastic tool PHATAS. Gaining a better understanding of the key parameters affecting SVIV will help in preventing it in the future. Results from the large test turbine will provide a means of validating the aeroelastic tool for these conditions and can help validate understandings that are based on numerical simulations. The main research question to answer is thus:

Based on field-test and simulation, what are the conditions that trigger the onset of SVIV on a parked large wind turbine?

To answer this question, the limitations of the testing conditions and simulation should be determined. After which the conditions and interactions of SVIV can be analyzed. The suggested sub-questions are as follows:

- What are the key conditions resulting in the onset of SVIV?
- Which modes does the turbine experience during SVIV?
- How accurately can PHATAS simulate the field-test results?

Chapter 3

Methodology

This section aims to provide an overview of the methodology used to go from the information obtained from the turbine to the analyzed data and conclusions. First, the test setup will be discussed to explain which data sources will be available. Then in section 3.2, the processing and visualizing method of the data is discussed. Lastly, section 3.3 discusses the models used to mimic the experiments with a simulation are discussed.

3.1 Test setup

The set-up of the experiment involves the TIADE large testing turbine. Two out of three blades are equipped with strain gauges near the root, both on the edgewise axis and the flapwise axis. These strain gauges are on both the compression and tension side, allowing for the calculation of the bending moments as shown in the cross-section in Figure 3.1. The blades equipped with these strain gauges are blades number 2 and 3. The bending moments are defined in either edgewise or flapwise direction. The flapwise direction is defined to be perpendicular to the local chord, while the Edgewise direction is defined to be along the local chord. Since these directions are with respect to the local cross-section of the blade, they rotate with the blade as it is pitching.

The wind turbine will be controlled by defining the pitch of the blades with respect to the rotor plane and defining the yaw angle with respect to the north. When the yaw angle is compared to the wind direction, the yaw misalignment can be controlled. The azimuthal angle of the turbine is controlled by fixing it to the desired angle using the brakes of the turbine. The azimuth angle is defined as 0° when blade 1 points straight up into the sky, with positive angles defined clockwise as shown in Figure 3.1. Hence, at an azimuth angle of 120 degrees, blade 2 will be pointing upwards. Over several test runs the Yaw angle, azimuth angle, and pitch angles of the different blades will be varied.

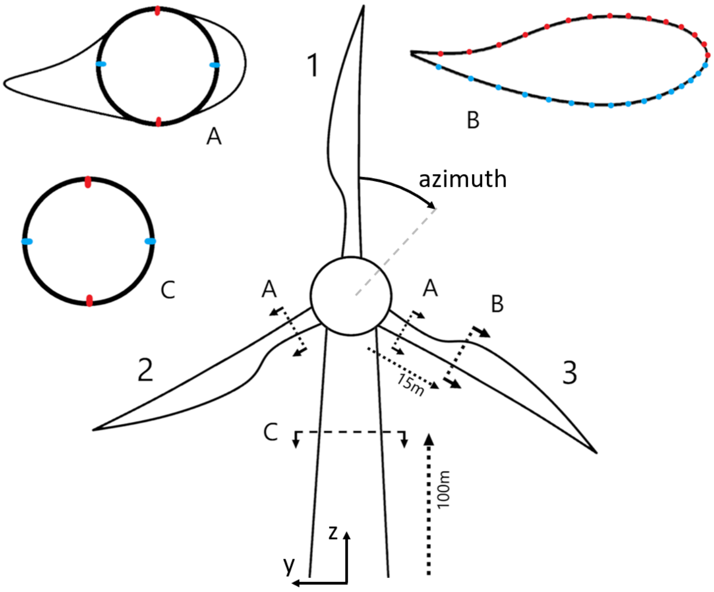

Figure 3.1: Front view of the turbine set up, with the azimuth angle defined clockwise from the position straight up. Cross-section A: strain gauges in blade root; Cross-section B: pressure sensors in blade 3; Cross-section C: strain gauges in the tower.

To obtain the environmental data, there are three sources of information. First of all, a wind measuring station is set up on the nacelle which can obtain the wind speed and direction. Secondly, there is a met mast set up approximately 1.5 km away which can provide further information on the atmospheric stability. Lastly, there is a profiling lidar set up 280 meters upwind of the wind turbine. This lidar was used to determine the inflow wind conditions on various altitudes between 42 and 188 meters. These various options are sketched in Figure 3.2 and further info on the lidar is presented in Table 3.1.

Distance to turbine	280 m
Direction from tower w.r.t. North	210°
Measurement heights	42 m
	58 m
	71 m
	82 m
	97 m
	110 m
	121 m
	136 m
	162 m
	175 m
	188 m

Table 3.1: Lidar location w.r.t. the wind turbine and measurement heights

It is noted that the wind measurements on the nacelle result in unusually high wind speeds as the wind accelerates around the nacelle. The met mast is located relatively far away, which can give a decent indication of the current atmospheric conditions, but will not result in accurate inflow measurements. Hence during this project, the profiling lidar upwind of the wind turbine is used as the main source of inflow data. The other options are used as redundancy in obtaining this crucial information as well as confirming if the lidar data is realistic or faulty. These instruments also provide information for various other research outside of the scope of this project.

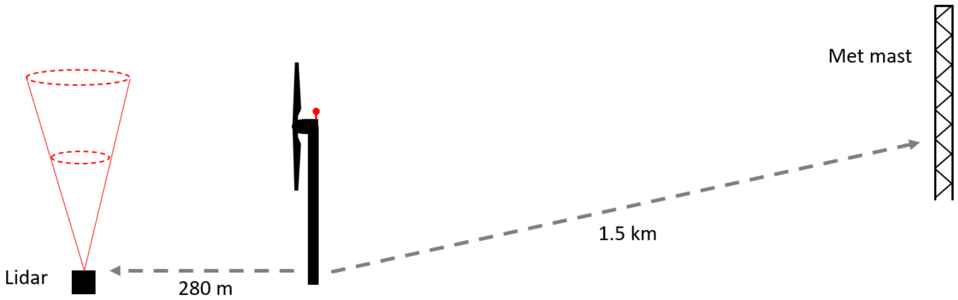

Figure 3.2: Wind measurement set-up (not to scale), lidar 280 m upwind, met mast 1.5 km away

3.2 Analysis

For analyzing the data, it is firstly important to find out how reliable the data sources are. After understanding the reliability of the data, the results can be visualized in the frequency domain. Visualizing the data is an important step to help better understand the measured results.

Data sources

Due to the inherent stochastic nature of the wind, the experiment will result in data for continuously varying conditions. When analyzing the data, it may therefore be needed to filter out severe gusts and very small steps in yaw angle will be challenging to test for. Also if the test takes long, the inflow conditions are bound to change throughout the test, making the results more challenging to interpret. The turbulence intensity and variance in the inflow conditions should thus always be taken into account when analyzing the results. Accurate measurements of the wind will likely be crucial to better interpret the results.

There are three different sources to obtain data on the wind direction and speed: A met mast, a lidar, and a measurement station on the turbine nacelle. While there was also a lidar installed on top of the nacelle, it was not usable for this project. The met mast will give accurate results at 2Hz every 20 meters from 50 to 230 meters high. However, the mast is located about 1.5 km away. The inflow conditions can therefore only be considered to be similar. This helps identify how trustworthy the other two wind measurements are. However, because of the distance, the inflow data from this source was not the first choice for analyzing the results.

The wind measurement station on the turbine nacelle measures the local wind but is strongly influenced by the presence of the blades and the nacelle itself. The wind speeds measured by this system were consistently higher than the lidar or met mast data. This is likely caused by the wind accelerating around the nacelle, and the difference in windspeed will likely vary depending on the yaw misalignment of the turbine. There is also the possibility of the measurement station being in the wake of a rotor blade during some experiments. Because of these reasons, the nacelle wind speed was not used in analyzing the experimental data.

The lidar used in this project is a profiling lidar set up about 280 meters south-south-west of the turbine (210 degrees). To calculate the speed and direction, it assumes some homogeneity at the same altitude to get its velocity vectors. The lidar is located in the free stream, up-wind of the turbine, and measures at a frequency of 4 Hz. The difference between the wind direction and the lidar direction varied between -60 and 80 degrees and is elaborated on in section 4.1. Despite the assumptions used for determining the wind speed with the lidar, it is considered to be a trustworthy source for finding the inflow conditions of the turbine. The proximity to the turbine makes the lidar preferable over the met mast. Therefore, the lidar is preferred as the source for the inflow data when analyzing the experiments. The measurements on the met mast will be used if the lidar data is unavailable or inaccurate due to rain or fog.

The force data received from the strain gauges are measured at a frequency of 64 Hz, which should give enough resolution to determine the frequencies of the force oscillations. This force signal can be converted into the bending moment. The bending moment is interesting for this case as it is directly related to the vibrations experienced by the blade. The data on the loads of the wind turbine are measured in several different locations. Blades 2 and 3 contain strain gauges at the root of the blade.

Blade 3 also has pressure sensors installed around its perimeter, 15 meters away from the root. Data from these sensors is sensitive to rain and has experienced some issues where sometimes no data is logged. Because of this, the data need careful post-processing to filter out any time where the signals are absent (NaN), set to 0, or unnaturally high peaks. The data was afterward visually inspected to see if there is any abnormal behavior. The pressure data was measured with a sampling frequency of 256 Hz.

The tower contained strain gauges near the root (8m) and at 100 meters high, and an accelerometer at the top of the tower (110m). These signals are all measured at a sampling frequency of 64 Hz. After comparing the frequency spectrum between these different sources, the tower bending moment at 100 meters was chosen to be used for most comparisons. This signal showed the same frequencies visible in either the accelerometer or the force sensor near the tower root. Where deemed to be of additional value, the tower 8m bending moment or tower top accelerometer data may still be considered. The strain gauge at 8 meters shows higher peaks for the tower modes while damping out other modes more, while the accelerometer near the top of the tower showed the modes originating from the blade modes more (and less of the tower modes).

Visualisation

After finding a suitable time series to analyze, the bending moments of this series will be transformed into the frequency domain. The dominant frequencies should be clearly visible in the power spectrum. The amplitude and frequency in this spectrum are key parameters to compare with the flow and turbine conditions. If SVIV occurs at any specific conditions, this should be visible in this data.

The Matlab routine ”pwelch” is used during this project to create any PSD. This is a built-in function of Matlab, which estimates the PSD of an input signal using Welch’s overlapped segment averaging estimator. The default behavior is generally used, which splits the data into 8 segments with a 50% overlap. For most experiments, the conditions were changed every 5 or 6 minutes, resulting in segment sizes of 66 to 80 seconds.

In order to visualize the frequency domain results for several pitch angles, yaw angles, inclination angles, etc. a surface plot is used. The plot visualizes the power in dB in color using Equation 3.1 where y is the power of the signal. dB was chosen in order to also visualize the force oscillations of lower magnitude without drowning it out due to other much larger amplitudes at different frequencies. This does have the undesirable side effect that small changes in color might signify a reasonably large difference in amplitude. Because of this, when it is deemed to be needed, the absolute power is also sometimes plotted.

$$y[dB] = 10log_{10}(y) \tag{3.1}$$

Lastly, due to issues regarding confidentiality, the actual frequencies can not be shared. Instead, the frequency spectrum is normalized such that the 1st fore-aft tower mode of the experimental data is at exactly 1. This is achieved by dividing all frequencies throughout the report by the frequency which was identified to be the first tower mode.

Flow chart

An overview of the approach for this report is visualized in the form of a flow chart in Figure 3.3.

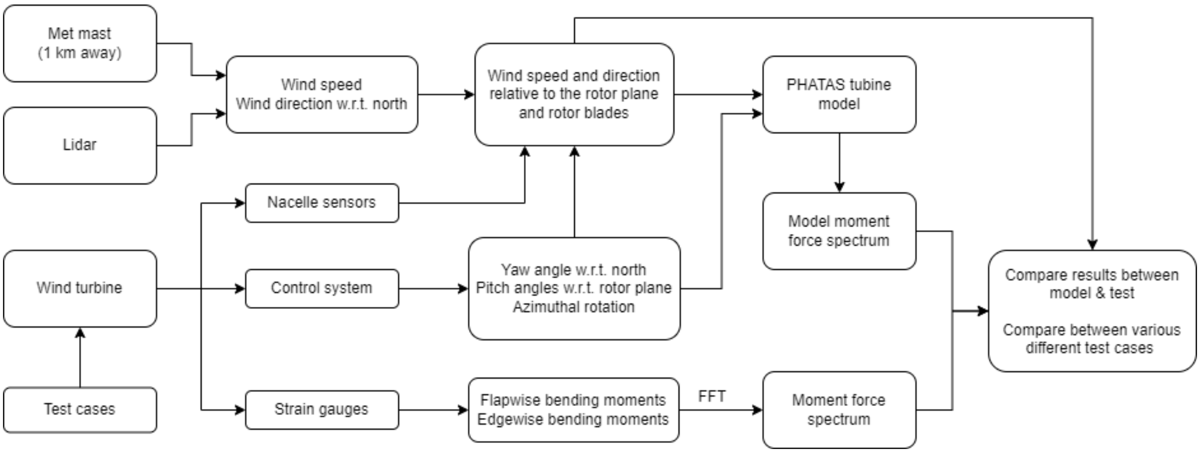

Figure 3.3: Flow chart of project

3.3 Aero-elastic modeling

For the modeling of SVIV, the wind turbine design package FOCUS6[35] developed WMC (now LM Wind Power) is used. In this software, a full model of the test turbine is modeled. For solving the dynamic response and loads, the aeroelastic solver Phatas[32] is used. The aerodynamic solver is expanded upon with the aero module of ECN (now part of TNO) which is a package containing two aerodynamic codes: Free Vortex Wake (FVW) model and Blade Element Momentum (BEM) model [36]. The inflow conditions can be manually set to a steady inflow, be interpolated from wind measurements, or be generated stochastically using SWIFT[37].

Phatas is a program for horizontal axis wind turbine analysis and simulation. This program was developed to model the dynamic response and loads of horizontal axis wind turbines. The structural response is modeled using a finite element approach for the wind turbine. This structural behavior is coupled to aerodynamic forces calculated using a model based on Blade Element Momentum (BEM) theory.

Blade element momentum theory

BEM theory is commonly used for fast engineering models of wind turbines. It relates the change of momentum of the incoming wind to the local forces of the turbine blade. This method assumes the actuator disk to be a 2-D plane exerting a force upon the tube of air flowing through. The flow that passes through the rotor disk is discretized in the radial and azimuthal directions. The tube obtained by discretizing in the radial direction is called an annulus.

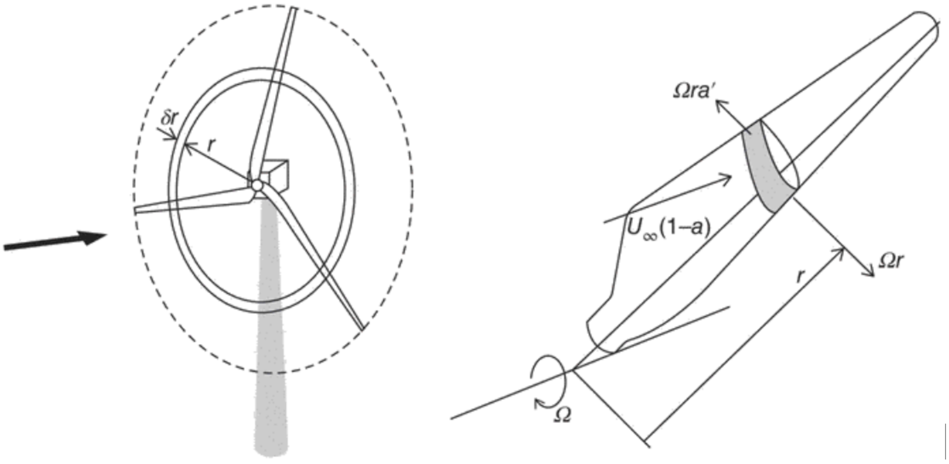

Figure 3.4: Blade Element Momentum theory annulus at radius r and the corresponding blade element [38]

In BEM theory, the radial wind component is ignored and all wind stays within their respective stream tube. Different stream tubes are therefore solved independently of each other. The wind turbine exerts a force on the flow, and in doing so, induces a velocity in the air. For wind turbines, this velocity is against the flow directions and thus slows down the air. The model is resolved by iteratively solving for the axial induced velocity factor, a, in each annulus using the equations of conservation for mass and momentum.

$$a = 1 - \frac{U_r}{U_\infty} \tag{3.2}$$

$$\rho A U = \dot{m} = constant \tag{3.3}$$

$$F = \Delta p_r A_r = (U_\infty - U_r)\,\dot{m} = \rho A_r (1-a) a U_\infty^2 \tag{3.4}$$

The rotor forces can be solved by calculating the local wind speed and direction at the blade element and identifying the force coefficients from the airfoil polar. This is achieved by splitting the blade up into slices as shown in Figure 3.4 and assuming conditions to remain constant for this slice. The local inflow velocity (W) and the angle of attack (α) can be determined as in Figure 3.5 after which the lift and drag can be calculated. Here C_L and C_D are the coefficients for lift and drag, which should be obtained from an airfoil polar and depend on the angle of attack. The contributions of the various blade elements can be added up to obtain the total force and calculate the next iteration of induced velocity.

$$Lift = C_L \frac{1}{2} \rho W^2 S \tag{3.5}$$

$$Drag = C_D \frac{1}{2} \rho W^2 S \tag{3.6}$$

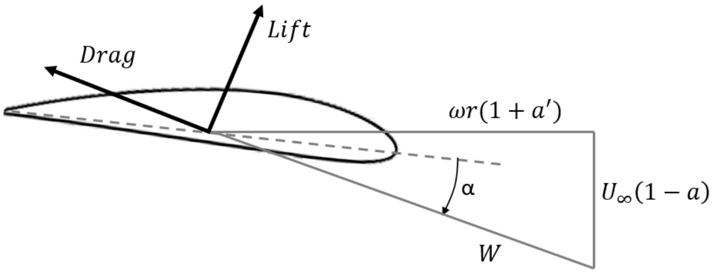

Figure 3.5: Blade Element Momentum theory inflow conditions at a blade cross-section

The main advantages of BEM lie in its simplicity and speed. However, due to its simplicity, it can not take everything into account. For example, in order to take into account that the blade is finite, the effect of tip and root vortices needs to be corrected for. Also, situations of yawed flow will require additional corrections.

Lastly, since the forces are calculated based on airfoil polars, unsteady conditions need to be accounted for through other means. Various dynamic stall models have been developed to resolve unsteady flow around airfoils. However, these models are usually not validated for conditions in deep stall. This may prove to be problematic when simulating the conditions where SVIV is present. Linking Phatas with the aero module allows for simulations using other dynamic stall models than what has already been implemented in Phatas.

In the simulations for this report, the Prandtl tip and root corrections[39] are used to account for the tip and root vortex. The correction for yaw was modeled using the in-house model of ECN (now part of TNO) by Schepers[40]. The dynamic inflow model used is also an in-house model originally developed by Snel and Schepers[41]. The various dynamic stall methods used during the simulation are discussed in section 3.3.

Dynamic stall models

For simulating the turbine in conditions similar to the experimental data, the use of a dynamic stall model is likely to be crucial. There are unsteady inflow conditions and high angles of attack, resulting in unsteady dynamics in the deep stall conditions and possible vortex shedding. The Dynamic stall models used in the simulations are the 1st order model from Snel[42] created based on Truong[43], a 2nd order model based on the Snel 1st order model[44], and the model developed by Leishman and Beddoes[45] which was expanded to wind turbines[46]. The chosen dynamic stall models were limited to what was already implemented in PHATAS or the aero module from TNO, and among those, the ones that did not crash the simulation. The Bedoes-Leishman model can use several different flow separation models[47], but during this project, only the separation method from Larsen[48] remained stable and was thus used.

It is acknowledged that the dynamic stall models used have not been developed based on deep stall behavior and may therefore result in less accurate simulations. It is however still interesting to see how they perform during the simulations. It was beyond the scope of this project to implement a new dynamic stall model in the simulation software or to fine-tune the input parameters of the models used. This limited amount of 'fine-tuning' the models may explain why some of the models did not successfully run in the simulations, despite being implemented. The combinations of the unique conditions of a parked turbine at large angles of attack may also impact the stability of the aero-elastic solver using the dynamic stall models.

Free vortex wake model

The free vortex wake model implemented in the aero module can be used as an alternative for BEM. This method is generally considered to be a higher fidelity engineering model than BEM (if applied correctly), but it also takes much longer to simulate. It is based on a generalized lifting line theory utilizing a free vortex wake. In this model, the lift distribution of the blade is modeled as a vorticity distribution along the quarter chord line of the blade. This follows according to the Kutta-Joukowski theorem shown in Equation 3.7 where $\Gamma(y)$ is the local circulation.

$$L = \int \rho V \Gamma \left(y\right) \tag{3.7}$$

According to Helmhotz's theorems, vorticity can not be created or destroyed while in a fluid. Hence, the Vortex lines along the chord need to remain constant and should either continue into infinity or form a closed loop. This is achieved by modeling shed vortices connected by trailing vortices to form a closed loop. Each vortex ring retains constant vorticity, but varying circulation along the blade or in time can be modeled by shedding new, overlapping, vortices. Figure 3.6 shows a visual representation of how the vortices are modeled. The shed vorticity convects with the wind. Its path and speed can either be modeled as a fixed path or be calculated based on the influence of all other present vorticity. A vortex-shedding model that actively calculates the path for each timestep is known as a free vertex model.

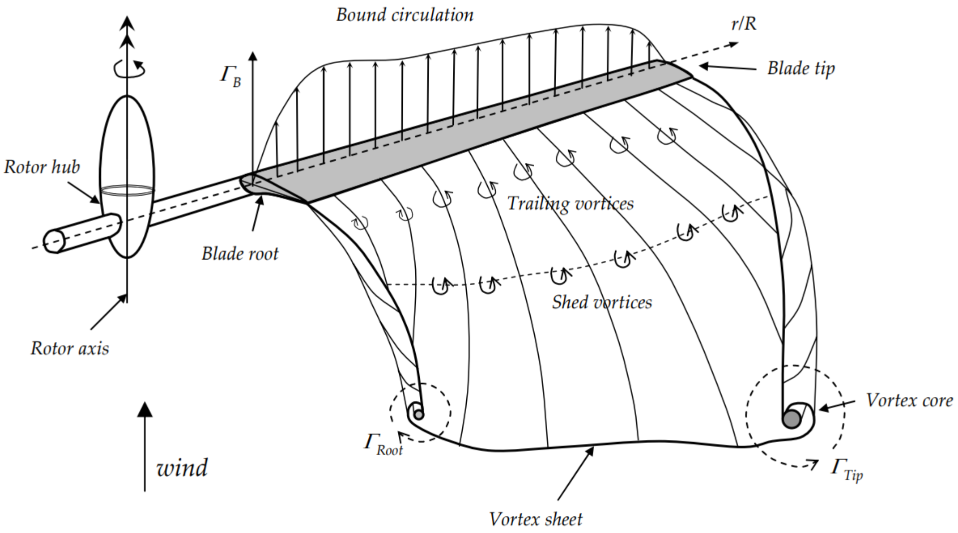

Figure 3.6: An illustration of a free Vortex wake method [49]

The method of obtaining the actual vorticity distribution may vary in this method. In the aero module, this circulation is obtained from the airfoil polars of the blade. Because of that, it still relies on dynamic stall models to estimate the dynamic behavior as inflow conditions vary. The velocity in the wake can be calculated by adding the contribution from all the vorticity in the wake (V_{ind}) to the free wind velocity (V_{inf}), where V_{ind} can be calculated according to the Biot-Savart equation presented in Equation 3.8.

$$V_{ind} = -\frac{1}{4\pi} \int \Gamma \frac{\vec{r} \times d\vec{l}}{r^3} \tag{3.8}$$

Free vortex wake models are capable (if applied correctly) of simulating more realistic conditions than a BEM model, but they do have some flaws. The induced velocity by a vortex line is inversely proportional to the distance with regard to that vortex line. Due to this definition, the induced velocity approaches infinity as one gets closer to the vortex line. To solve this singularity a viscous vortex core needs to be modeled for which various models exist. Another issue with the vortex lines is the assumption that they remain constant in strength, viscous effects like dissipation would prevent this assumption from holding. Lastly, discretizing the entire wake and calculating its influence requires much more computational power than a similar BEM calculation.

For this project, the downside of needing a large computational effort may be partially reduced because the turbine is not rotating. A shorter wake with a higher timestep may result in results of reasonable quality. A lack of viscous effects and the need to rely on a dynamic stall model will likely strongly influence any results, similar to BEM. This report will apply the same dynamic stall models as used in BEM and aim to reduce the computational time to a reasonable time to see if the results are an improvement over BEM.

Turbulent inflow modelling

To set up the load case, a realistic inflow of air is simulated using SWIFT[37]. These conditions should be the same as for the experiment, hence the input will be directly based on the measured data from the experiment. Both steady and unsteady wind fields can be generated, allowing for possibly faster testing before making everything as realistic and computationally heavy as needed.

SWIFT works by starting with an auto power spectral density (APSD) and the coherence function. It then uses the fast Fourier transform, to generate their inverse discrete Fourier transforms. It is hereby generating discrete-time sequences of the wind as if sampled from continuous random signals. The phase of the wind is generally assumed to be a uniform distribution between 0 and 2π.

As an alternative to SWIFT, it is also possible to use the wind as measured by the lidar during the experiment. This would result in a very accurate indication of how the wind behaved during the experiment. However, this method is limited by a lack of any horizontal shear as the lidar only measures the wind speed and direction on different heights, but not on different lateral locations of the turbine. A few steps were taken to implement this wind speed in the simulation. Firstly wind would be separated into a u and v component, based on the misalignment with the mean wind direction. The vertical component v is neglected. The defined velocities from various altitudes are then interpolated using a splines method, and saved in the Turbsim format. This format can be read by the 'Aero module' from TNO. The yaw angle of the turbine would be set based on the mean yaw-misalignment of the experiment. The mean yaw misalignment could likely have been implemented in the components of the wind file but was defined separately to have a good overview when using the same wind files in different test cases with various yaw angles.

Structural degrees of freedom

The structural behavior of the turbine is modeled using PHATAS[32], which resolves the structural deformations and loads through a beam-based model. The individual components can be modeled as elastic or rigid. Table 3.2 gives an overview of which components of the turbine were modeled elastically.

For a fully aero-elastic simulation, all components of the turbine should be simulated elastically. Unfortunately, this project encountered problems when trying to simulate the turbine with the rotor shaft torsion. Setting this component to be resolved elastically by the structural solver resulted in all simulations crashing before getting any results. The cause of the crash is an instability that results in unrealistically large forces, accelerations, and deformations before ending with 'NaN'. the cause of this instability is currently not fully understood and therefore unresolved. Hence, the shaft was modeled as a rigid component. This should result in the absence of a shaft natural frequency in the simulations. There is also a chance that this may impact the coupling between the blades.

The tower bending modes are defined in the normal direction of the rotor plane and the lateral direction. Oscillations in these directions are also referred to as fore-aft (FA) and Side-Side (SS).

Structural component	**Modeled Elastically**
Blade edge-wise	ON
Blade flap-wise	ON
Blade torsion	ON
Tower bending	ON
Tower torsion	ON
Shaft torsion	OFF

Table 3.2: Natural frequencies identified from the experiment with all blades is in vane position of 85 degrees pitch

Simulation analysis

The analysis of the simulation data is performed in a similar way as the experimental data is analyzed. The bending and accelerometer data output from the simulation is therefore defined to be in the same locations as was the case during the experiments. That is 100 meters up the tower, in the nacelle, and at the root of the blades. Further data can be obtained from the simulation, but these direct comparisons are essential when determining the performance of the simulation versus the experiment.

Most data from the simulation will also be converted to the frequency domain. Just like for the experiment, this will be done by calculating a PSD estimate using the ”pwelch” function in Matlab. This function uses Welch’s overlapped segment averaging estimator with by default 8 segments with a 50% overlap. A few simulations were too short or failed after a short period. If these simulations were still deemed of interest, instead of the default 8 segments, a segment size was set at 80 seconds with 50% overlap. This length was based on how long the 8 segments would be for a simulation of 360 seconds.

Chapter 4

Experiment results

The results from the in-field test turbine need to be processed and analyzed. This section aims to present the natural frequencies visible in the data, identify the increase in magnitude in the bending moment oscillations due to SIV, and check if there is any vortex shedding using pressure sensors.

4.1 Experiment conditions

Experiments have been performed spread out over 4 different days for various different tests. Due to this spread-out nature of the tests, naturally, the environmental conditions also varied greatly. Table 4.1 shows an overview Of the conditions which were tested.

	Pitch angle			**Yaw misalignment**	**Rotor azimuth**	**Wind (std) [m/s]**	**Ti [%]**	**Wind dir.**
#	Blade 1	Blade 2	Blade 3					Lidar : 210°
1	85°	-15° till 85°	85°	0°	120°	15.9 (2.0)	13%	290°
2	85°	85°	-15° till 165°	0°	240°	14.3 (1.6)	11%	150°
3	85°	85° till 180°	85°	90°	120°	18.8 (2.6)	14%	265°
4	85°	85°	85°	0° till 60°	120°	15.9 (2.0)	13%	290°
5	85°	85°	85°	-130° till 95°	240°	14.3 (1.6)	11%	150°
6	85°	85°	85°	-5° till 200°	240°	19.1 (2.6)	14%	242°
7	85°	85°	85°	-110° till 90°	330°	17.4 (3.4)	19%	270°
8	85°	180°	85°	94° till 113°	120°	19.5 (2.8)	14%	270°
9	85°	85°	180°	117° till 94°	240°	16.6 (1.8)	11%	268°
10	89°	89°	89°	90°	240° till 360°	19.2 (2.6)	14%	256°

Table 4.1: Table summarizing the test conditions for the various experiments

As can be seen from Table 4.1, various tests were performed while varying either the yaw angle or the pitch angle. The test closest to a repetition is test 2 which has similar conditions to test 1 but with a different blade pointed up. Alternatively, there are also tests 5 and 6 which repeat the same test but with a large difference in wind speed.

Experiments 8 and 9 are unique because during these experiments severe vibrations were visibly present in the wind turbine. The effect of SVIV is less noticeable in the other experiments, but there are still a few conditions identified where oscillations in the measured forces tend to increase in magnitude.

4.2 Repeated pitch traverse

The experiments did not contain any repeated tests under the exact same conditions to be used as validation. The closest thing to a repeated test were experiments 1 and 2 from Table 4.1. These two tests perform a pitch traverse of the blade at 0 degrees azimuth, however, one test has blade 2 at 0 degrees azimuth, and the other test has blade 3 at 0 degrees azimuth

Test 1 performs the pitch traverse for blade 2. In this test, blade 2 is pointing up (120° azimuth) and the wind speed is about $15.9 m/s$ with a turbulence intensity of about 13%. Test 2 performs a similar pitch traverse for blade 3. Here, blade 3 is pointed upwards (240° azimuth) and the wind speed is about 14.3m/s. with a turbulence intensity of about 11%.

Other than the slightly varying inflow conditions, there is one key differentiating factor between these two experiments. During the test for blade 2, the trailing edge of blade 3 was not clean as it was used for different ongoing experiments. Similarly, blade 2 wasn't in a clean state during the experiment for the pitch traverse of blade 3. Since these non-clean blades were kept in a vane position of 85 and the yaw angle of the turbine was kept at 0, these slight alterations to the blades should not significantly impact the experiments. However, it is important to realize that the coupled effects between the blades may have been affected.

Figure 4.1 and Figure 4.2 show a comparison of the edge-wise bending moment and the tower normal moment between the two experiments. The left plot represents experiment 1 where blade 2 is pointed up, while the right plots show the results from experiment 2 with blade 3 pointing up. It is good to note that blade 3 went from -15 to 85 degrees in steps of 5 degrees, while the experiment with blade 2 was in steps of 15 degrees. Hence it is expected that the results for blade 3 capture some more details, but follow a similar behavior and magnitude as with the experiment for blade 2.

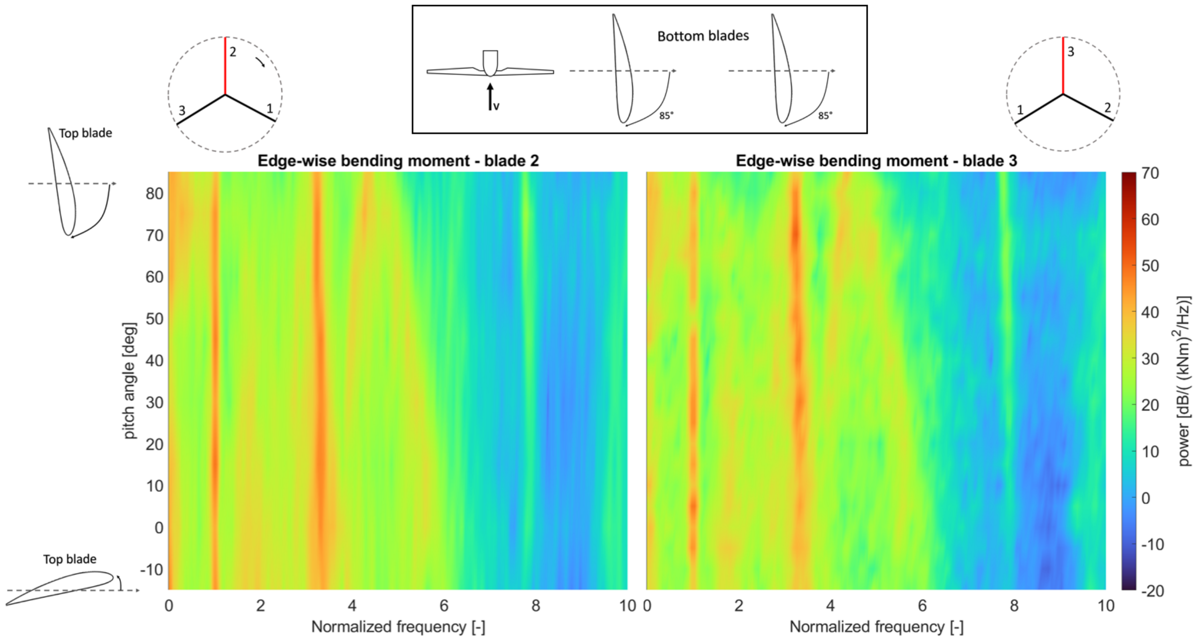

Figure 4.1: Edge-wise bending moment for repeated pitch traverse for the top blade, blade 2 (15.9m/s) vs. blade 3 (14.3m/s) pointed up

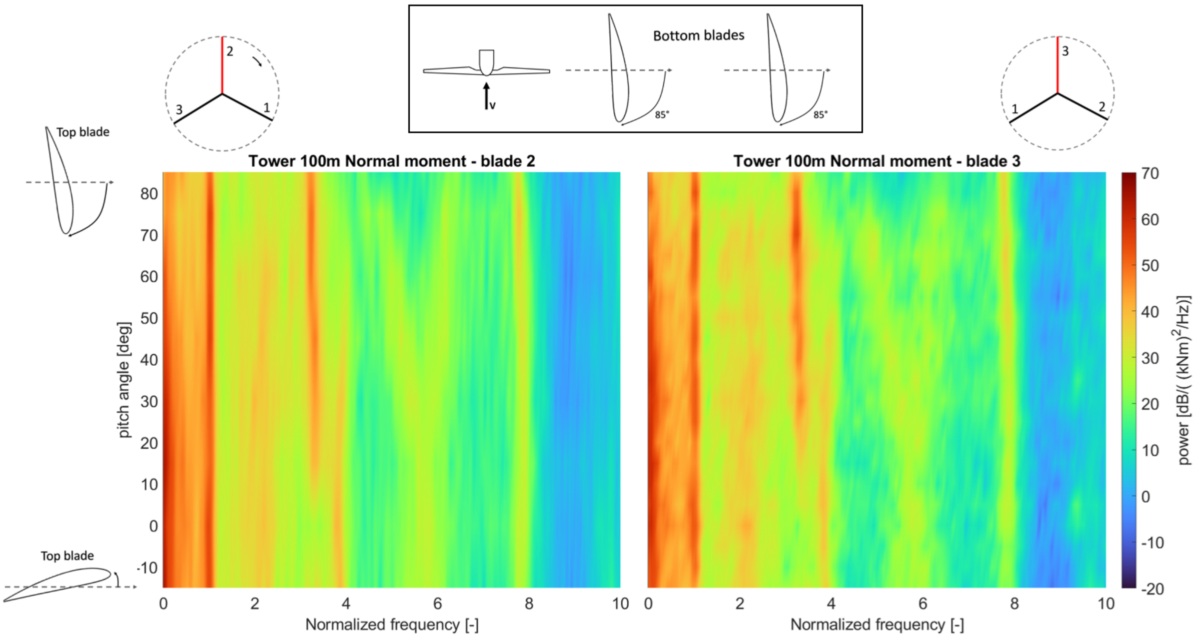

Figure 4.2: Tower normal moment (at 100m) for repeated pitch traverse for the top blade, blade 2 (15.9m/s) vs. blade 3 (14.3m/s) pointed up

From the figures above, it is deduced that the magnitudes and frequencies of the modes behave in a very similar way. The peaks in oscillations can be found at the same frequencies and with very similar magnitudes. This strengthens the belief that the data obtained during these experiments is trustworthy.

4.3 Key frequencies

The first step in analyzing the data from the wind turbines is to identify what the dominant frequencies are in the wind turbine. These frequencies were identified purely by inspection of the spectral distributions of the various force measurements. Most frequencies were validated using an internal TNO report[50] on simulating the turbine in question. Some simple calculations and comparisons to the literature were also performed. An overview of the dominant frequencies is presented in Table 4.2. The frequencies have been normalized with respect to the 1st tower mode.

Vibration mode	Normalised frequency [-]
1st tower FA	1
1st tower SS	1
1st drivetrain torsion	1.8
1st flapwise	2.2
asymmetric edgewise in yaw	2.9
asymmetric edgewise in tilt	3.3
symmetric edgewise	4.4
2nd flapwise	6.2
2nd tower FA	7.8
2nd tower SS	7.8

Table 4.2: Natural frequencies identified from the experiment with all blades is in vane position of 85 degrees pitch

All of the natural frequencies mentioned in Table 4.2 were obtained by identifying the peaks in the PSD plots created from the measured data of the turbine. Figure 4.3, Figure 4.4 and Figure 4.5 are three examples of said power density plots. Note that the z-values denote the amplitude in dB and are thus log scale. This helps in identifying higher natural frequencies which may be more damped, conversely, a small change in shade is equivalent to a rather significant difference in amplitude.

The general process of identifying which relied on identifying which peaks in the power spectral density plots were present for which sensor. Based on when and where a force oscillation was present, a reasonable estimate could be made. For example, the frequency of the tower modes is present in all data and stays (close to) constant regardless of pitch or yaw. They also are the only oscillation peaks consistently present in the tower bending moment near the top and bottom for all conditions, both in lateral and normal directions.

The flapwise bending moment at the root of blade 3, as the yaw angle is varied, is visualized in Figure 4.3. As can be seen in the box to the right of the plot, all three blades are pitched at 85 degrees and blade 3 is pointing straight up at an azimuth angle of 0 degrees. The power of the oscillations in the flapwise bending moment clearly has a high amplitude at frequencies near 0 due to variations in the wind, at 1 due to the 1st tower frequency, and at 1.8 and 2.2 due to the generator shaft torsional natural frequency and the 1st flapwise natural frequency. At 4.4 a very small peak is present due to coupling with the edgewise natural frequency. At higher frequencies, peaks in the oscillation power are visible at 6.2 for the 2nd flapwise natural frequency and 7.8 for the second tower natural frequency, but the magnitude of these peaks is already much smaller.

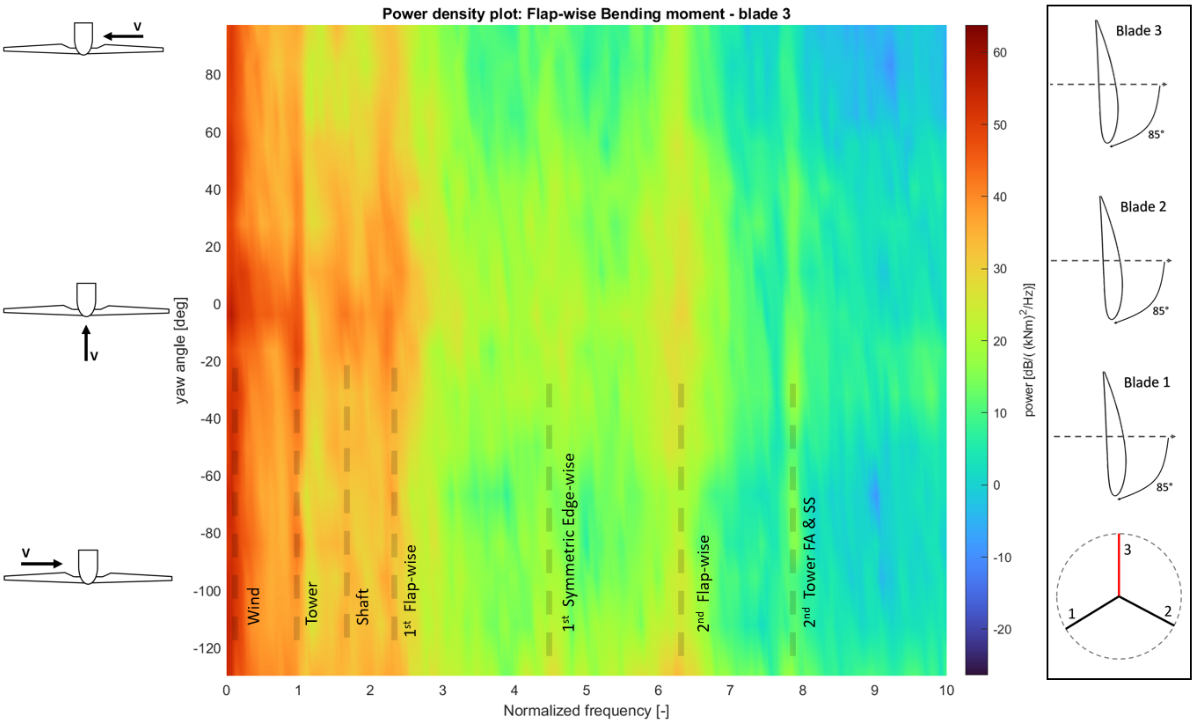

Figure 4.3: Power spectral density of the flapwise bending moment during yaw traverse, blade 3 is at 0 degrees azimuth

The edgewise bending moment for blade 3 is presented in Figure 4.4. Other than the tower frequency of 1, there are two other frequencies present of a similar magnitude. These are at the normalized frequencies of 3.3 and 4.4 and are natural frequencies (asymmetric and symmetric) of the blade in the edgewise direction. Oscillations are also present at the normalized frequency of 7.8 with a lower amplitude due to the 2nd tower frequency. An even lower peak is present at 6.2 due to the interaction with the flapwise natural frequency.

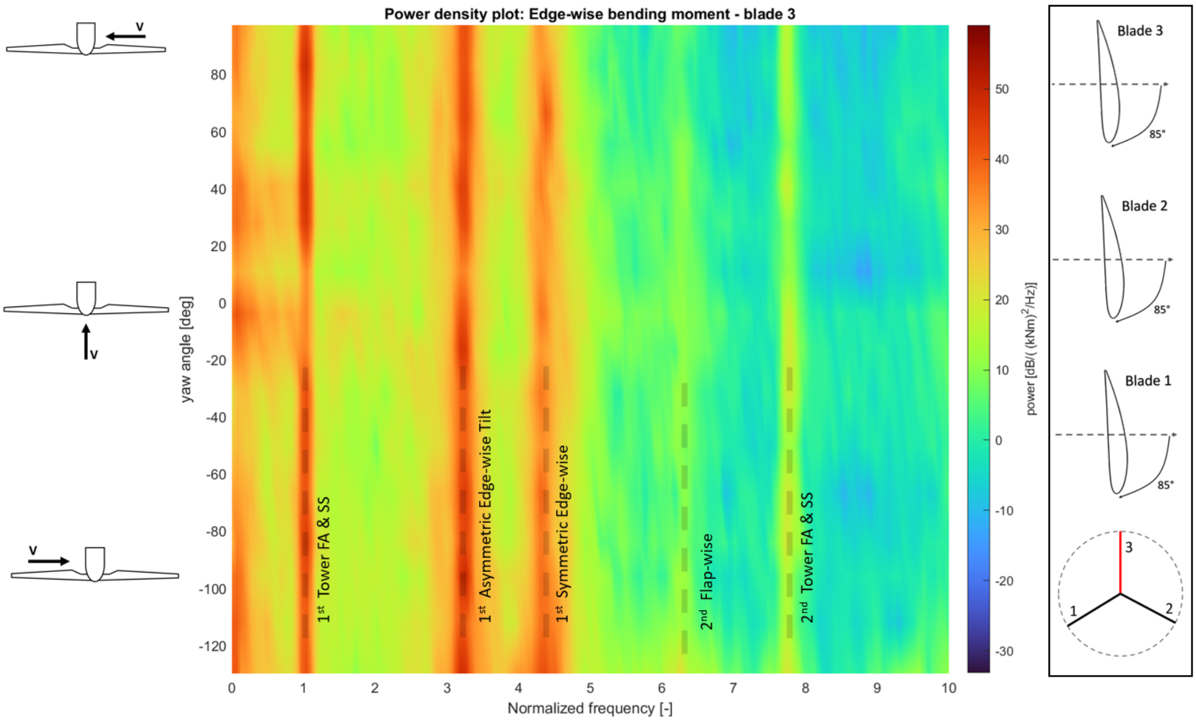

Figure 4.4: Power spectral density of the edgewise bending moment during yaw traverse, blade 3 straight up

In Figure 4.5, the same experiment is performed with blade 3 in a horizontal position. Here, the peak for the force oscillations with a frequency of 4.4 is still present, but the peak at 3.3 is not. Instead, there is a peak for force oscillations present at the normalized frequency of 2.9. If an azimuth angle other than 0 or 90 degrees is tested, both peaks at 2.9 and 3.3 are visible. Hence it is concluded that the oscillation at 2.9 is an asymmetric out-of-plane mode around the yaw axis. This will be referred to as the edgewise asymmetric mode in yaw since the blades are pitched 85 degrees. Similarly, the peak at 3.3 is the edgewise asymmetric mode in tilt. A second out-of-plane mode in yaw is visible at the normalized frequency of 9.5. just like the first mode, this oscillation is only visible when the azimuth angle of the measured blade is not in line with the tower.

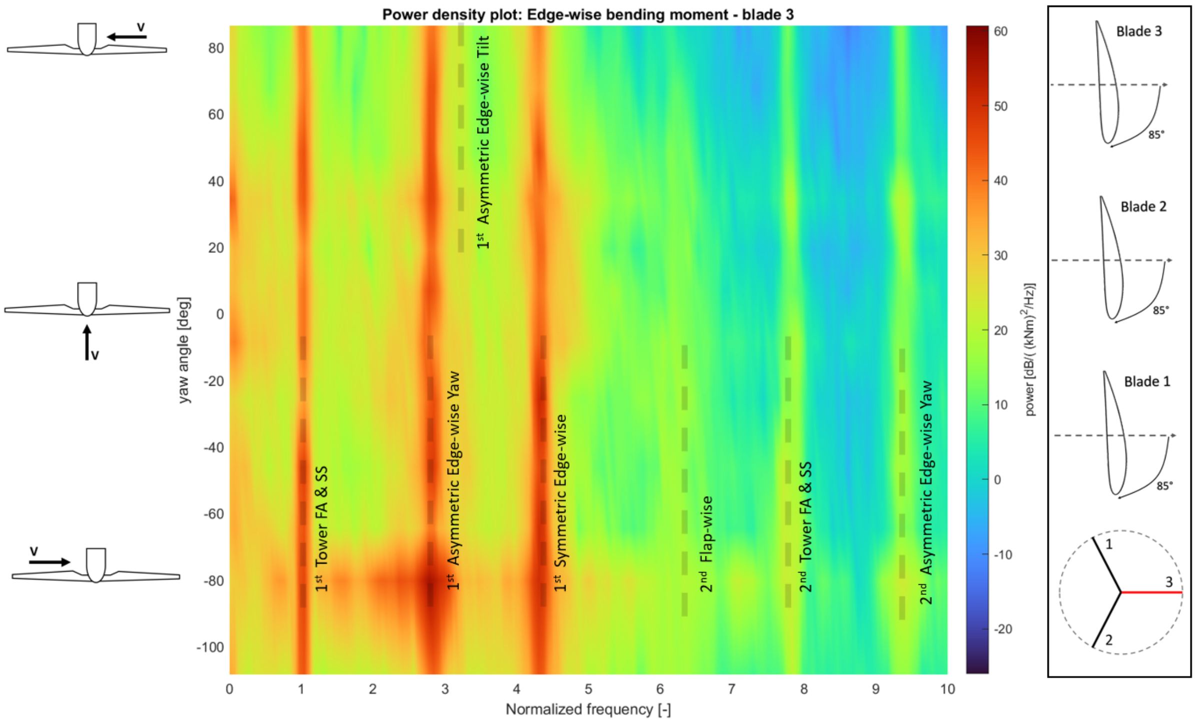

Figure 4.5: Power spectral density of the edgewise bending moment during yaw traverse, blade 3 at 90 degrees azimuth, note: severe gust during the test at -80 degrees yaw

Some of the natural frequencies of the turbine are dependent on the relative position of the blades, hence if the blades pitch the natural frequencies may change as well. This is clearly visible in Figure 4.6, where the peak at the normalized frequency of 4.4 splits up and moves towards 3.3 and 5.9. The peak that increases from 3.3 to 5.9 is also present in the flapwise moment and thus very likely a coupled mode between the edge and flapwise direction. The peak that decreases from 4.4 to a normalized frequency of 3.3 is only visible in the edgewise bending moment. This frequency is believed to be the symmetric edgewise frequency which admittedly no longer is fully symmetric when the blade is pitched away from the vane position of 85 degrees pitch. The shifting frequency of the peaks as one blade is pitched indicates that the coupling between the blades strongly affects their natural frequencies.

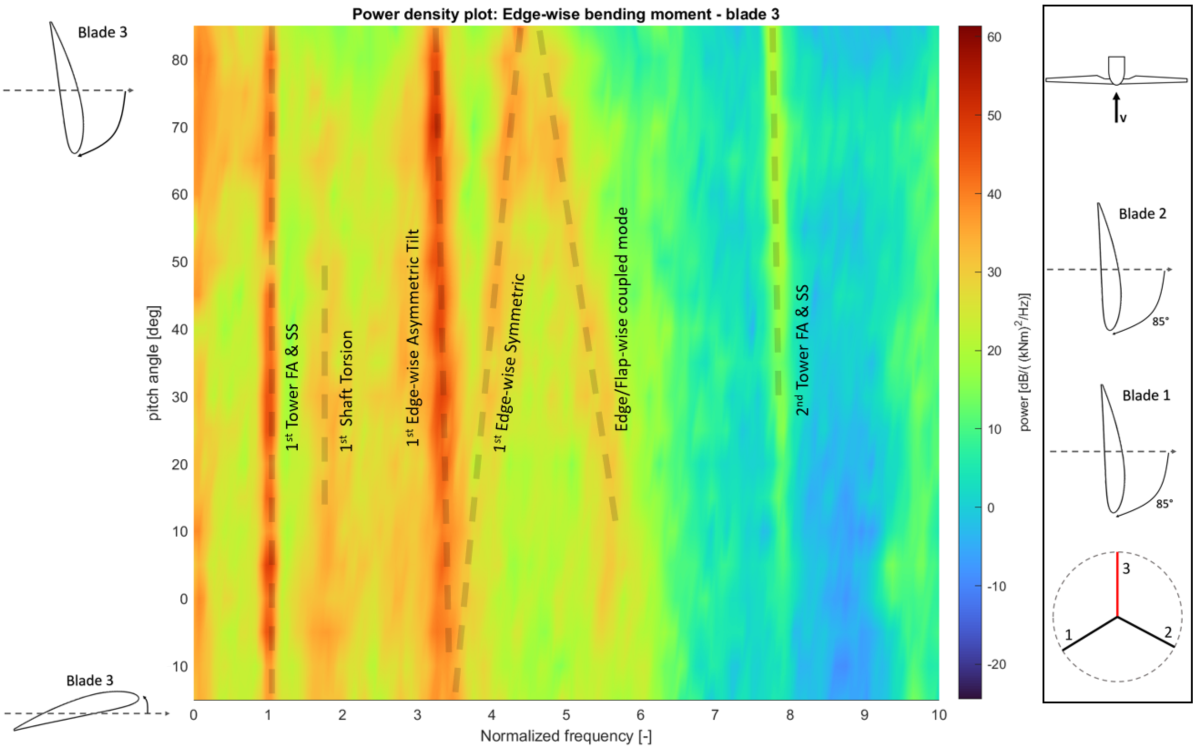

Figure 4.6: Power spectral density of the edgewise bending moment during pitch traverse of blade 3, blade 3 straight up, yaw of 0 degrees

Figure 4.7 Shows the response of the flapwise bending moment of blade 3 as it is pitched. As mentioned before, the peak which moves from 4.4 to 5.9 is visible in the flapwise direction as well, hence there is clearly some coupling between the blades. The second flapwise frequency from 6.2 also moves a little to combine with the other peak as the pitch angles approach 0 degrees.

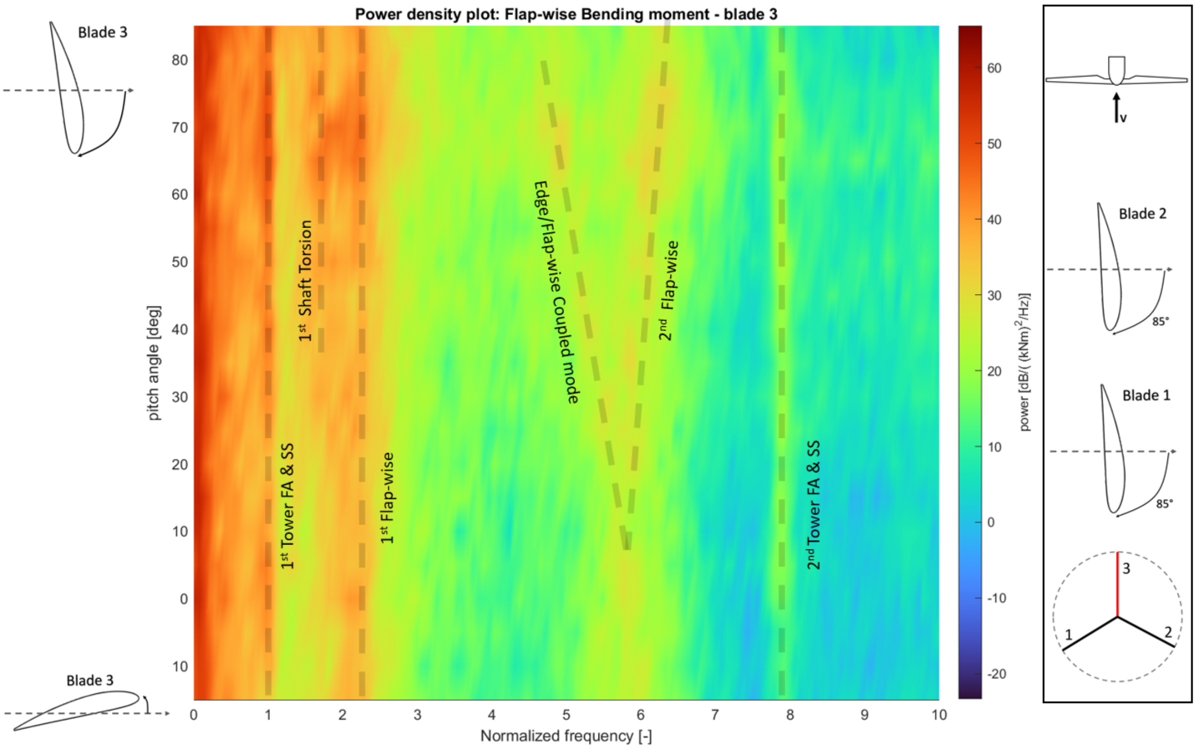

Figure 4.7: Power spectral density of the flapwise bending moment during pitch traverse of blade 3, blade 3 straight up, yaw of 0 degrees

The oscillation peak at 1.8 is present in both the edgewise direction and the flapwise direction when the blade is pitched such that the bending moment has a component in the lateral direction (xy-plane). This frequency is unlikely to be a tower mode since the first tower frequency is at 1. Due to how this oscillation is mainly present in the lateral direction, yet isn't a tower mode, it was concluded that the frequency might be due to the torsional natural frequency of the main shaft. This idea is further reinforced by Figure 4.8 showing the PSD of the main shaft torque, where the vibration with a frequency of 1.8 is clearly present. Furthermore, calculating the mode by hand using the equation below resulted in a close approximation, thus giving further confidence that this is the shaft's natural frequency.

$$f_n \approx \frac{1}{2\pi}\sqrt{\frac{q_{shaft}}{I_{rotor}}} \tag{4.1}$$

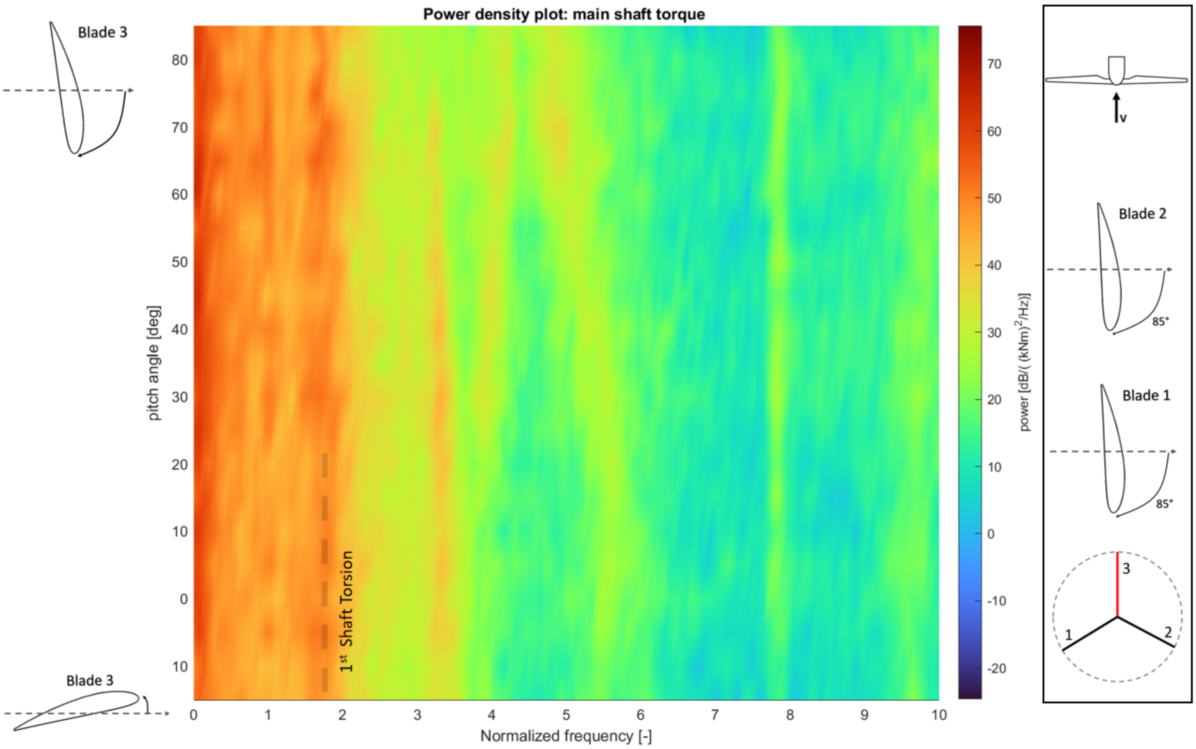

Figure 4.8: Power spectral density of the main shaft torque during pitch traverse of blade 3, blade 3 at 0 degrees azimuth, yaw of 0 degrees

4.4 The effect of windspeed

To quantify the effect of a higher wind speed, a yaw traverse has been performed on two different days (see experiments 5 and 6 in Table 4.1). The average wind speed changed from $14.3m/s$ to $19.1m/s$ while the average turbulence intensity only changed about 2%, from 11% to 13%. In case of the presence of a vortex shedding frequency (outside of lock-in), this should be visible as a shift in frequency.

Figure 4.9 and Figure 4.10 show the power spectral density plot of the edgewise moment and the tower normal moment for the two different wind speeds. The amplitude of the oscillations increased greatly as the wind speed increased. The frequency of these oscillations has shown no sign of shifting, which confirms the belief that these peaks are structural eigenfrequencies.

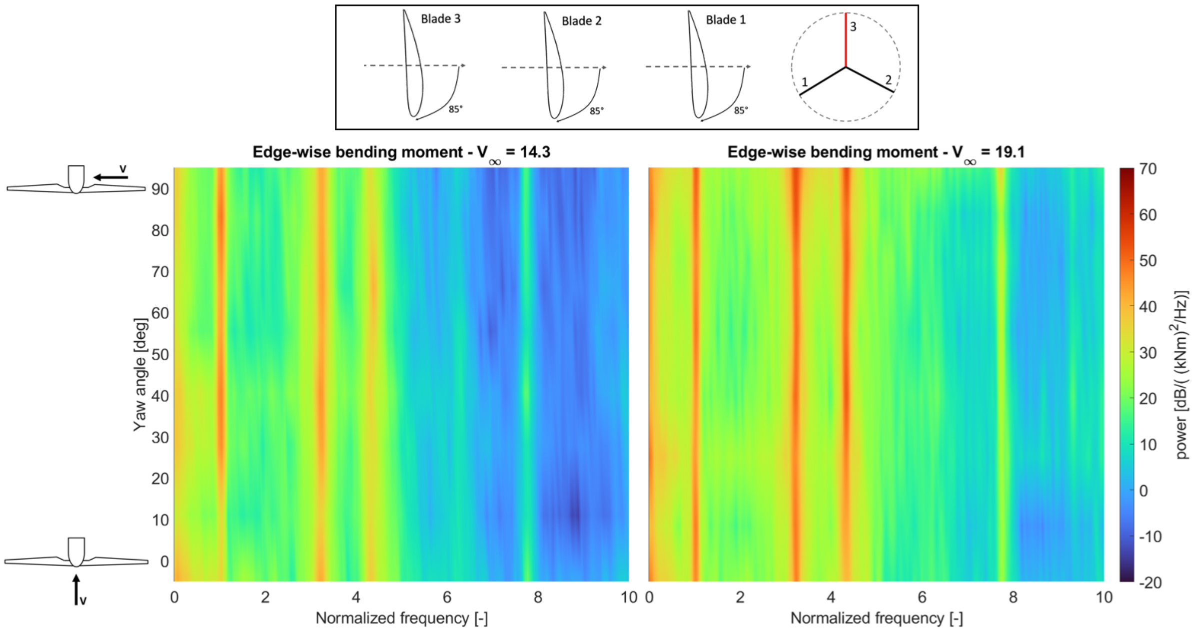

Figure 4.9: Edge-wise bending moment for yaw traverse 14.3m/s vs. 19.1m/s measured at the root of blade 3, which points up.

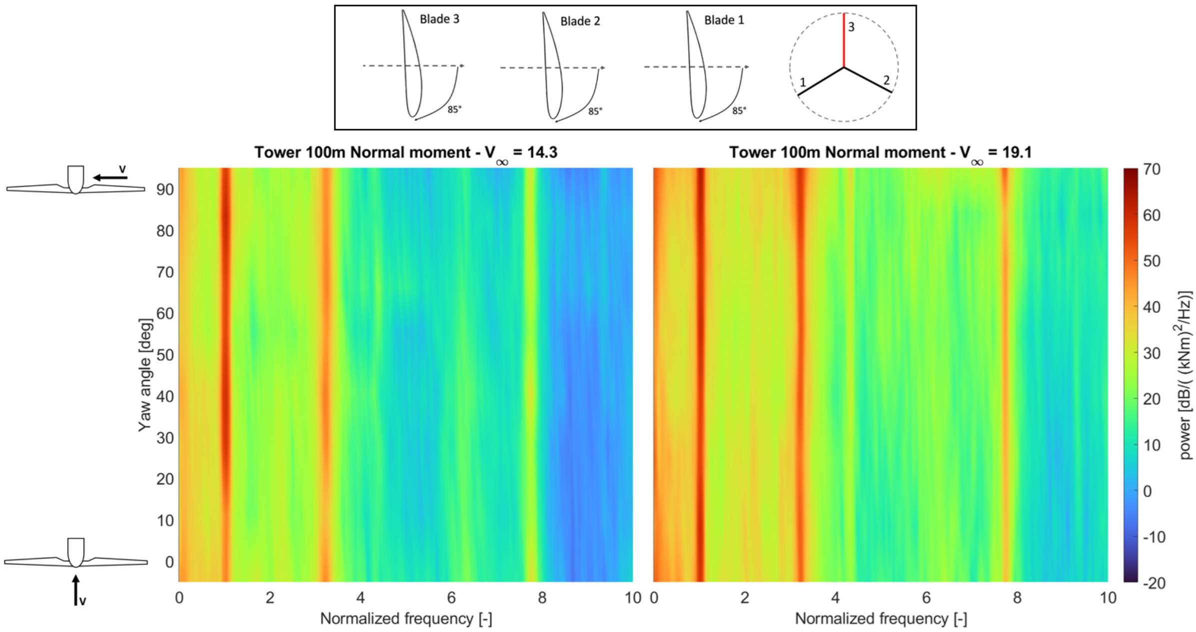

Figure 4.10: Tower normal moment (at 100m) for yaw traverse 14.3m/s vs. 19.1m/s

4.5 Stall induced vibrations

As mentioned in section 2.3, stall-induced vibrations are inherently due to how the forces change with respect to the operating conditions. This effect can be modeled as a negative aerodynamic damping which (partially) cancels out against the structural damping of the system. This phenomenon can be observed in the experiments by inspecting how the magnitude of the force oscillations changes as the pitch or yaw angle changes. An increase in the amplitude can signify a reduction in aerodynamic damping.

Changing the pitch angle should change the aerodynamic damping induced by the blade. This can be seen in the data where the amplitude of the oscillations at some frequencies are reduced. Figure 4.11

shows the PSD of the bending moments in the tower normal to the rotor. These bending moments are calculated from strain gauges placed 100 meters high. While the 1^{st} tower mode does not seem to be very affected, the oscillation corresponding with the asymmetric edgewise mode in tilt appears to be fully damped out as the pitch angle reduces. The peak of the second tower mode seems to reduce in amplitude when reducing the pitch angle. However, the peak corresponding to the $1st$ symmetric edgewise mode only shows up after the pitch angle is reduced. This is likely the case because when all three blades are in vane position, this mode cancels out between the blades. Whereas, when on blade is pitched away from vane position, this canceling will no longer happen and the tower will start to experience the oscillating force.

For a better idea of the relative size of the force oscillations, the FFT is plotted with a linear scale in Figure 4.12. The force oscillations with the highest amplitude appear to be the asymmetric edgewise mode in tilt, the first tower mode and the oscillations very close to 0, which are believed to be due to the wind. The oscillations corresponding to the asymmetric edgewise mode were the largest around 70 degrees pitch and damp out almost completely at 10 degrees pitch and below. The oscillations at the 1^{st} tower mode have however not shown a clear trend of changing due to the pitched blade. The 2^{nd} tower mode does appear to reduce in amplitude as the pitch angle is reduced.

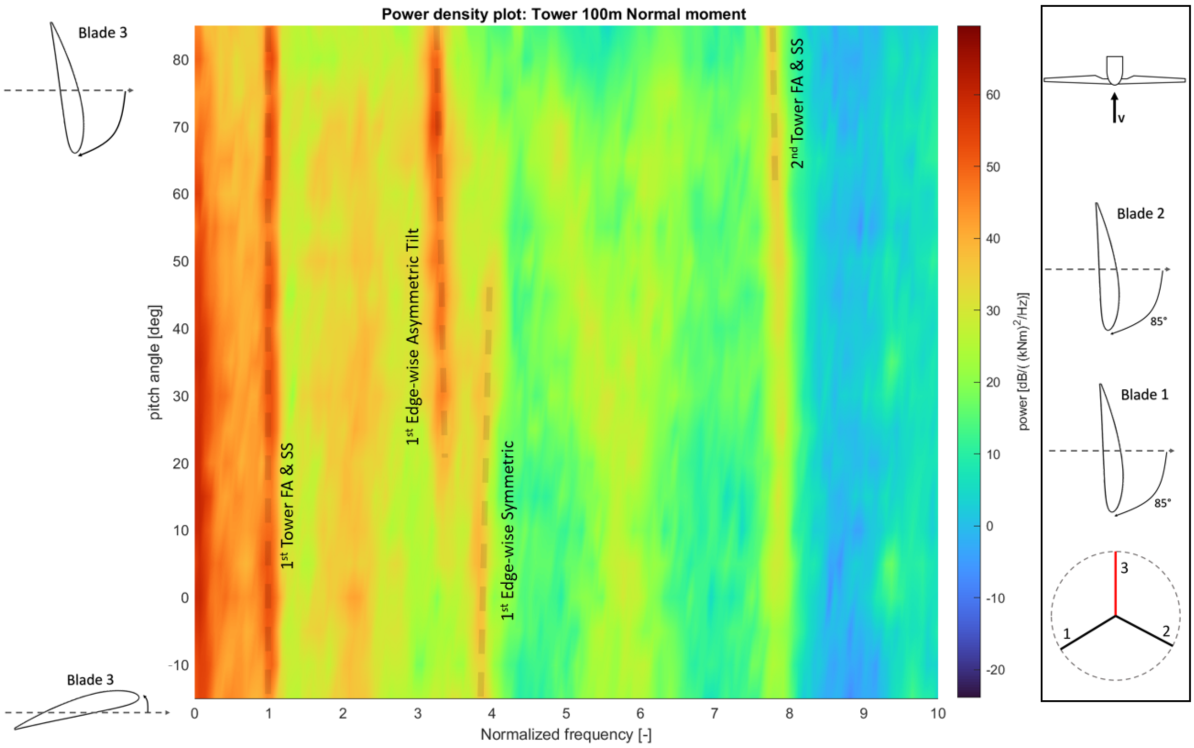

Figure 4.11: Power spectral density of the fore-aft bending moment of the tower at 100m high, blade 3 varies in pitch, yaw of 0 degrees

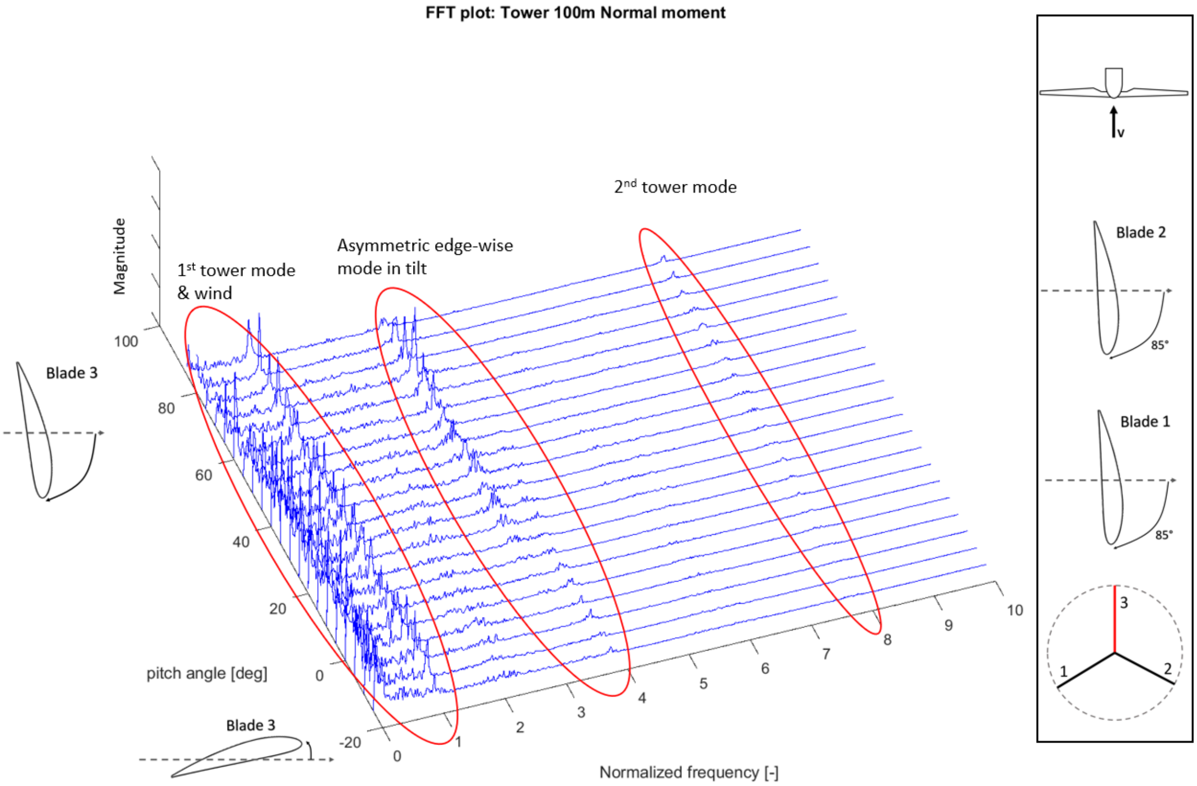

Figure 4.12: FFT of the Bending moment of the tower at 100m high, normal to the rotor plane, blade 3 varies in pitch, yaw of 0 degrees

A few experiments were performed in conditions where the wind turbine would experience much more severe vibrations. These experiments are numbers 8 and 9 in Table 4.1. The time series of test 8 is shown in Figure 4.13 with the test conditions shown in the box at the top. Near the end of the experiment, the vibrations became too severe to continue the experiment. The experiment was therefore stopped early by pitching blade 2 back to 120 degrees pitch.

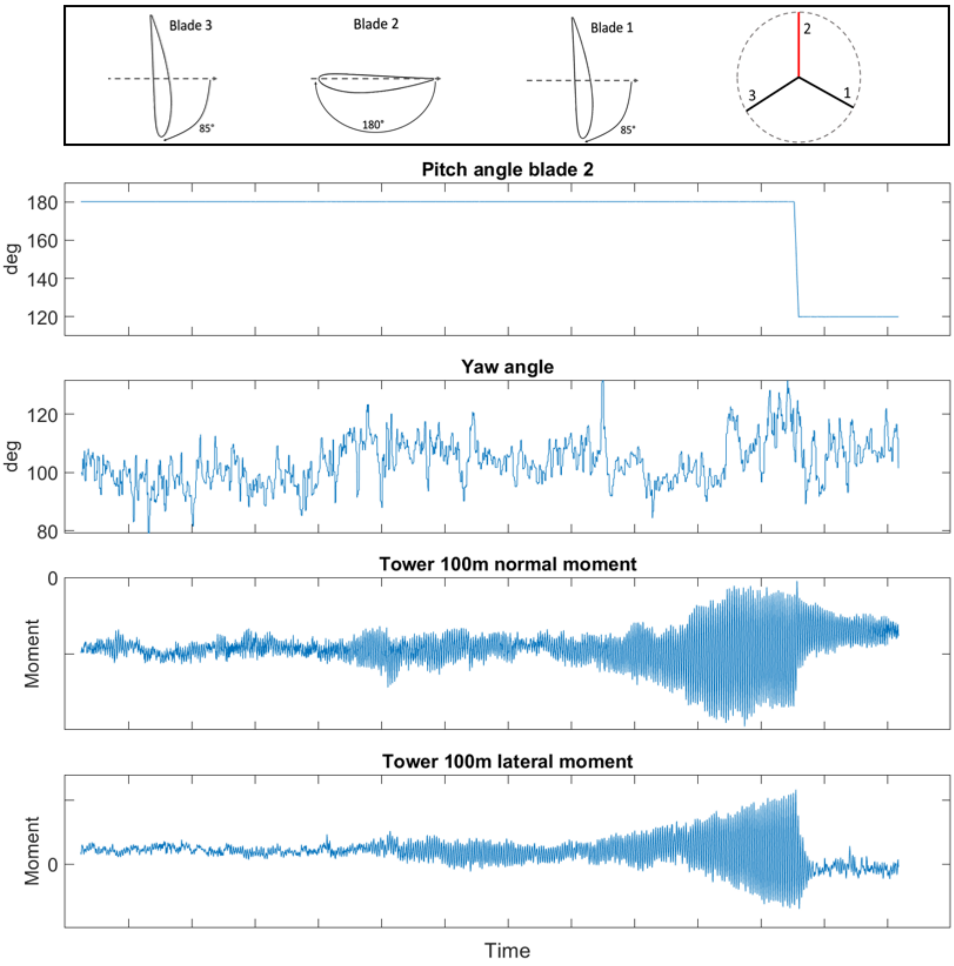

Figure 4.13: Bending moment oscillations in the blade during SIV test with blade 2 at 180 degrees pitch with $V_{mean} = 19.5m/s$ and $Ti = 14\%$

Figure 4.13 Shows how the oscillations started increasing in amplitude once a high enough yaw angle was achieved. During this experiment, the tower was also visibly shaking with increasing amplitude until the pitch angle was adjusted. This fast growth in amplitude indicates the presence of negative aerodynamic damping with severe SIV as a result. It is uncertain if vortex shedding also plays a role, but considering the seemingly exponential growth in oscillations and the sensitivity to the wind speed (see Figure 4.19) SIV very likely to be of significant influence in this experiment. The condition of the wind turbine where this behavior was identified was with one blade straight up, at a pitch angle of 180 degrees, and the other two blades were positioned in a feather position of 85 degrees pitch. under these conditions, serious SIV occurred when the yaw angle approached 110 degrees.

After pitching blade 2 back to 120 degrees pitch, most vibrations damped out quite quickly. The tower bending moment oscillations in the lateral direction damped out almost instantly, while the normal direction damped the oscillations much slower. This is likely because the tower has less aerodynamic damping in the fore-aft direction when the blades are in vane position.

When plotting this data in the frequency domain, the amplitude is averaged over some time and the growth over time is therefore not as nicely visualized. However, it is still interesting to visualize which modes were amplified the most. In the Figure 4.14 it is clear that while all frequencies seem to grow in magnitude, the first natural frequency of the tower is dominant. The first tower mode is thus the most excited by these conditions of SIV.

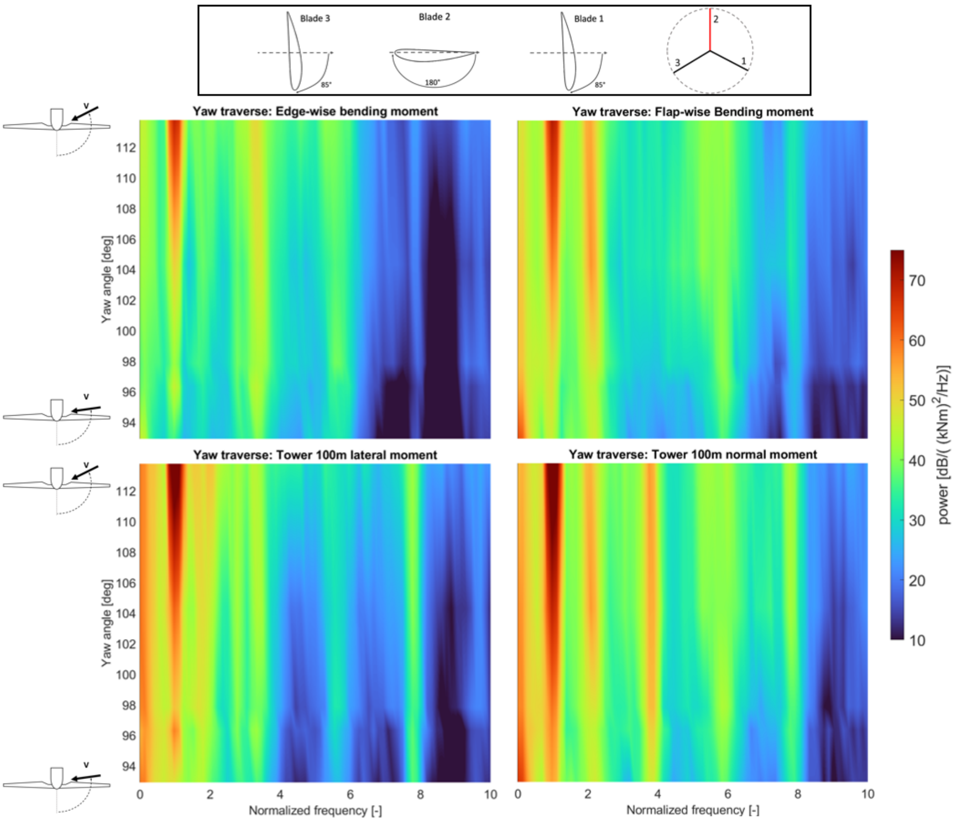

Figure 4.14: PSD of the blade and tower moments during SIV test with blade 2 at 180 degrees for a mean wind speed of $19.5 m/s$ with $Ti = 14\%$

To get a better physical understanding of the system, it may be useful to compare the phases of several signals. Figure 4.16 shows the bending moment time series for a rather short period of time during the greatly increased oscillations of experiment 8. The tower bending moment is clearly dominated by oscillations in a single frequency. The phase shift between the fore-aft (normal) mode and the side-side (lateral) mode is 150 degrees. If this directly correlates to the displacement, the tower would oscillate in an oval shape as visualized in Figure 4.15.

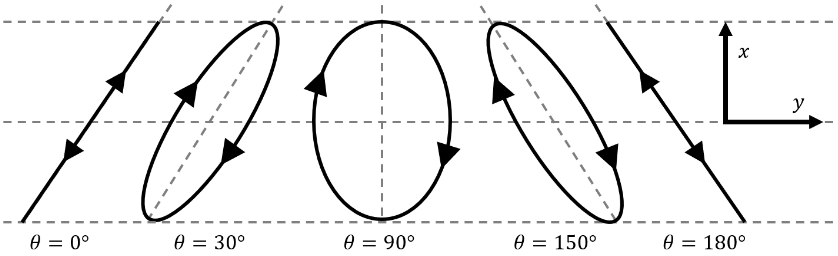

Figure 4.15: Oscilation shapes of two perpendicular modes with the same frequency and different amplitude for various phase shift angles θ

The blade bending moments do clearly experience oscillations at different frequencies, but with the same tower frequency still being the most dominant. The phase shift between the edge-wise signal from blade 2 and the tower lateral oscillations is about 185. The phase shift between the flapwise bending moment and the tower fore-aft oscillations is 180 degrees. This correlation makes sense as, with the blade pitched at 180 degrees, the edge-wise direction aligns with the lateral direction and the flap-wise direction is aligned with the normal motion (fore-aft) of the tower. The 180 degree difference is likely explained by the positive and negative directions being flipped between the blade and tower.

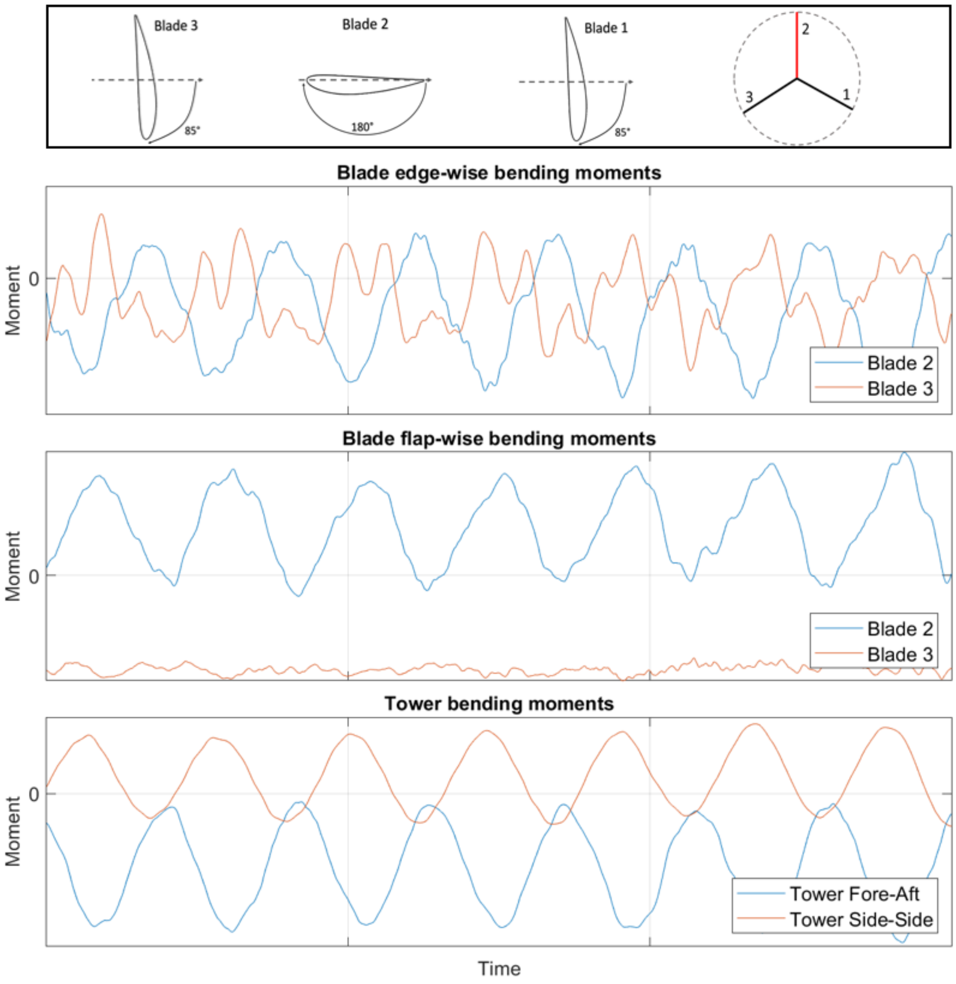

Blade edge-wise bending moments

Blade flap-wise bending moments

Tower bending moments

Figure 4.16: Bending moment oscillations in the blade during SIV test with blade 2 at 180 degrees pitch with $V_{mean} = 19.5m/s$ and $Ti = 14\%$

Another experiment was performed later on the same day. Unlike the experiment discussed above, blade 3 was at 180 degrees pitch and the yaw angle was slowly reduced instead of increased. Lastly, the windspeed and turbulence intensity had dropped quite a bit from $19.5m/s$ with $Ti = 14\%$ to $16.6m/s$ with $Ti = 11\%$. The change in conditions was significant enough that the experiment did not need to be cut short due to force oscillations of excessive magnitude, but SIV was still present. The time series from this experiment is shown in Figure 4.17. The oscillations still increased in amplitude for some yaw angles, but the increase in magnitude was not as severe as in the previous experiment.

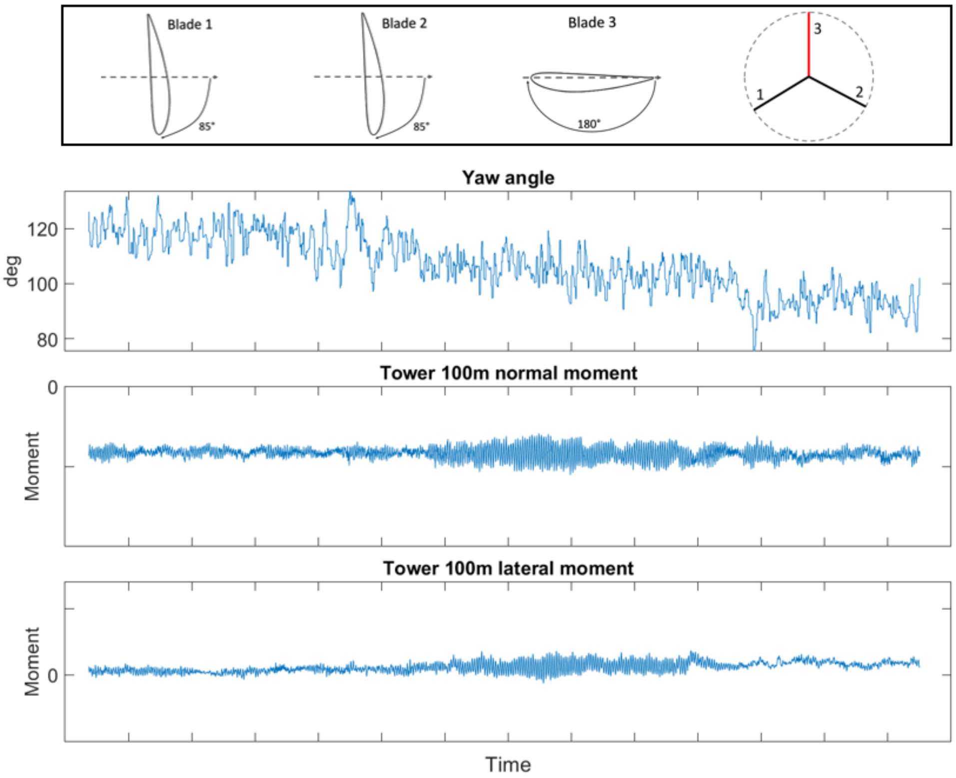

Figure 4.17: Bending moment oscillations over a short period of time to identify the phase shift between signals $V_{mean} = 19.5m/s$ and $Ti = 14\%$

Figure 4.18 shows the PSD of this second experiment for SIV. Once again it can be noticed that while several modes increase in magnitude, the most dominant mode appears to be the first tower mode at the normalized frequency of 1. Unlike the first experiment, this time the force oscillations did not continue to grow to dangerous magnitudes. Because of this, the yaw traverse could be continued until past the yaw angle where the oscillations occurred.

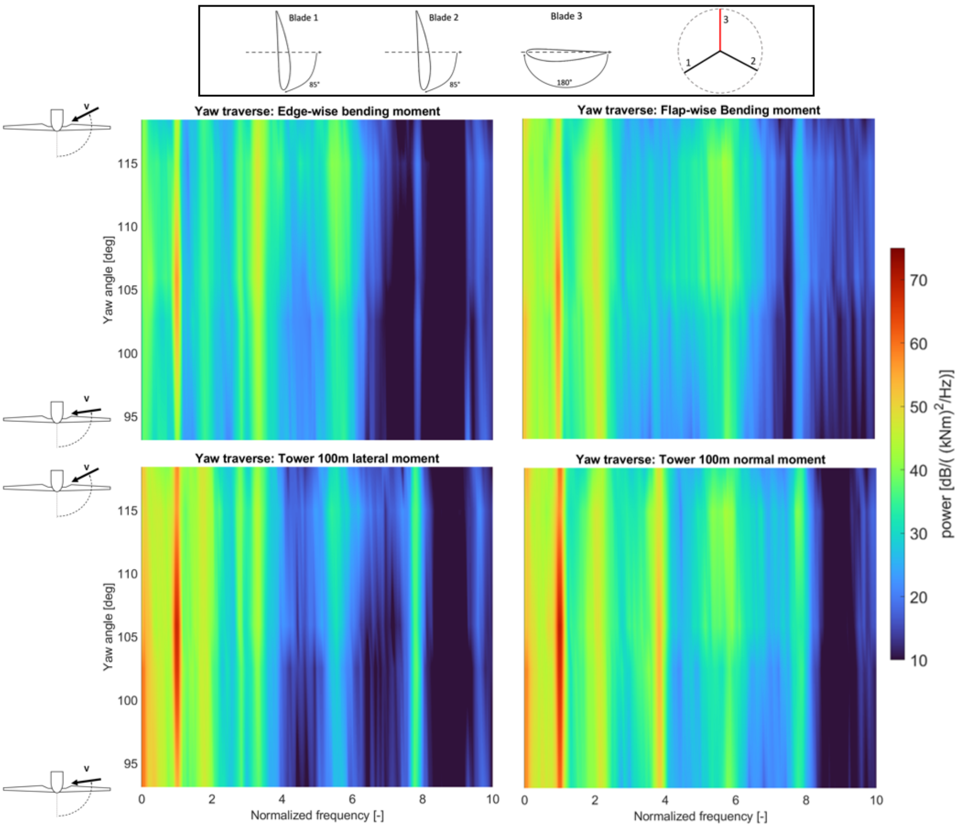

Figure 4.18: PSD of the blade and tower moments during SIV test with blade 3 at 180 degrees for a mean wind speed of $16.6m/s$ with $Ti = 11\%$

Directly comparing the power in the measured systems, Figure 4.19 shows the power obtained by integrating the entire PSD of the various signals for both tests 8 and 9. The experiment with wind speeds around $19.5m/s$ experienced a much larger growth in power compared to the experiment with wind speeds around 16.6. This indicates that in the more extreme conditions, the negative aerodynamic damping may have a much more significant effect on the dynamics of the wind turbine.

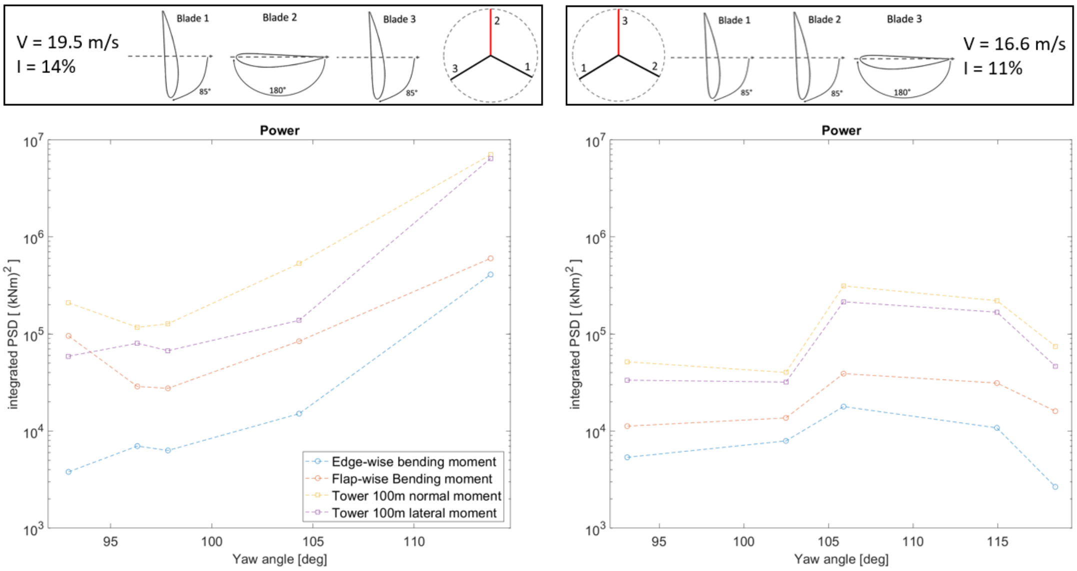

Figure 4.19: Integrated Power comparison for the SIV test with one blade at 180 degrees pitch, $19.5m/s$ with $Ti = 14\%$ vs. $16.6m/s$ with $Ti = 11\%$

4.6 Vortex shedding

In the data from the bending moments, there were no oscillations visible which could be identified as a vortex-shedding frequency. Hence it is likely that if vortex shedding does occur, all the energy is fed into one of the natural frequencies. Pressure sensors are located along the airfoil of blade 3, located 15 meters from the root. These sensors may provide a better understanding of which frequencies are present in the aerodynamic forces, and thus help identify the presence of vortex shedding.

The power spectral density of the pressure is plotted in Figure 4.20, 4.21 and 4.22 for three different downwind locations along the chord. These results are obtained from the yaw traverse of experiment 6 (see Table 4.1), but to improve visualization, it has been plotted with respect to the angle of attack for blade 3. All three plots show clearly the presence of much higher pressure variation for some angles of attack. However, there is not a clear vortex shedding frequency, as all regions of increased fluctuations are spread out over a rather broad range of frequencies. That said, it is clear that for angles of attack between -110 and -150 the air experiences much higher pressure fluctuations. If there was structured vortex shedding, a single frequency should have a clear peak. Considering the windspeed of $19.1 m/s$ and a Strouhal number of between 0.15 and 0.2, the vortex shedding normalized frequency should have been between 3 and 4 at the root of the blade when the angle of attack is 90 degrees.

The broad range of excited frequencies in the pressure oscillation leads to the belief that the flow separates in a stochastic manner, resulting in no specific vortex shedding frequency. The sensors are likely much more exposed to these oscillations in pressure when close in proximity to the point of separation. The pressure sensor near the leading edge, see Figure 4.20, experiences much greater fluctuations at -40 degrees angle of attack likely because of this. Similarly, the greatly increased fluctuations due to the separation region can be seen near the trailing edge at -170 degrees in Figure 4.22

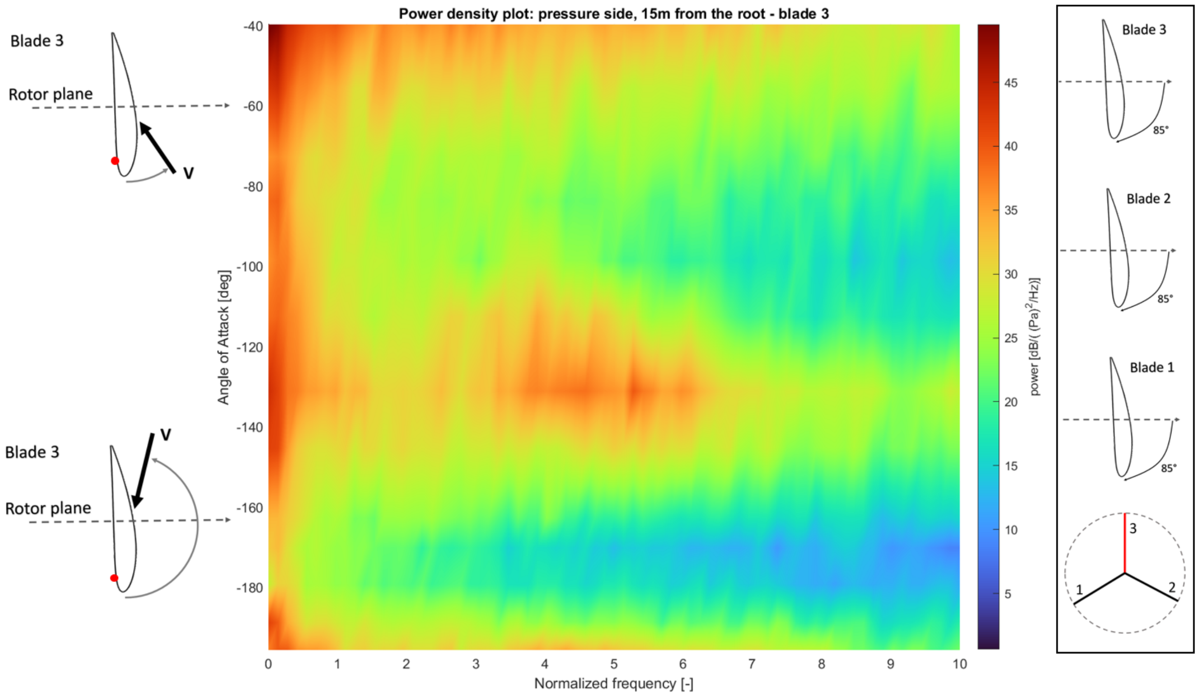

Figure 4.20: Frequency response in dB for the pressure measured near the leading edge of blade 3 during a yaw traverse of blade 3, measured in downwind direction 15 meters from the blade root

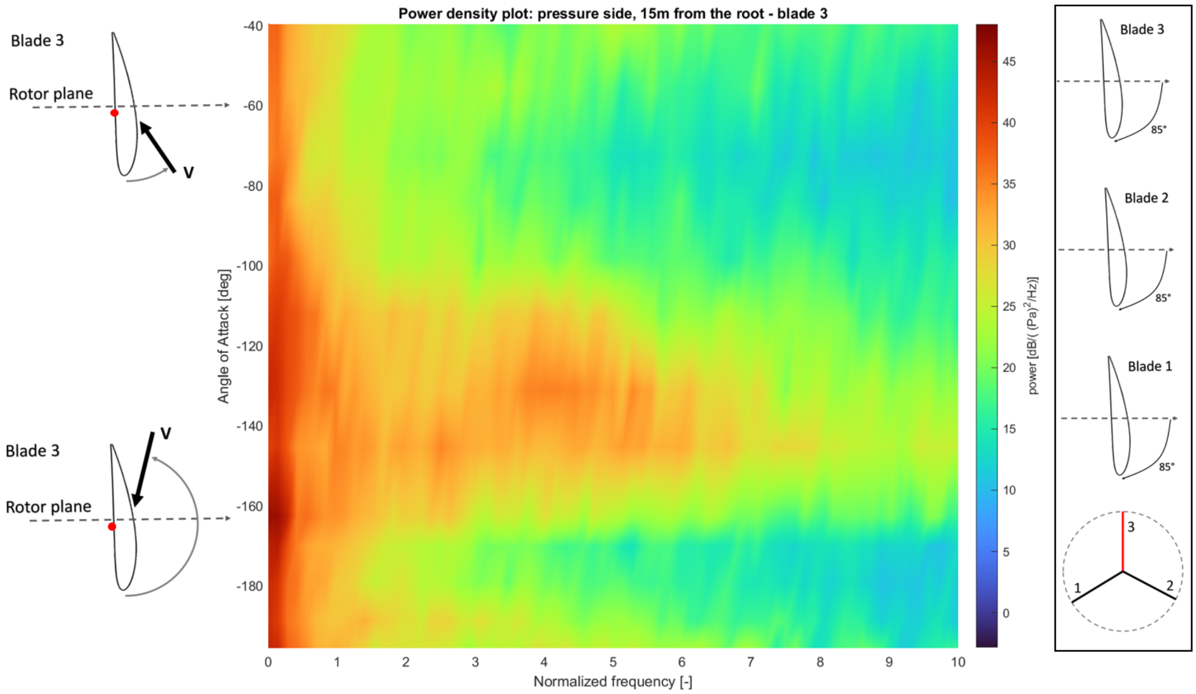

Figure 4.21: Frequency response in dB for the pressure measured near the middle of the chord of blade 3 during a yaw traverse of blade 3, measured in downwind direction 15 meters from the blade root

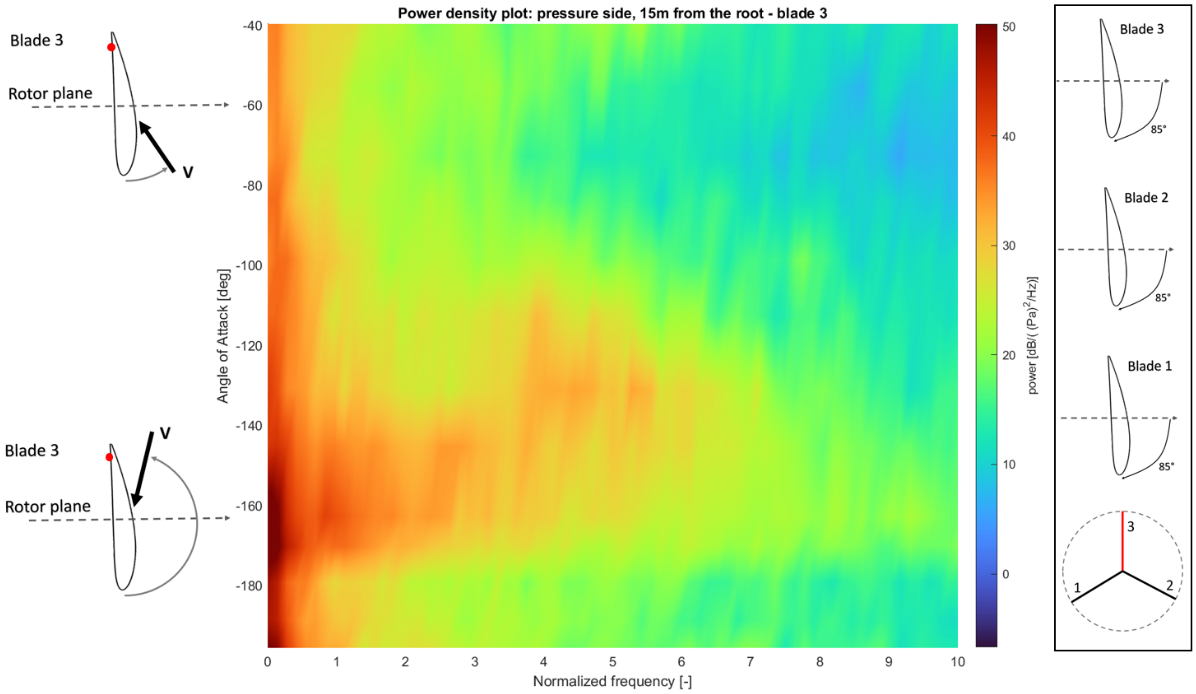

Figure 4.22: Frequency response in dB for the pressure measured near the trailing edge of blade 3 during a yaw traverse of blade 3, measured in downwind direction 15 meters from the blade root

4.7 The effect of coupling

As mentioned before in section 4.3, the structural behavior of the blade frequencies appears to be strongly coupled with their relative position/pitch angle. Varying the pitch of a single blade not only affects the aerodynamic damping of the turbine but also the structural frequencies to which it is sensitive.

Figure 4.23 compares the force oscillations for the same local angle of attack for blade 3 caused by either changing the pitch angle or yawing the entire rotor.

At an angle of attack of 5 degrees, both the conditions and results for both the pitch traverse and yaw traverse are the same. It is at 5 degrees because there, all blades are at 85 degrees pitch and the yaw angle is 0 degrees. However for any other angle of attack, the pitch and yaw traverse experience the same flow over the top blade (at 0 degrees azimuth), but experience different conditions over the remaining blades and nacelle. In Figure 4.23 it is seen that the pitch traverse causes some of the blade's excited modes to shift, while for the yaw traverse, they remain at a constant frequency. The tower frequencies at 1 and 7.9 do not appear to shift due to the pitch traverse. For the edge-wise bending moment, the peak of the asymmetric edgewise mode in tilt becomes more broad and ends up merging with the symmetric edgewise mode. During the yaw traverse these edge-wise modes remain quite narrow. There are also some peaks present in the pitch traverse which are not visible during the yaw traverse. This becomes more clear in Figure 4.24 where the power spectrum is plotted for the edgewise bending moment for 5 and 55 degrees. At 55 degrees angle of attack, there are 4 additional modes visible in the yaw traverse: the rotor shaft, the 1st flapwise mode, the edge-wise asymmetric mode in yaw, and a flap/edge-wise coupled mode. Also, the shifting peaks are visible.

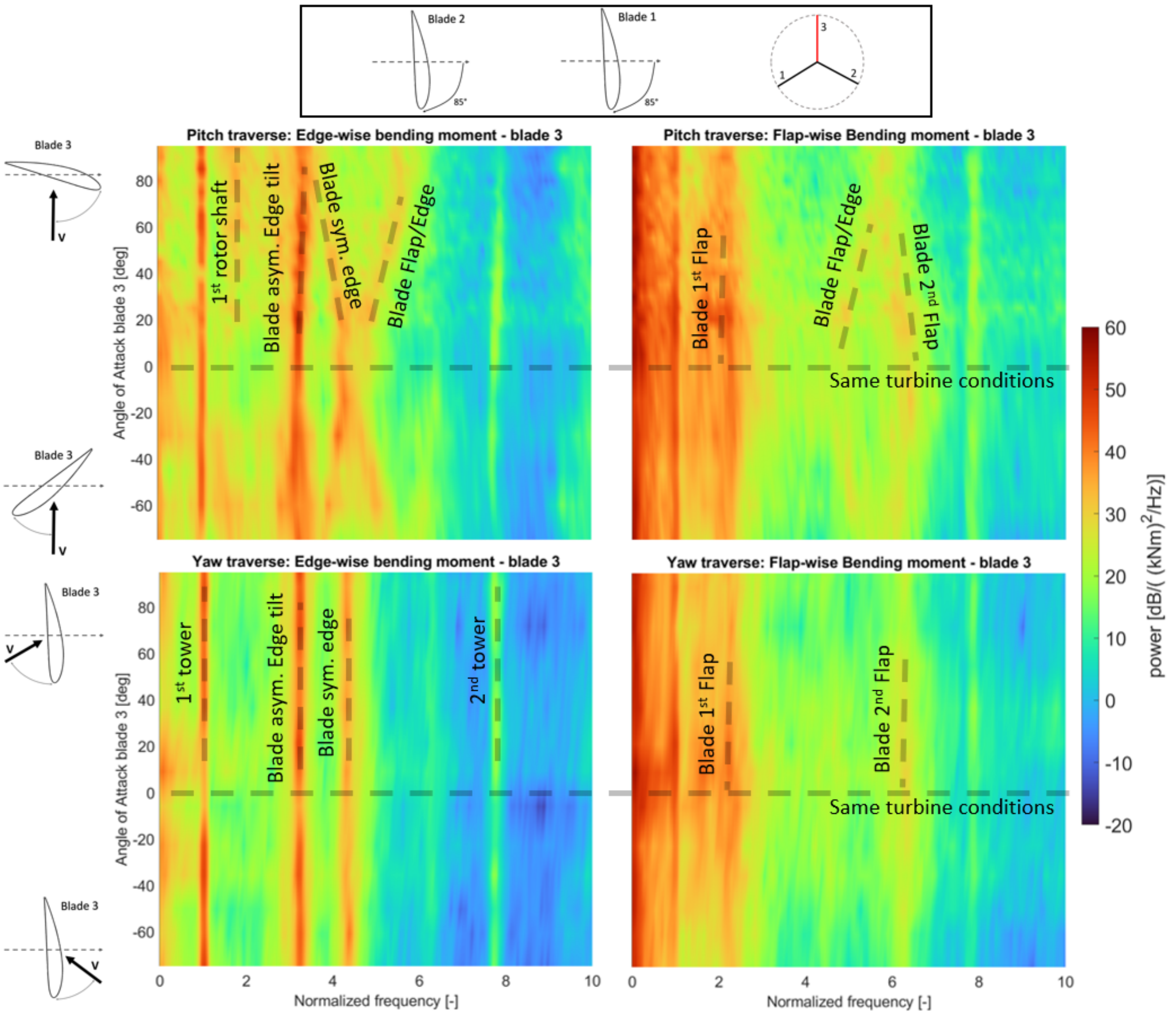

Figure 4.23: Blade flap and edge-wise bending moment vs angle of attack, for both a pitch traverse (top) and a yaw traverse (bottom)

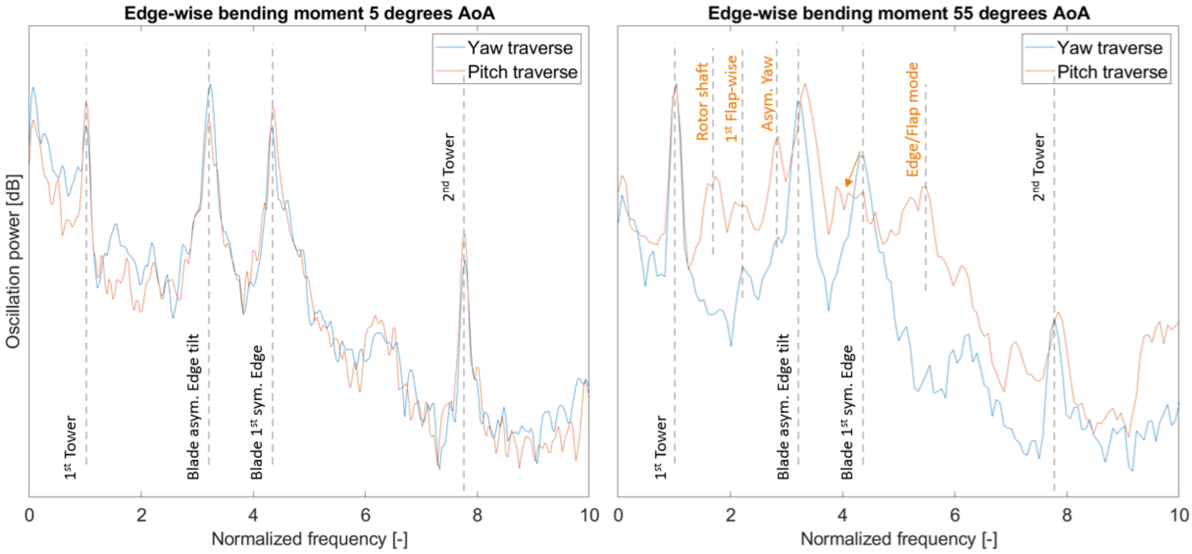

Figure 4.24: Edgewise bending moment at 5 and 55 degrees angle of attack, for both a pitch traverse and a yaw traverse

Figure 4.25 shows how these conditions affect the tower bending moment. At 0 degrees angle of attack the conditions and resulting oscillations are very similar. But just like the loads on the blade, the shifting natural frequencies from the pitch traverse are transferred to the tower. This effect therefore clearly affects the dynamics of the entire wind turbine. An interesting difference between the pitch traverse and yaw traverse is that the tower normal modes are damped more in the pitch traverse, resulting in smaller oscillations than in the yaw traverse for angles away from 0 (e.g. +60 and -60 degrees)

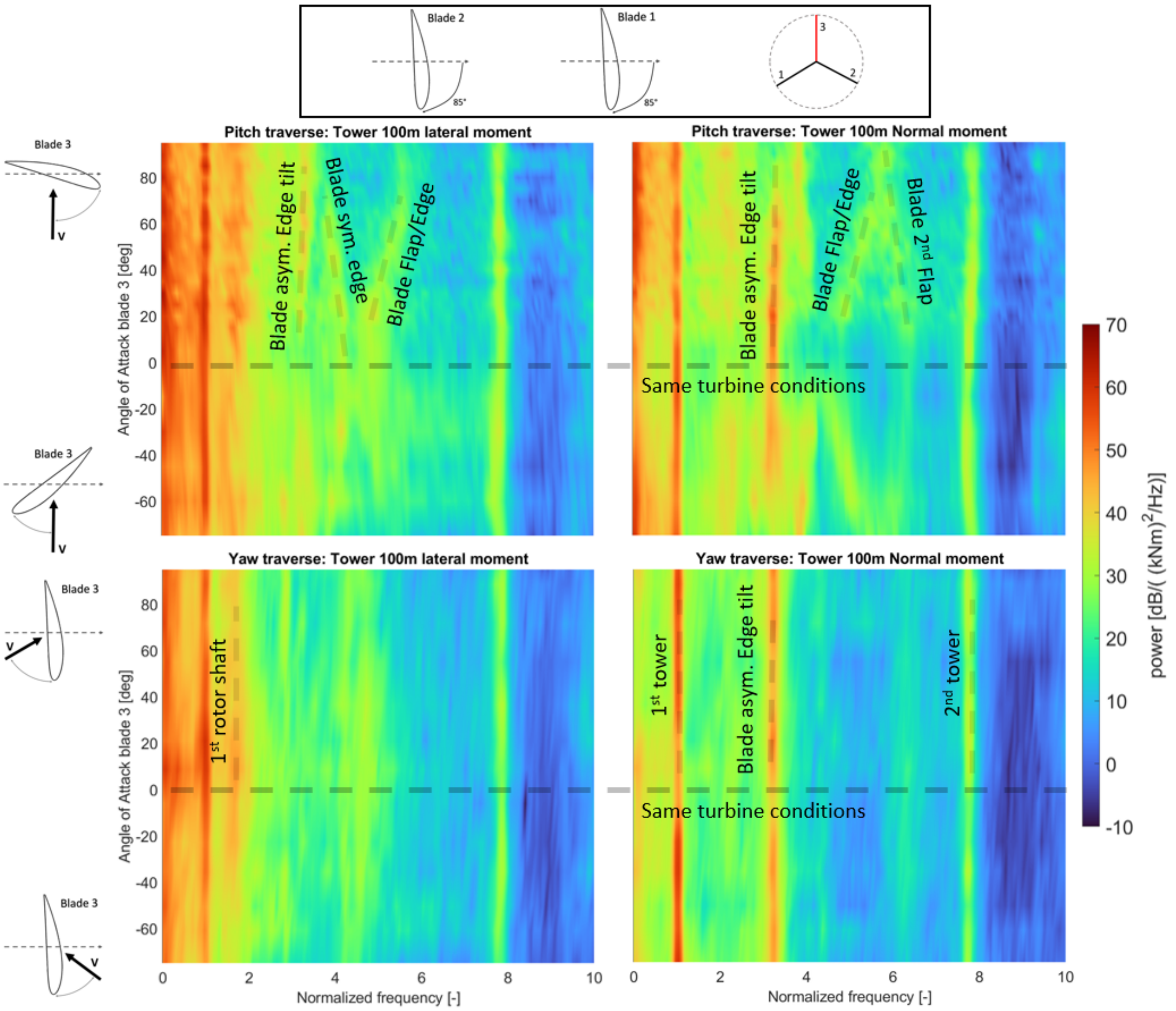

Figure 4.25: Tower normal and lateral bending moment at 100m vs angle of attack, for both a pitch traverse (top) and a yaw traverse (bottom)

4.8 Azimuthal traverse

Some situations where the blade experiences a high inclination angle were identified to possibly result in VIV in other literature. This experiment aims to measure the oscillating loads in the blade as the azimuth angle varies with a yaw misalignment of 90 degrees. This will result in varying inclination angles and with that, reduced normal flow and increased radial flow. Figure 4.26 shows how the inclination angle is defined as the angle between the incoming flow and the axis perpendicular to the blade. This is defined this way, such that an inclination angle of 0 degrees results in no flow in the radial direction, and an angle of 90 degrees will only have flow in the radial direction.

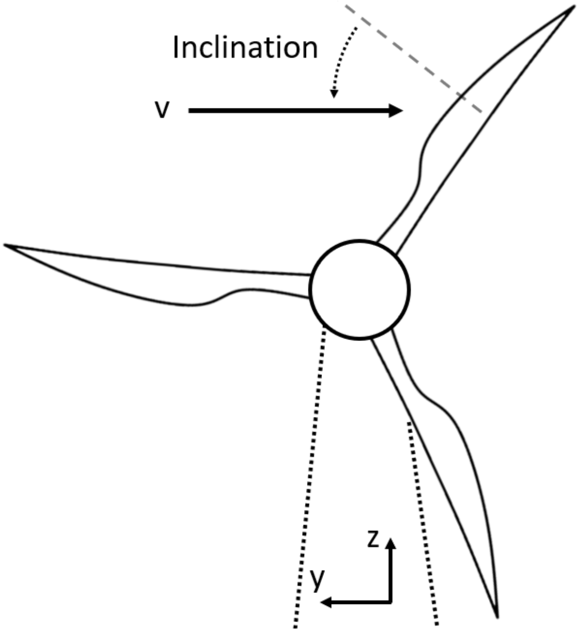

Figure 4.26: Inclination angle of the wind with respect to an axis perpendicular to the turbine blade. Due to 90 degrees yaw misalignment this is in the y-z plane and equal to the azimuth angle of the blade

Experiment 10 from Table 4.1 tested the azimuth traverse at about 90 degrees yaw. Because of this, the inclination angle is equivalent to the local blade azimuth angle. The exception to this would be after it passes 90 degrees. After an inclination angle of 90 degrees, the wind approaches the other side of the blade, reversing the pressure side and suction side. For the sake of visualizing the results without creating too much confusion, everything is defined with respect to the conditions at a blade azimuth of 0 degrees (which is also an inclination angle of 0 degrees). Angles beyond 90 degrees are continued to count up until 120 degrees where the experiment stopped. The wind will approach the blade from the other direction for these 30 degrees. The PSD of this experiment is presented in Figure 4.27.

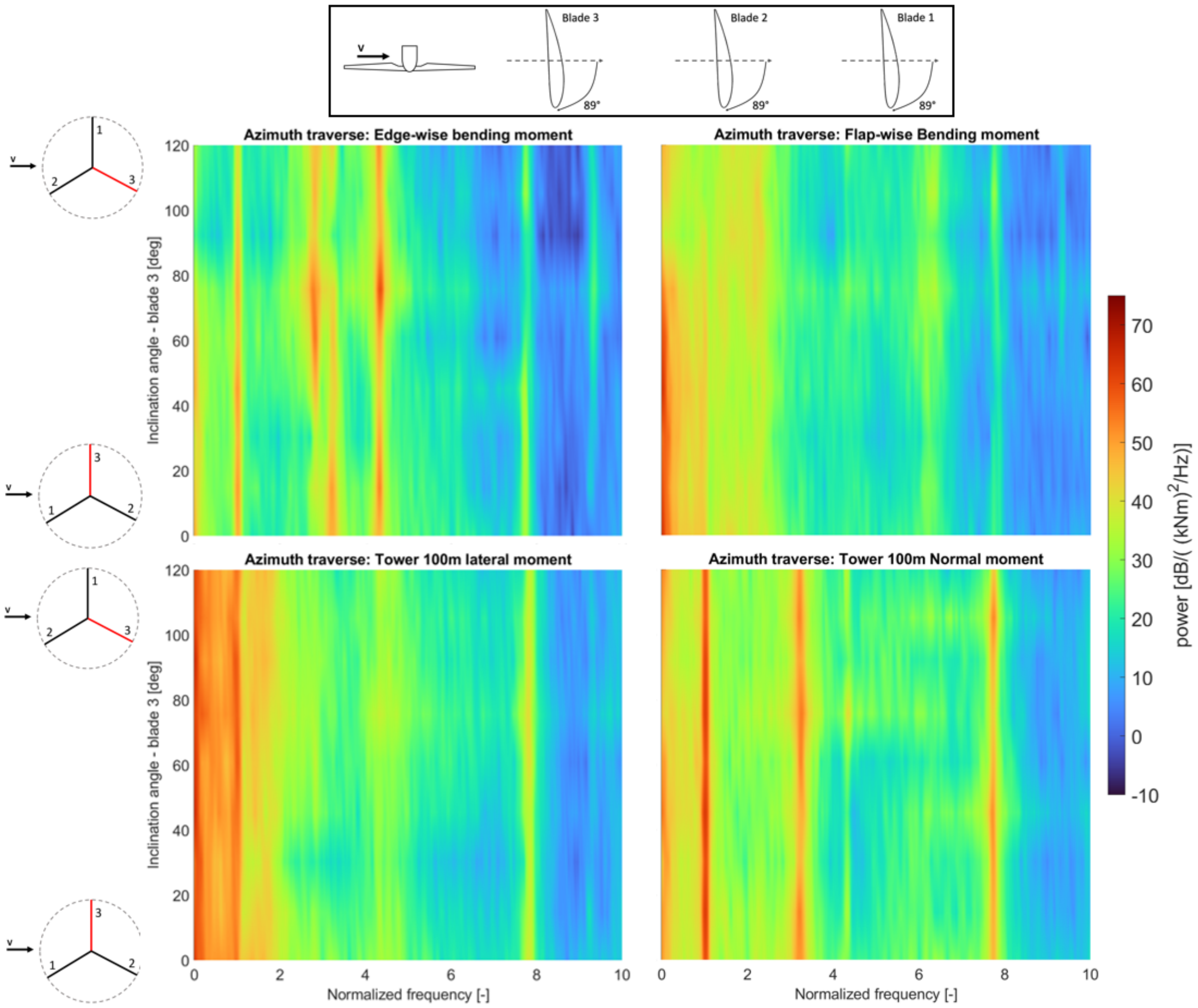

Figure 4.27: Power spectral density of the blade root edgewise bending moment(top left), flapwise bending moment (top right), tower 100 m lateral moment, and tower 100m normal moment during an azimuth traverse, $V \approx 19.2 m/s$, $Ti = 14\%$ at -90 degrees yaw

Figure 4.27 clearly shows no relation between the frequency and the azimuthal angle other than the presence or absence of the asymmetric edgewise mode at the normalized frequencies of 2.9 and 3.3 as discussed in section 4.3.

The most notable peak in the blade edge-wise bending moment PSD is located around the inclination angle of 75 degrees.Figure 4.28 also shows the presence of another peak at the azimuth angle of 45 degrees. Only the pressure sensor near the mid-chord location is plotted, but this data is consistent with the other pressure sensors. Noteworthy is that this peak at an inclination angle of 45 is absent in the bending moment PSD data. This rather broadband peak in the pressure oscillations appears on the suction side of the blade, i.e. behind the blade where the air is most likely fully separated. The inclination angle might be such that the wake of the measured blade sticks closer to the blade, resulting in unstructured stochastic pressure measurements of the highly turbulent flow.

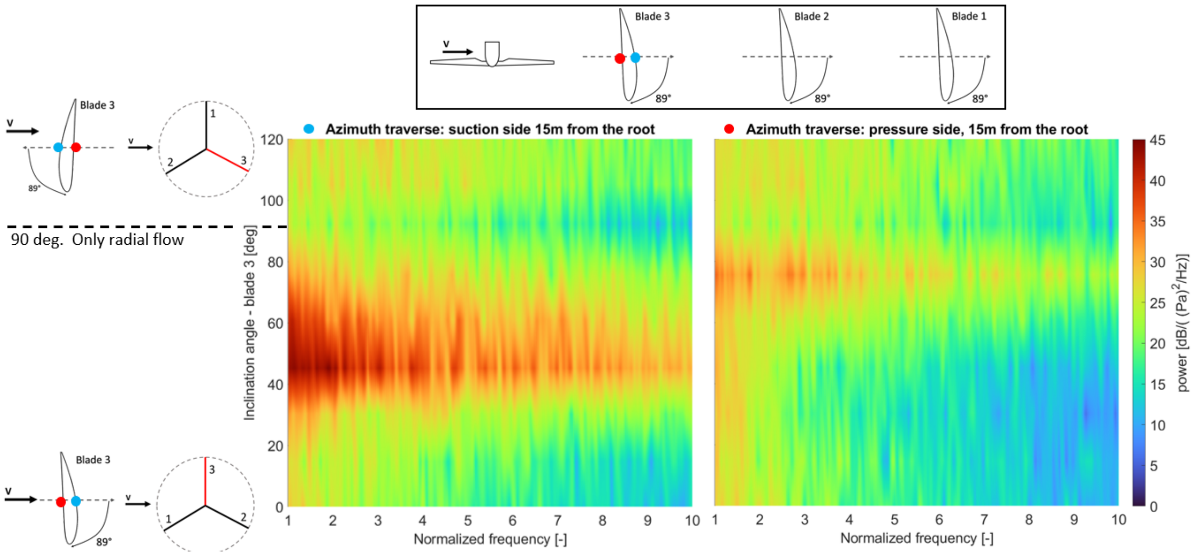

Figure 4.28: Power spectral density of the pressure variations measured 15m from the root on blade 3, at the mid chord, during an azimuth traverse, $V \approx 19m/s$, $Ti = 13.6\%$ at -90 degrees yaw

Looking further into this, Figure 4.29 shows the integrated power obtained from the PSD, as well as the mean bending moment from the inclination angle traverse. The standard deviation (std) of the data plotted bottom left follows the same trend as integrating the PSD. The oscillations in the edgewise bending moment experience a clear peak in power at a 75-degree inclination angle. Conversely, the power in the flapwise bending moment starts to drop off at about 75 degrees. At very high inclination angles, both edgewise and flapwise load sensors measure little power, likely because the wind mainly flows radially resulting in lower loads.

The mean bending moment is interesting as it gives some insight into the magnitude of the incoming forces with respect to the experienced oscillations. Here a clear dip is visible for the edgewise bending moment at 45 degrees inclination. The average edgewise bending moment was lower therefore lower in these conditions, when the power is divided by this mean, a peak is visible at 45 degrees. This effect appears to only affect the edgewise bending moment. This shows that the power of the edgewise vibrations is likely strongly coupled with the forces in other directions. It may also be possible that this was influenced by the tip vortex of blade 1. As the inclination angle of blade 3 is tilted downwind it may experience some of the wake of the rest of the rotor. The lack of a clear peak in the power of any oscillation at 45 degrees supports the idea that the pressure fluctuations as shown in Figure 4.28 were the result of unstructured turbulence and not structured vortex shedding.

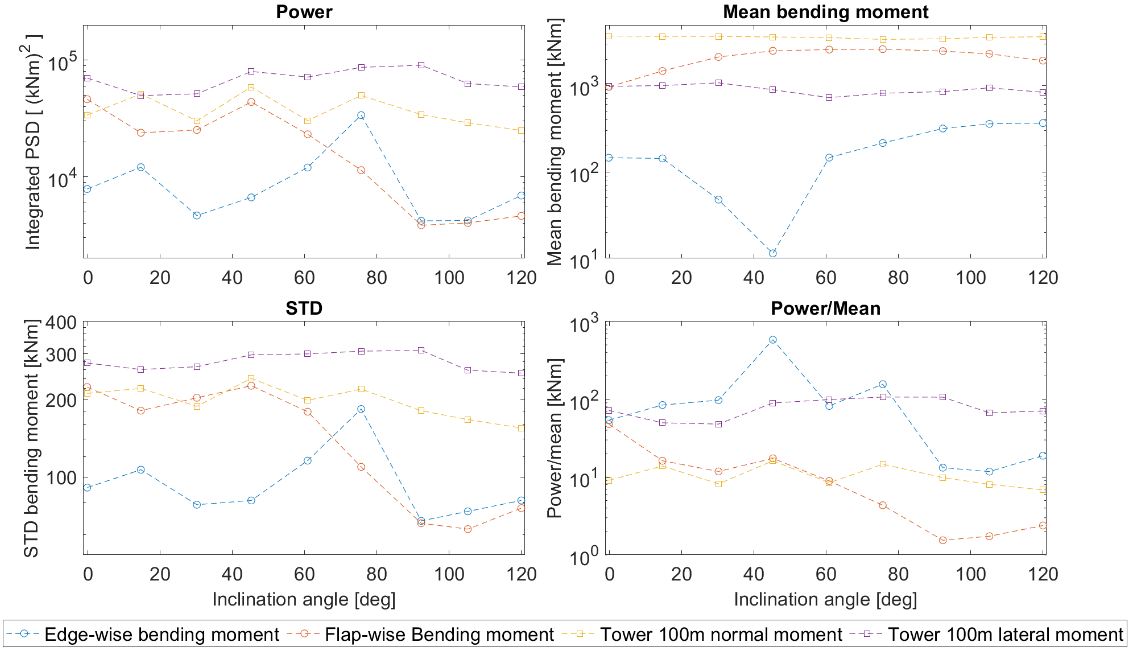

Figure 4.29: Power from integrated PSD, mean bending moment, standard deviation, and power divided by the RMS (top-left/top-right)

Chapter 5

Simulations

This section aims to show various results obtained by attempting to simulate the same conditions as were tested in the experiment. Some similarities and differences between simulation and experiment will be discussed as several different dynamic stall models will be tried out. As discussed in section 3.3, all simulations are performed using the aeroelastic solver PHATAS[32].

The goal of simulating the turbine is to see if the aeroelastic tool can be used to further expand on the knowledge obtained from the experiments. For example, combining one blade at 180 degrees pitch and a yaw angle resulted in unstable vibrations. Does this also occur for different pitch angles like 135, 45, or 0 degrees? If this is not the case, It might be possible to identify a more optimal pitching strategy which prevents problematic SVIV and reduces the oscillations when in stall. A good working simulation can also give further insight into the modes experienced by the turbine in SVIV, which may help with future structural design.

Naturally, before the aeroelastic tool can be used for such purposes, it first needs to be validated to correctly simulate SVIV. The experimental dataset can be used for this purpose.

For the simulation, it is important that it can identify the correct peaks for the natural frequencies and the right correlation between the amplitude of these peaks and the pitch and yaw angles. Hence simulating a yaw traverse and a pitch traverse is crucial for the comparison. The behavior of the simulation using different inflow conditions or dynamic stall models are also of interest, to find what settings best represent reality. Lastly, The conditions where unstable SVIV occurred in the experiment should be simulated to find if the observed unstable behavior matches the simulation. Based on these cases, it should be possible to conclude if the simulation can be used to extend to different conditions and what limitations it might have. Table 5.1 gives an overview of the experiments treated in this report.

#	Goal	Based on	Dynamic stall	Inflow type	Pitch	Yaw misaligned	Rotor Azimuth	Wind (std) [m/s]
5.1.1	Compare inflow conditions	Test 2	None	Steady	Traverse	0°	240°	14.3 (1.6)
5.1.2	Compare inflow conditions	Test 2	None	SWIFT	Traverse	0°	240°	14.3 (1.6)
5.1.3	Compare inflow conditions	Test 2	None	Lidar data	Traverse	0°	240°	14.3 (1.6)
5.2.1	Compare dyn. stall models	Test 2	Snel, 1st order	Lidar data	Traverse	0°	240°	14.3 (1.6)
5.2.2	Compare dyn. stall models	Test 2	Snel, 2nd order	Lidar data	Traverse	0°	240°	14.3 (1.6)
5.2.3	Compare dyn. stall models	Test 2	Beddoes–Leishman	Lidar data	Traverse	0°	240°	14.3 (1.6)
5.3.1	Natural frequencies	Test 2	Beddoes–Leishman	Lidar data	Traverse	0°	240°	14.3 (1.6)
5.3.2	Natural frequencies	Test 2	Beddoes–Leishman	Lidar data	85°/85°/85°	0°	330°	14.3 (1.6)
5.3.3	Shaft frequency	None	None	Steady	85°/85°/85°	0°	240°	2.0 (0.0)
5.4.1	Pitch vs yaw traverse	Test 2	Beddoes–Leishman	Lidar data	Traverse	0°	240°	14.3 (1.6)
5.4.2	Pitch vs yaw traverse	Test 5	Beddoes–Leishman	Lidar data	85°/85°/85°	Traverse	240°	14.3 (1.6)
5.5.1	Inspect AWSM results	Test 2	Snel, 1st order	Lidar data	Traverse	0°	240°	14.3 (1.6)
5.6.1	Recreate SIV instability	Test 9	Beddoes–Leishman	Lidar data	85°/85°/180°	Traverse	240°	16.6 (1.8)
5.6.2	Recreate SIV instability	Test 8	Beddoes–Leishman	Lidar data	85°/180°/85°	Traverse	120°	19.5 (2.8)
5.6.3	Extend yaw traverse	Test 8	Beddoes–Leishman	SWIFT	85°/180°/85°	Traverse	120°	19.5 (2.8)
5.6.4	Recreate SIV instability	Test 9	Snel, 1st order	Lidar data	85°/85°/180°	Traverse	240°	16.6 (1.8)
5.6.5	Recreate SIV instability	Test 9	Snel, 2nd order	Lidar data	85°/85°/180°	Traverse	240°	16.6 (1.8)
5.6.6	Recreate SIV instability	Test 8	Snel, 1st order	Lidar data	85°/180°/85°	Traverse	120°	19.5 (2.8)
5.6.7	Recreate SIV instability	Test 8	Snel, 2nd order	Lidar data	85°/180°/85°	Traverse	120°	19.5 (2.8)

Table 5.1: Table summarizing simulations performed for the various experiments

5.1 Inflow conditions

As an initial test for the simulation, various types of inflow conditions were checked. This could give insight into how the oscillations of the simulations were dependent on the state of the inflow. The following cases are compared: static inflow, turbulent inflow as generated by SWIFT, and wind speed as measured by the lidar. See Table 5.2 for an overview of the differences between the three cases.

test case	**5.1.1 Static**	**5.1.2 SWIFT**	**5.1.3 Measured**
Origin	Manually defined	Simulated	Lidar
Turbulence	No	11%	11%
Vert. shear	Power function	Stochastic sim.	Spline interpolation
Hor. shear	no	Stochastic sim.	No
Simulation time	360 seconds		
Wind ramp time	60 seconds		
Dynamic stall model	None		
Blade segments	28		
Mean wind speed	$14.3m/s$		
Mean yaw angle	0°		

Table 5.2: Constant parameters for the simulations comparing different types of inflow

Test 2 in Table 4.1 was the most extensive pitch traverse experiment performed. Because of this, it was chosen as the reference case for the comparison between different inflow models. Hence, the simulations were set up in an attempt to mimic these test conditions while using different types of inflow conditions. For the static test case, the incoming wind speed at hub height is kept constant at the average wind speed of the recreated test case. Shear was implemented based on a power curve and also remained constant during the simulation.

The turbulent inflow generated by Swift was based on the same average wind speed but with a turbulence intensity of 11%, which matches the turbulence measured during the experiment. If a different experiment were to be simulated, the average wind speed and turbulence intensity should be adjusted accordingly. This wind field is generated stochastically and creates a wind field containing both vertical shear and horizontal shear. This stochastic wind should thus be similar to the experiment in wind speed and turbulence intensity, but will not mimic the testing conditions. It will not have the same variations over time because it is stochastically generated around the mean. As such, the actual variations of windspeed over time may be quite different from the experiment and it will not capture situations like gusts. Hence, there will be some discrepancies between the simulated conditions and the experimental conditions.

An alternative to simulating the unsteady wind field with Swift is to directly input the wind field as measured during the testing campaign. This method may be able to mimic the testing conditions better than the stochastic wind which may behave very differently from the testing conditions. Using the measured wind speed does however come with some limitations. The lidar is capable of measuring the wind speed at various altitudes and can thus give an insight into the vertical shear, however, it can't measure the varying windspeed in the lateral direction. This would thus result in a wind field that varies correctly on the z-axis while remaining constant along the y-axis. lastly, while located upwind, the lidar may not measure the wind that passes directly by the rotor, as the wind direction is constantly shifting. As such, it can only show an indication of the kind of wind the turbine is experiencing.

Inflow conditions results

Figure 5.1 shows the simulated response of the edgewise bending moment of blade three with respect to the pitch angle for various simulated inflow conditions. Clearly, the static inflow does not show comparable results compared to the experiment. The order of magnitude of the force oscillations in the simulation is much smaller than in reality. The only exception is when the blade is at 80 degrees and BEM is modeling limit cycle oscillations as the outer part of the blade jumps between stalled conditions and attached conditions. Here, the absence of turbulent wind or dynamic stall conditions severely increased the oscillations around stall.

The results of the simulation when using either a generated turbulent inflow from SWIFT or the interpolated data from the LIDAR show results much closer in magnitude to what was measured in the experiment. This clearly shows the need for realistic inflow in the simulation. While unsteady inflow conditions show decent results, the measured inflow is believed to more closely mimic the experiment conditions and therefore is a better inflow. The lack of variance of the windspeed in the y-direction has likely very limited influence as the measured and varied blade is pointed straight up in the sky.

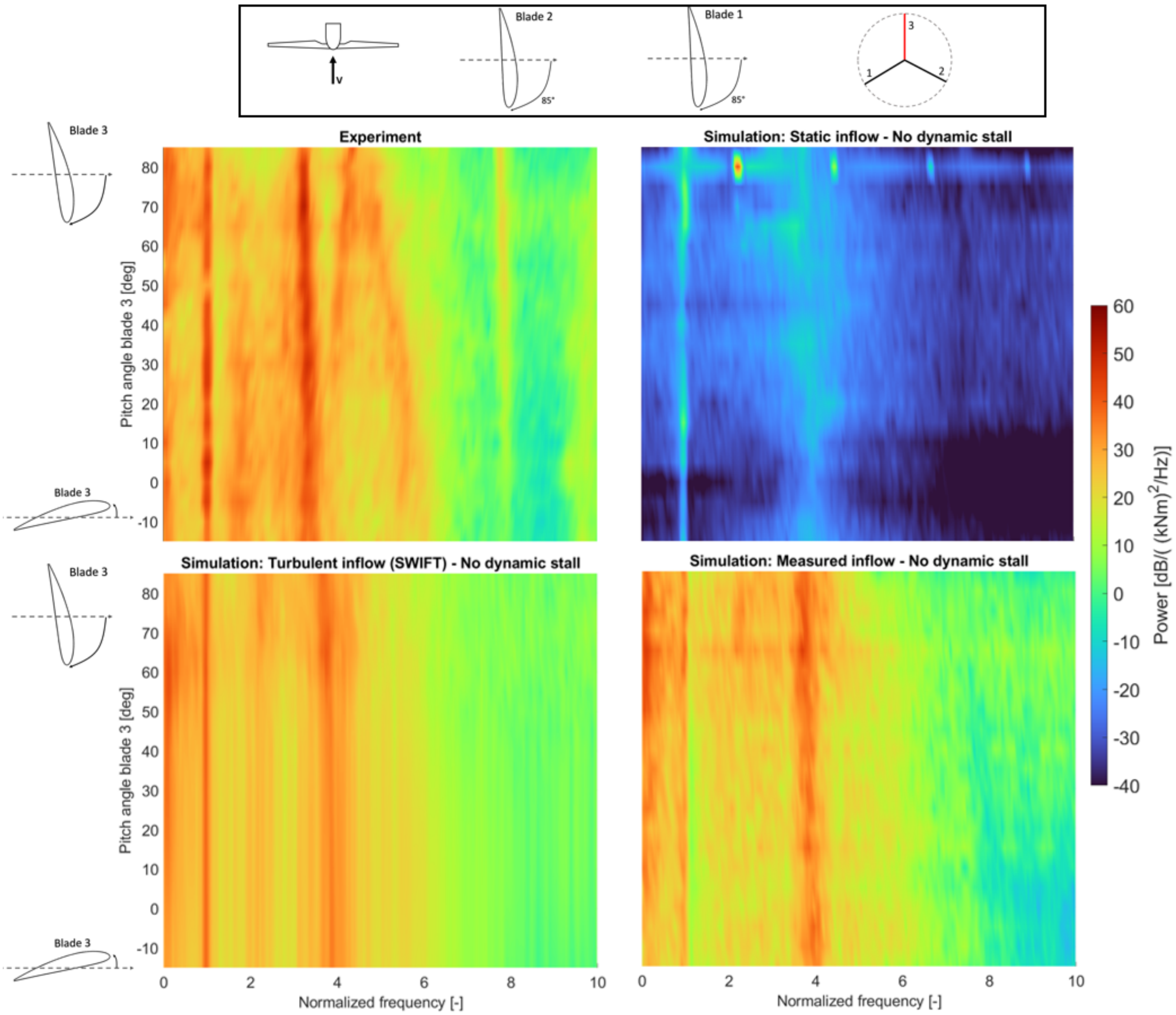

Figure 5.1: Edgewise bending moment at the root of blade 3 with the pitch angle of blade 3: experiment (top left), static inflow (top right), SWIFT turbulent inflow (bottom left), measured inflow (bottom right). all simulations without dynamic stall

5.2 Dynamic stall models

Dynamic stall models are generally considered to be of high importance when attempting to simulate the conditions of SVIV. This is because the vortices shed during stall greatly affect the perceived inflow angles. This effect is strongly coupled with the structural vibrations. Hence whenever there exists vortex shedding, a dynamic stall model should be needed. The simulations for three different dynamic stall models are described in Table 5.3

Test case	5.2.1	5.2.2	5.2.3
Dynamic stall model	Snel, 1st order	Snel, 2nd order	Beddoes-Leishman
Simulation time	360 seconds		
Wind ramp time	60 seconds		
Blade segments	28		
Mean wind speed	$14.3 m/s$		
Turbulence	11%		
Inflow origin	Lidar		
Vert. shear	Spline interpolated		
Hor. sher	none		
Mean yaw angle	0°		
Pitch angle blade 1	85°		
Pitch angle blade 2	85°		
Pitch angle blade 3	traverse°		
Azimuth angle blade 3	0°		

Table 5.3: Input conditions for the simulations comparing different Dynamic stall models

Figure 5.2 shows the PDF of the same edgewise bending moment with respect to the pitch angle of blade 3 as in Figure 5.1, but now compared to different dynamic stall models. These simulations have been performed using the measured inflow conditions from the experiment. The different dynamic stall models result in oscillation peaks with the same frequencies, but significantly different magnitudes. The second-order dynamic stall model based on Snel shows the highest magnitudes whereas the Beddoes Leishman model shows the smallest amplitudes.

Regardless of the dynamic stall method chosen, there appear the be large differences in the frequencies of the peaks when compared to the experimental results. Especially the shifting frequencies during the pitch traverse do not appear to show up clearly in the simulation. This will be further discussed in section 5.3.

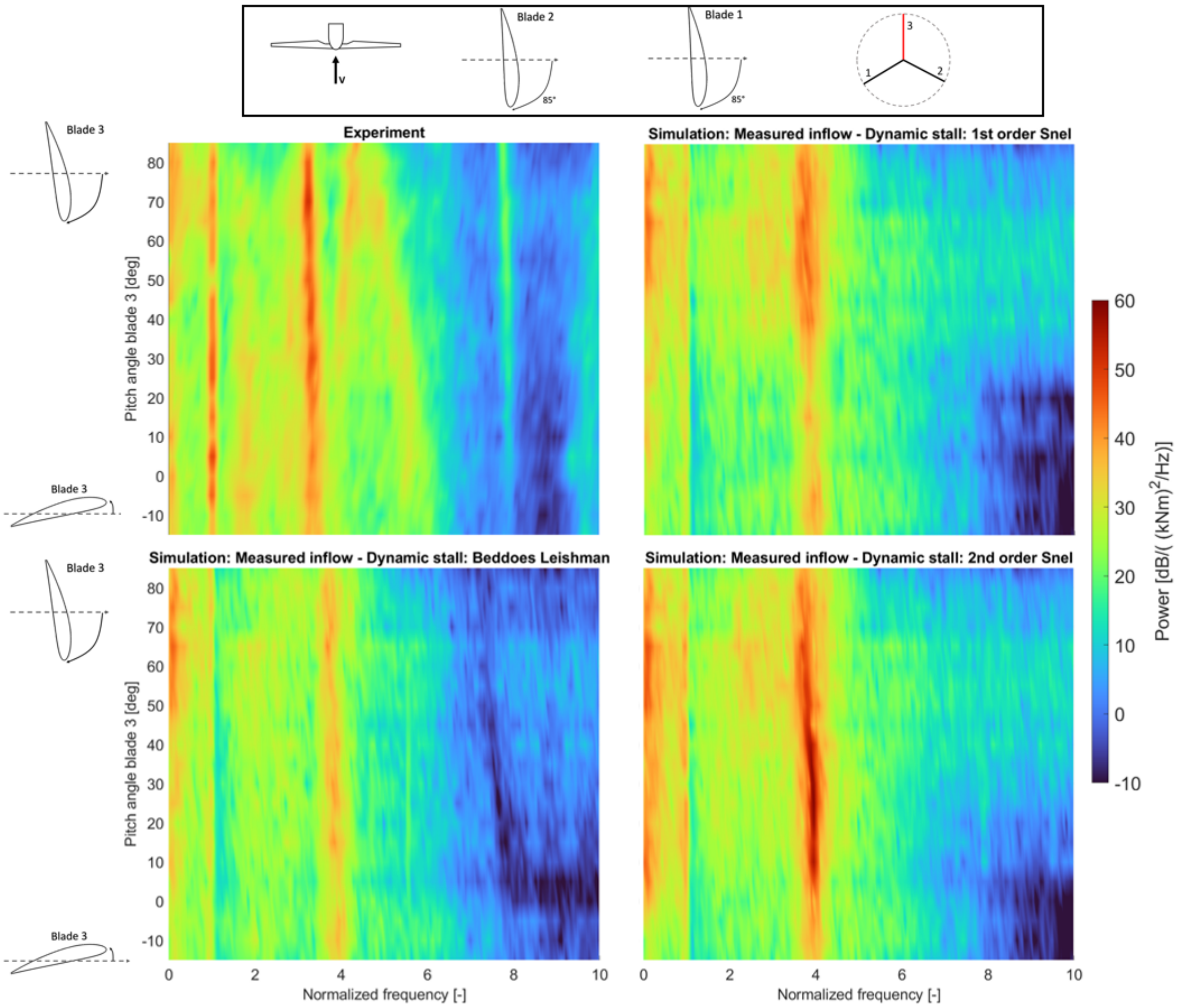

Figure 5.2: Edgewise bending moment at the root of blade 3 with the pitch angle of blade 3: experiment (top left), 1st order Snel (top right), 2nd order Snel (bottom right), Beddoes Leishman (bottom left). all simulations with measured inflow conditions

5.3 Simulated natural frequencies

Following the comparison between various models, it is important to know how well the natural frequencies of the model match what was observed during the actual experiments.Table 5.4 shows an overview of what are believed to be the natural frequencies as observed from the simulation. The frequencies from the model file originate from the individual components of the wind turbine model in use and do not take into account any interaction between the blades, nacelle, and tower. Since this is not fully realistic, the second column attempts to identify these key frequencies from the aero-elastic simulation. As mentioned in section 3.3, the aero-elastic solver was unable to run while simulating the drive-train shaft to be elastic. Thus the shaft torsion mode is expected to not be visible in the simulation data. Table 5.5 gives an overview of the simulations used to identify the natural frequencies. However, these modes should be identifiable in all other simulations as well.

Mode	**Model file [-]**	**Aero-elastic simulation [-]**	**Experiment [-]**
1st tower FA	0.98	0.98	1,0
1st tower SS	0.98	0.98	1.0
1st Shaft torsion	-	1.7*	1.8
1st flapwise	2.2	2.0	2.2
asymmetric edgewise in yaw	-	3.2	2.9
asymmetric edgewise in tilt	-	3.8	3.3
symmetric edgewise	4.1	4.1	4.4
2nd flapwise	6.08	5.6	6.2
2nd tower FA	6.08	7.6	7.8
2nd tower SS	4.68	7,8	7.8

Table 5.4: Normalized natural frequencies identified from the simulation and compared to the experiment when all blades are in vane position of 85 degrees pitch. *Shaft torsion determined separately but not present in most simulations due to resulting instabilities

Test case	5.3.1	5.3.2
Azimuth angle blade 3	0°	90°
Simulation time	360 seconds	
Wind ramp time	60 seconds	
Blade segments	28	
Mean wind speed	14.3m/s	
Turbulence	11%	
Inflow origin	Lidar	
Vert. shear	Spline interpolated	
Hor. sher	none	
Mean yaw angle	0°	
Pitch angle blade 1	85°	
Pitch angle blade 2	85°	
Pitch angle blade 3	-15° till 85°	
Dynamic stall	Beddoes-Leishman	

Table 5.5: Input conditions for the simulations to identify the excited modes

The PSD plots shown in Figure 5.3 were used to determine the natural frequencies of the model in the aero-elastic simulations. Not all natural frequencies may however be successfully identified due to being damped out or because other vibration modes have a rather broad peak in the PSD, for example, the mode around the normalized natural frequency of 2. Also, to find the edge-wise asymmetric mode in yaw, a simulation with the measured blade at 90-degree azimuth angle was used as in Figure 5.5. While Table 5.4 only shows the modes for the parked condition with all blades at 85 degrees pitch, a pitch traverse is useful to help identify these modes.

The first tower mode in the simulation appears to be very close to the model file and the experiment, but all frequencies below this peak show a rather high amplitude as well. This is believed to be likely due to the unsteady inflow from the wind rather than the structural dynamic of the turbine. The peak in the flapwise direction around the frequency of 2 is rather broad.

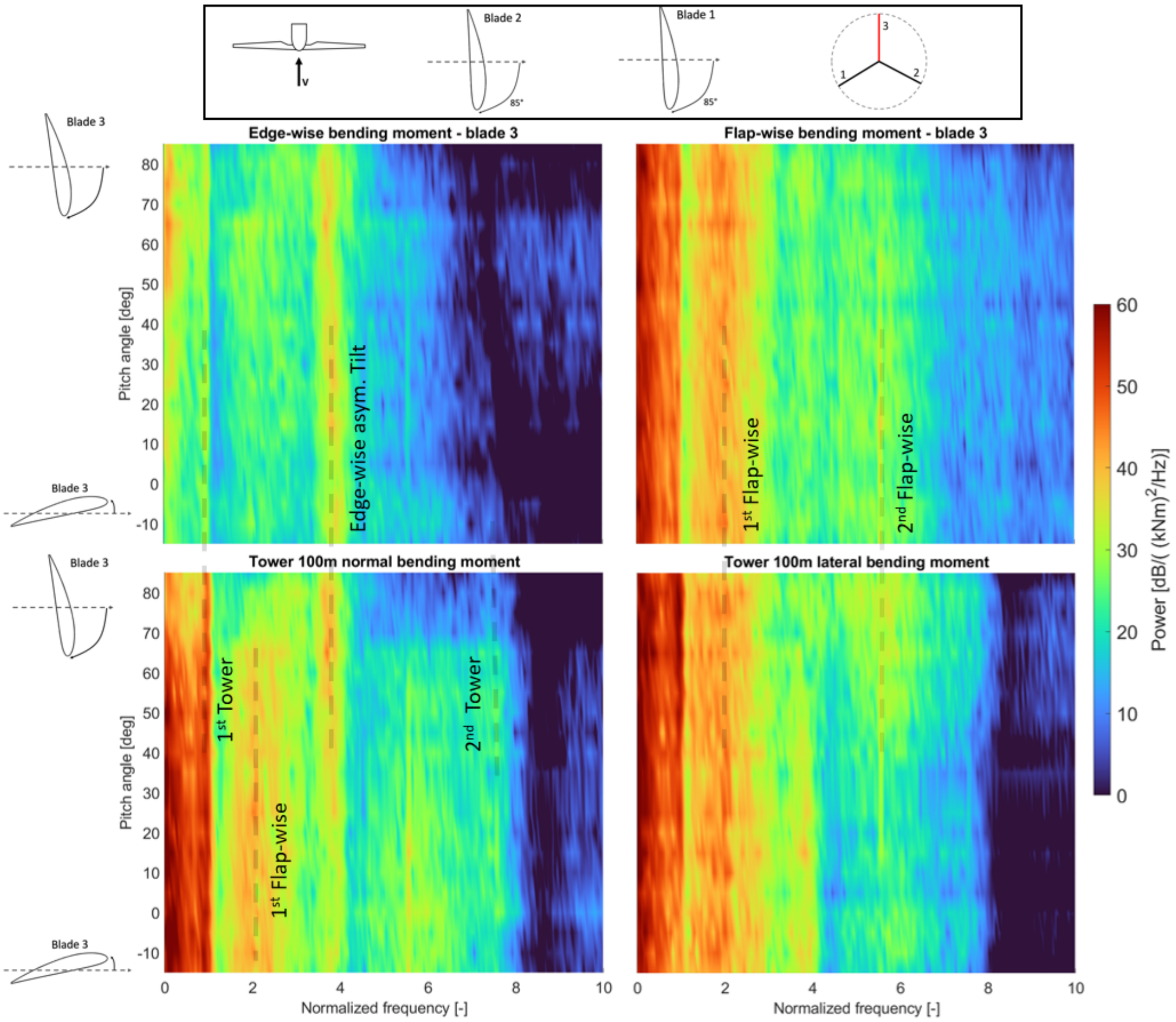

Figure 5.3: PSD of the simulation results using Bedoes Leishman dynamic stall and inflow conditions as measured by the lidar

The higher tower modes do not appear very clearly in Figure 5.3. The tower bending mode 8 meters from the root of the tower is plotted in Figure 5.4 to help better identify the tower modes. While the model file showed natural frequencies of 6.08 in the normal direction and 4.68 in the lateral direction, there were no large peaks present at these frequencies. Instead, the peaks which are believed to be tower modes are located at 0.98 and 7.6 in the normal direction, and 0.98 and 7.8 in the lateral direction. These frequencies also match the experimental results rather closely and show the need to simulate the turbine instead of relying on the model file.

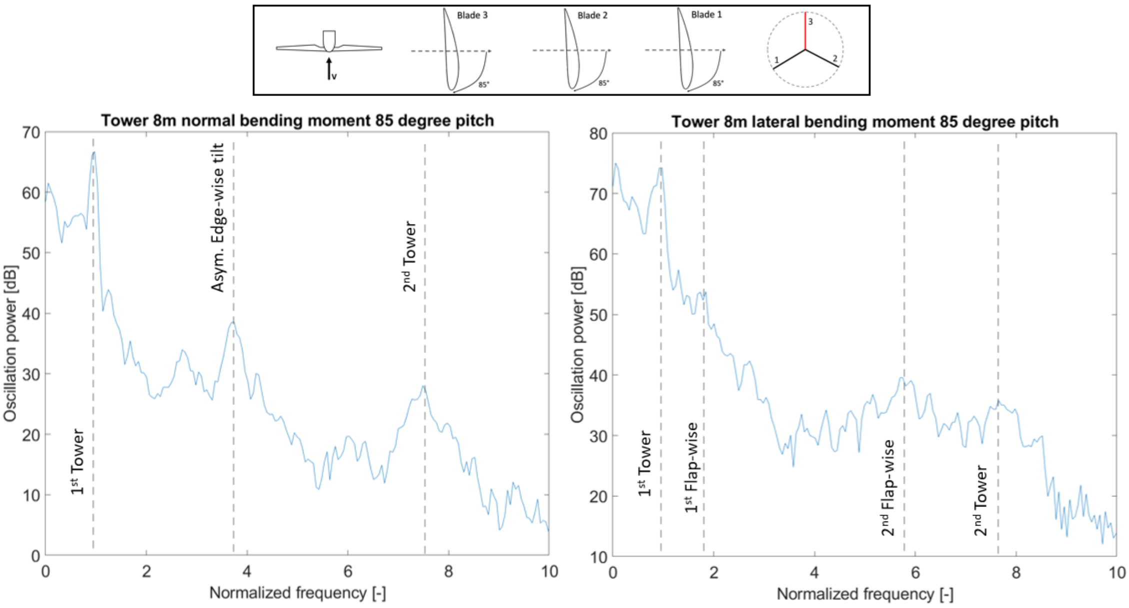

Figure 5.4: PSD of the bending moment near the tower root (8m high) for all blades at 85 degrees pitch. Simulation results use the Bedoes-Leishman dynamic stall model and inflow conditions as measured by the lidar

The asymmetric edge-wise modes exist because of the interaction of multiple blades and will therefore only exist after the simulation and not in the model file. The asymmetric modes can be identified by being present in the blade for either aligned with the tower (0-degree azimuth) or horizontal (90-degree azimuth). for angles in between, both asymmetric modes should be present and the symmetric mode should always be present. Figure 5.5 shows the edgewise response of the blade when performing a pitch traverse at either 0 or 90 degrees azimuth at 85 degrees pitch. The peak at the frequency of 4.1 is likely the symmetric edgewise mode, as it is present in both 0 and 90 degrees azimuth.

At a normalized frequency of 2.7 a peak appears to be visible in all signals. To identify the source of this peak, simulation 5.3.1 was repeated several times with different degrees of freedom turned off. When either the edgewise or the flapwise bending was removed from the simulation, this frequency disappeared in the PSD. Hence it was determined that this mode is likely a coupled mode between edge and flapwise direction. This mode was not noticeable in the experiment data. This is possibly due to some inaccurate modeling of coupling between the blades or because this frequency experiences more damping in the actual turbine.

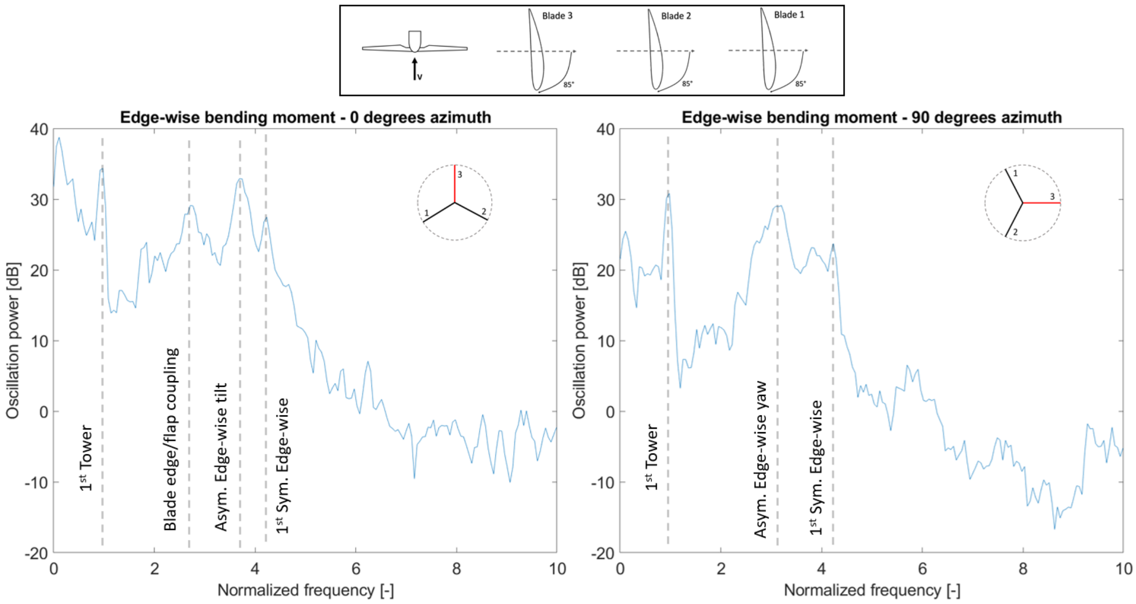

Figure 5.5: PSD of the edge-wise bending moment at 0 vs 90 degrees azimuth. Simulation results use the Bedoes-Leishman dynamic stall model and inflow conditions as measured by the lidar

Shaft torsion

As discussed previously, including a flexible shaft in the simulation resulted in an unstable simulation. This subsection aims to discuss this in a little more detail.

When simulating a case like 5.3.1 in Table 5.5, the simulation tended to crash within 1 second. The cause of this crash appeared to be instability which caused all forces, deformations, and accelerations to increase to unrealistic values before returning 'NaN'. However, while the simulations with conditions similar to the experiment did not result in usable data, a simpler simulation as defined in Table 5.6 did work. The key to getting the simple simulation to work was setting the timestep to 0.02 seconds which caused the instability to fall outside of the Nyquist limit. This was however not a catch-all solution, as most simulations would not successfully run with this time-step.

This simulation could thus help identify a shaft torsional frequency of the structural model. Figure 5.6 shows the power spectral density of the shaft torsion where the 1st tower mode and the 1st shaft frequency are identified. The 1st shaft mode was determined to be at a normalized frequency of 1.7. Due to the instabilities caused by the shaft modeling, the shaft torsion could not be included in the other simulations.

Test case	5.3.3
Simulation time	360 seconds
Wind ramp time	60 seconds
Blade segments	28
Mean wind speed	$2m/s$
Turbulence	0%
Inflow origin	manually defined
Vert. shear	none
Hor. sher	none
Mean yaw angle	0°
Pitch angle blade 1	85°
Pitch angle blade 2	85°
Pitch angle blade 3	85°
Dynamic stall	none
Shaft torsion	enabled

Table 5.6: Input conditions for simplified simulation to check shaft torsion

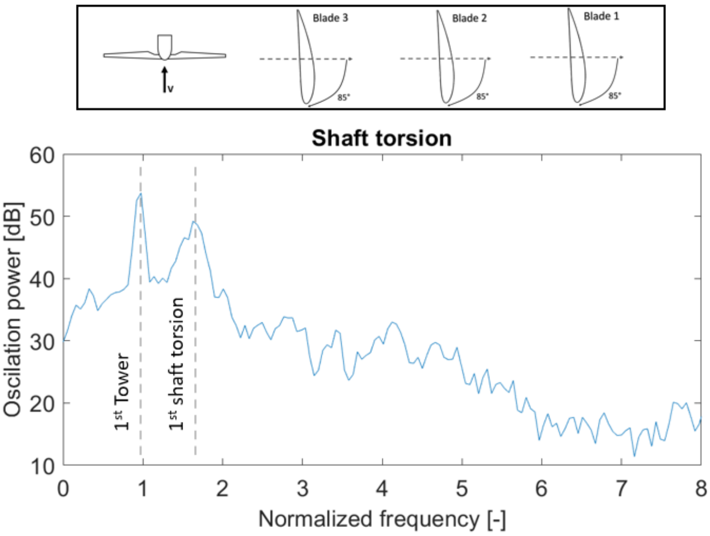

Figure 5.6: PSD of the shaft torsion, for a simplified simulation with steady 2m/s inflow and all blades at 85 degrees pitch

5.4 Pitch vs. yaw traverse

In section 4.7, the difference between a pitch traverse and a yaw traverse was compared for a situation where the local angle of attack was the same. A key difference identified was the shifting natural frequencies during the pitch traverse, indicating a strong coupling effect between the blades. This section aims to perform the same comparison between a pitch or yaw traverse for the same local angle of attack for blade 3 at a local azimuth angle of 0 degrees. This simulation uses the Beddoes-Leishman dynamic stall model and uses the inflow conditions as measured by the lidar from experiment 2 as presented in Table 4.1 ($V_{mean} = 14.3$, $Ti = 11\%$).

Test case	5.4.1 pitch traverse	5.4.2 yaw traverse
Yaw misalignment	0	-105° till 0°
Pitch angle blade 1	85°	85°
Pitch angle blade 2	85°	85°
Pitch angle blade 3	-15° till 85°	85°
Measured blade	Blade 3	
Measured blade azimuth angle	0°	
Measured blade angle of attack	5° till 105°	
Simulation time	360 seconds	
Wind ramp time	10 seconds	
Blade segments	28	
Mean wind speed	$14.3 m/s$	
Turbulence	11%	
Inflow origin	Lidar, experiment 2	
Vert. shear	Spline interpolated	
Hor. sher	none	
Dynamic stall model	Beddoes-Leishman	

Table 5.7: Input conditions for the simulations compare between yaw and pitch traverse in the simulations

Just like in the experiment, the natural frequencies remain at a fixed frequency for the yaw traverse. However, in the pitch traverse the oscillations peaks ought to shift in frequency as was the case for the experiment shown in Figure 4.23. This shifting is however not visible in Figure 5.7. While a small shift does occur as was pointed out in section 5.3, it pales in comparison compared to the actual experiment. As such it can be concluded that modeling of the coupling between the blades as a single blade gets pitched is not sufficiently well implemented. Improving this structural modeling is outside of the scope of this project.

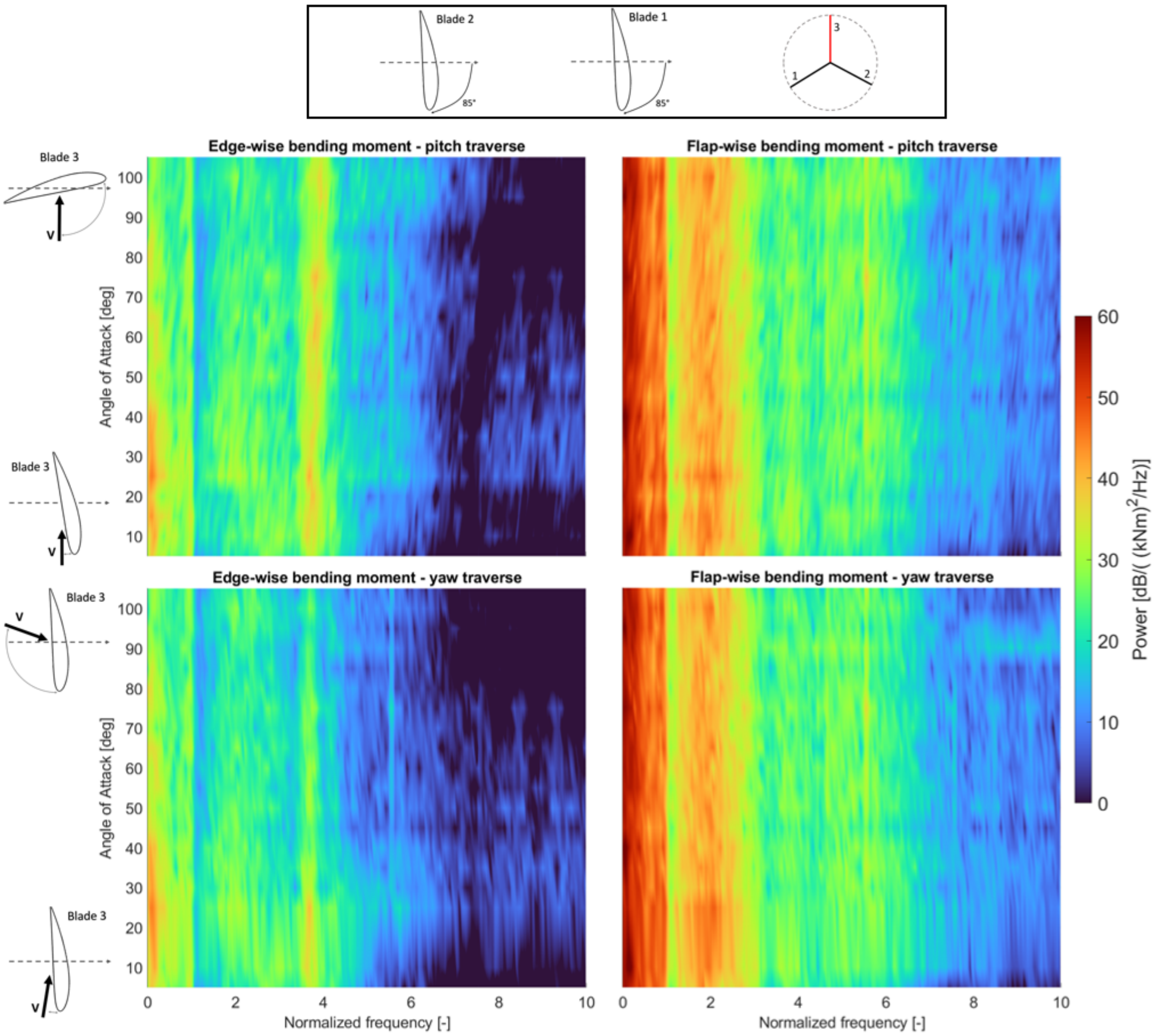

Figure 5.7: Comparing the PSD of the Force oscillations in the blade resulting from the same local angle of attack conditions on the top blade (0 degrees azimuth) between a yaw and pitch traverse

5.5 AWSM results

The AWSM model is based on lifting-line free vortex wake modeling and is thus inherently different from BEM. However, because the lifting line C_L and C_D data originates from polars as defined by the user, a dynamic stall model is still required. Figure 5.8 shows the resulting power spectral density from simulating a pitch traverse using AWSM as the aerodynamic solver versus the experiment. This simulation used the first-order Snel dynamic stall model and was limited to 5 free vortex wake points to speed up calculation. The overview of the simulation settings is given in Table 5.8.

Test case	5.5.1 AWSM pitch traverse
Simulation model	Lifting-line free wake vortex shedding
Simulation time	360 seconds
Wind ramp time	10 seconds
Blade segments	14
Wake nodes	5
Mean wind speed	$14.3 m/s$
Turbulence	11%
Dynamic stall	1st order Snel
Inflow origin	Lidar
Vert. shear	Spline interpolated
Hor. sher	None
yaw angle	0°
Pitch angle blade 1	85°
Pitch angle blade 2	85°
Pitch angle blade 3	traverse°
Azimuth angle blade 3	0°

Table 5.8: Input conditions for the simulation using AWSM

Free Vortex Wake modeling is generally considered a higher fidelity engineering model than BEM, at the cost of being more computationally expensive. The computational effort required for a simulation with a large wake was however beyond the resources available to this project. Instead, a rather short wake of 5 wake points is simulated. The wind turbine is parked and thus does not result in the higher wind speed and the spiraling vortices from an operating turbine. Hence, A short wake was assumed to be reasonably accurate for this comparison.

Figure 5.8 shows the same discrepancies as were seen in the BEM simulations. The first symmetric mode in the edgewise direction and the second symmetric mode in the flapwise direction do not shift in frequency nearly as much as what is visible in the experiment. Also, the tower mode at a frequency of 7.9 was absent. These changes were seen consistently in all simulations regardless of the aerodynamic model and are thus most likely due to the structural model.

In the experiment, the magnitude of the force oscillations from the blade modes was reduced when the blade pitch was reduced to 0 degrees signifying an increased aerodynamic damping. The AWSM simulation showed a much more significant decrease in amplitude in the edgewise direction and not enough of a reduction in the amplitude in the flapwise direction around the frequency of 2.

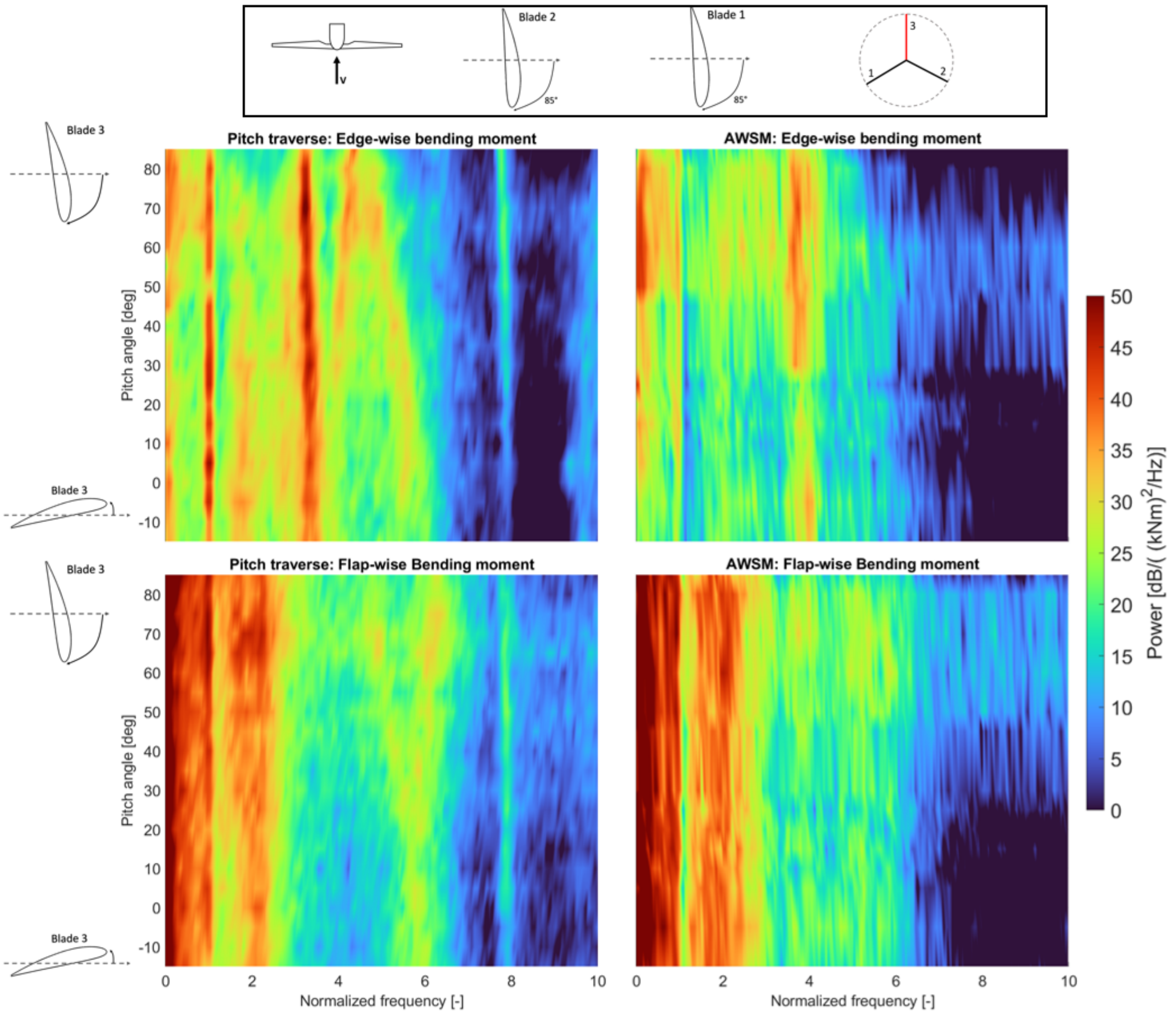

Figure 5.8: Simulation with AWSM vs. experiment for a pitch traverse at $V = 14.3m/s$, $Ti = 11\%$, and the mean yaw angle is 0°

5.6 Extreme SIV

During the experiment, problematic SIV was identified to occur for tests 8 and 9 from Table 4.1. In these tests, one blade was pitched at 180 degrees pitch at 0 degrees azimuth while both other blades were at 85 degrees. Around the yaw angle of 113 degrees, the wind turbine was visibly moving and the force oscillations greatly increased in amplitude. While the simulations showed some clear limitations in the previous tests, it may still be interesting to see if the situation where severe SIV should be present would be possible to simulate. Table 5.9 gives an overview of the input and conditions of the simulations performed.

Test case	**5.6.1**	**5.6.2**	**5.6.3**	**5.6.4**	**5.6.5**	**5.6.6**	**5.6.7**
Dynamic stall model	Beddoes-Leishman	Beddoes-Leishman	Beddoes-Leishman	1st order Snel	2nd order Snel	1st order Snel	2nd order Snel
Based on experiment	9	8	8-extended	9		8	
Simulation time	360 seconds	360 seconds	360 seconds	360 seconds		360 seconds	
Wind ramp time	10 seconds	10 seconds	10 seconds	10 seconds		10 seconds	
Blade segments	28	28	28	28		28	
Mean wind speed	16.6m/s	19.5m/s	19.5m/s	16.6m/s		19.5m/s	
Turbulence	11%	14%	14%	11%		14%	
Inflow origin	Lidar	Lidar	SWIFT	Lidar		Lidar	
Vert. shear	Spline interpolated	Spline interpolated	Generated	Spline interpolated		Spline interpolated	
Hor. sher	none	none	Generated	none		none	
Yaw traverse	93° till 113°	94° till 117°	80° till 130°	93° till 113°		94° till 117°	
Measured blade	Blade 3	Blade 2	Blade 2	Blade 3		Blade 2	
Blade azimuth angle	0°	0°	0°	0°		0°	
Pitch angle blade 1	85°	85°	85°	85°		85°	
Pitch angle blade 2	85°	180°	180°	85°		180°	
Pitch angle blade 3	180°	85°	85°	180°		85°	

Table 5.9: Input conditions for the simulations to mimic the severe SIV case

Figure 5.9 shows the results of the simulation compared to experiment 9. At the top of the figure, the lateral (side-side) bending moment is compared in a surface plot. Here it is already clear that the simulation does not have the same magnitude of force oscillations present around the yaw angles where the experiment experienced much higher amplitude oscillations. At the bottom of Figure 5.9 the integrated power is plotted for the tower and blade, and the same conclusion can be made. At the yaw angles where the sensors measure more power in the oscillations, no such phenomenon was found during the simulation.

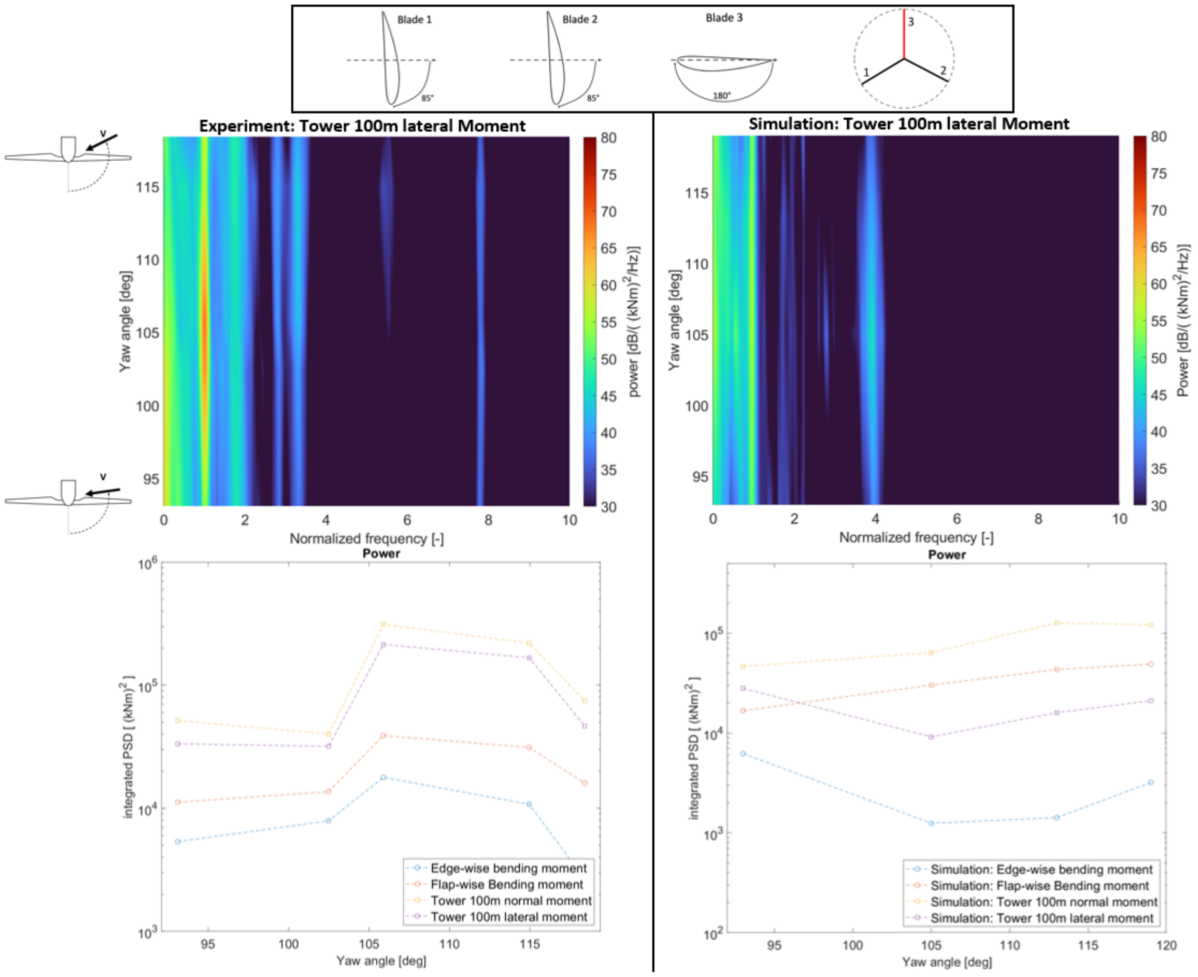

Figure 5.9: SIV Simulation result vs. experiment: Mimic yaw traverse of experiment 9, with blade 3 at 0° azimuth, pitch of blade 1 and 2 at 85° and pitch of blade 3 at 180°, with $V = 16.6m/s$ and $Ti = 11\%$

Figure 5.10 compares the simulation results aimed to mimic the extreme oscillations observed in experiment 8. The wind data is however limited due to the experiment being cut short when the force oscillations became too severe. Because of this, the yaw angle of the simulation goes to 110° instead of 113°. Similarly to what was observed in the simulation of experiment 9, this simulation does not show any large growth in the power of the oscillations at the problematic yaw angles.

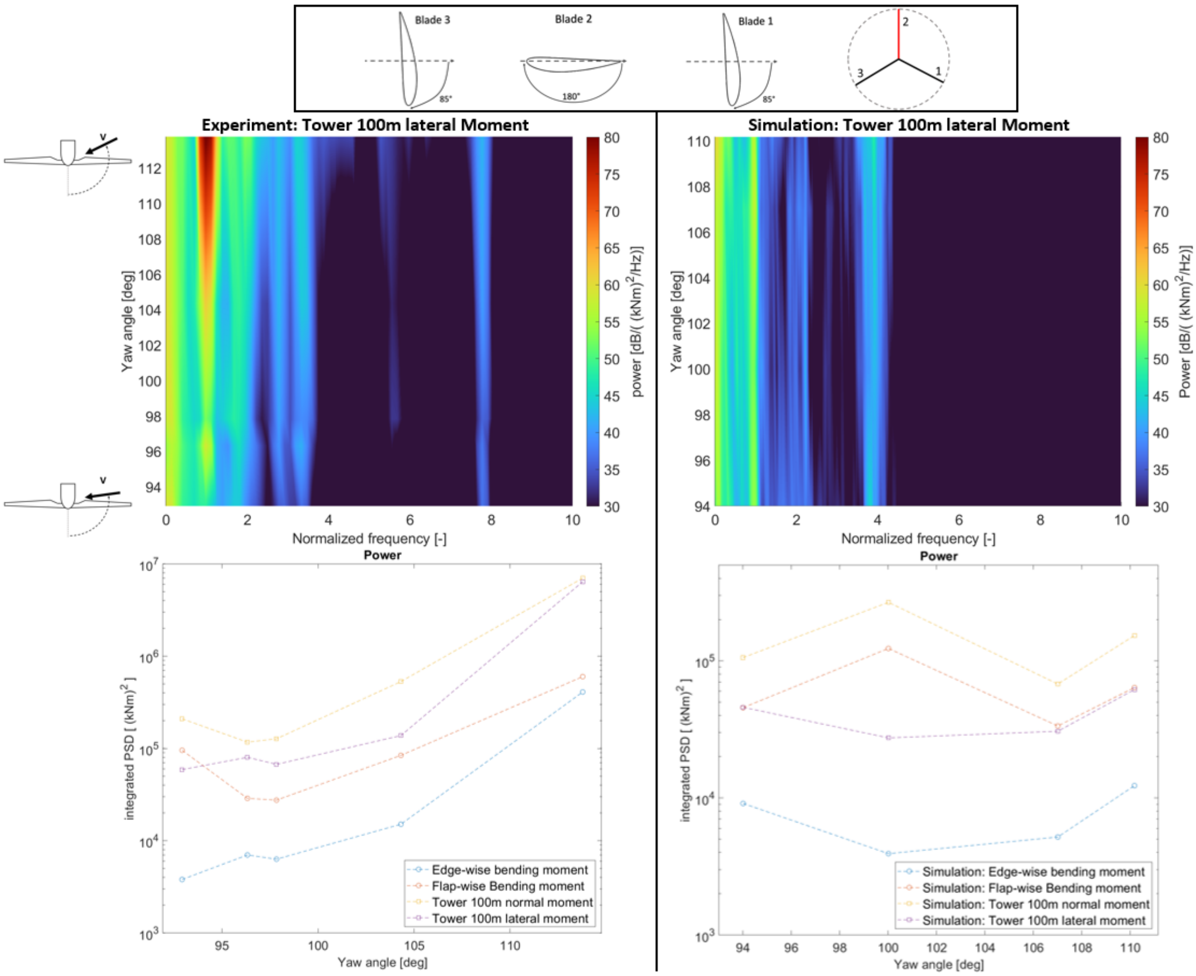

Figure 5.10: SIV Simulation result vs. experiment: Mimic yaw traverse of experiment 8, with blade 2 at 0° azimuth, pitch of blade 1 and 3 at 85° and pitch of blade 2 at 180°, with $V = 19.5m/s$ and $Ti = 14\%$

Because the wind data from the lidar only correlates to the short yaw traverse from the experiments, it may be interesting to generate further wind and simulate a larger amount of yaw angles. The integrated power of this experiment is plotted in Figure 5.11 and does not show any significant peaks in the force oscillation power for any yaw angle. Hence, the simulation model was unable to identify this instability.

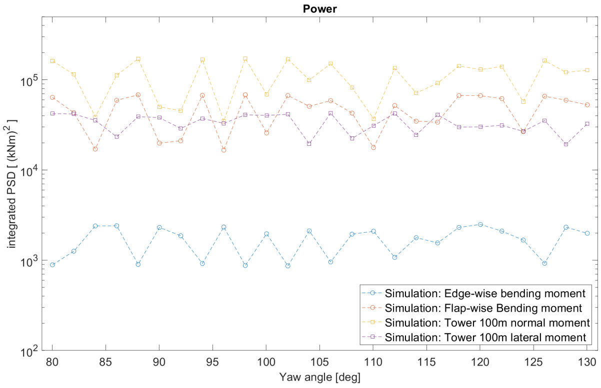

Figure 5.11: SIV Simulation result integrated power: Extending experiment 8 by generating wind using FAST for yaw angles 80° till 130°, in steps of 2°, with blade 2 at 0° azimuth and 180° pitch, and blades 1 and 3 at 85° pitch, for $V = 19.5m/s$ and $Ti = 14\%$

Using either the first or second-order Snel dynamic stall model did not result in a large increase in oscillations. Figure 5.12 shows the power obtained from simulating with both Snel models, and shows no large increase in power for any yaw angle. The oscillation power between the flapwise and the tower normal oscillations appear to have a positive correlation. As they both either increase or decrease when varying the yaw angle. similarly, the blade edgewise and tower normal bending moment have their oscillation power correlating as they behave in a very similar way. This can be explained as the measured blade is pitched at 180 degrees with a local blade azimuth angle of 0 degrees. Thus, the edgewise direction of the blade is aimed in the same direction as the tower's lateral moment, and the flapwise direction is parallel with the tower's normal direction.

However, unlike the excited state in the SIV experiment, the normal and lateral bending moments do not appear to have much correlation. During SIV of the experiment, all sensors measured increased oscillation power at the same time. Meanwhile, the simulation sometimes shows the tower's normal moment oscillation power increasing as the lateral direction decreases. This behavior may actually be quite natural and simply indicates that no unstable situation was simulated which would result in a large increase of power in the system for all directions.

To explain the lack of an unstable situation in the simulation, several causes may be of influence. The very large yaw angle for a parked turbine might not be well suited for BEM and/or its yaw modeling. Two blades are experiencing quite a large inclination angle, resulting in a likely non-negligible amount of radial flow. This falls outside of the assumptions of BEM, and since it was observed that the blade frequencies are coupled, these two blades shouldn't be ignored. There are also differences in the blade modes between the simulation and experiment which may impact the presence of the instability. Lastly, the dynamic stall model will likely not respond in a fully accurate way for the blades in deep stall.

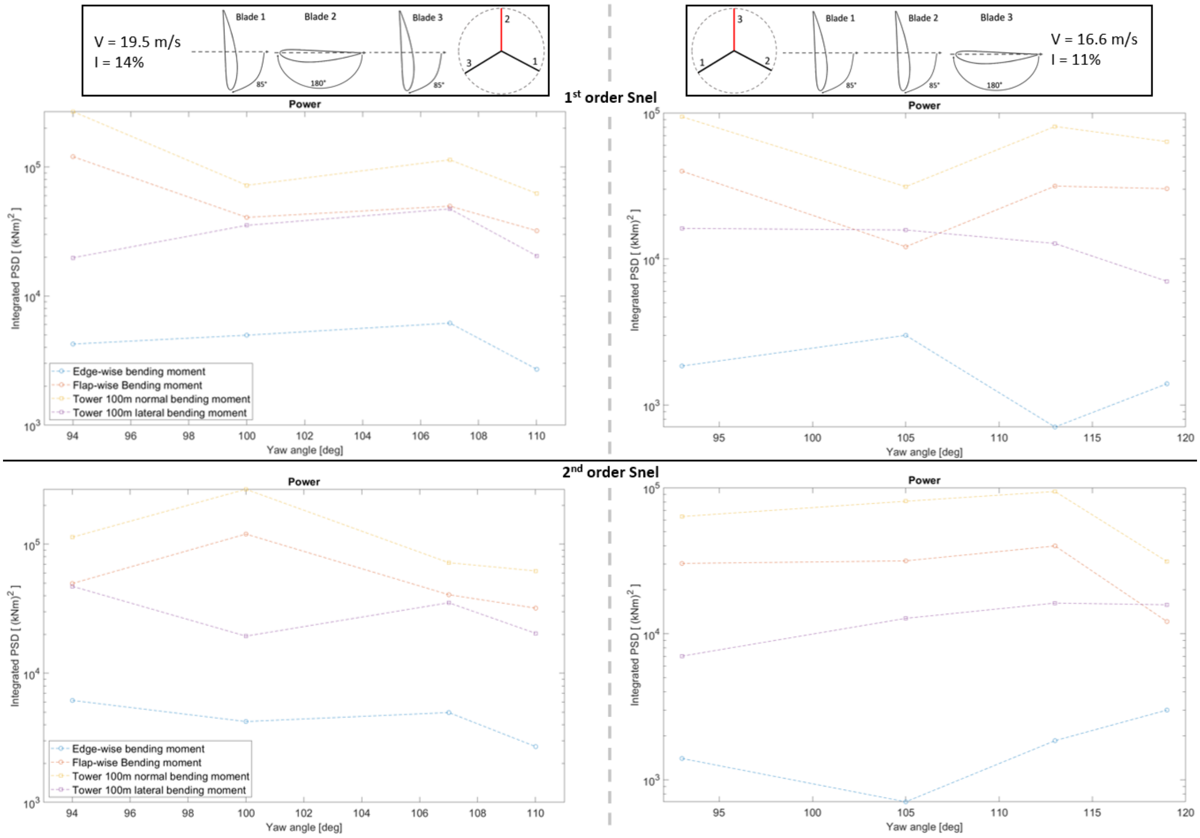

Figure 5.12: SIV Simulation result integrated power: Snel 1^{st} order and 2^{nd} order, for $V = 19.5 m/s$, $Ti = 14\%$ and $V = 16.6 m/s$, $Ti = 11\%$

Chapter 6

Conclusion and recommendations

This chapter will discuss some conclusions obtained from the experiment, its analysis, and the following simulations. These results were not without its limitations, for which some future recommendations are given

6.1 Conclusions

SVIV is a phenomenon where wind turbines suffer from greatly increased vibrations due to an aero-elastic interaction between the structure and aerodynamic forces while the blade is in deep stall. This research aimed to identify the conditions that result in SVIV for a large parked wind turbine, using experimental data from a 3.8 MW wind turbine supplemented by some simulations using PHATAS.

From analyzing the experimental data various conditions were identified where the measured forces were oscillating with an increased magnitude. When only yawing the turbine while all blades are in a feather position some specific angles like 100 and 200 degrees yaw showed an increase in the magnitude of the oscillations. The angles where the flow came from behind the wind turbine (>90 deg.) also showed slightly more oscillations than when the wind came from the front as should be the default.

Pitching the top blade away from the feather position increased damping in the edgewise and normal directions. However, when combining the top blade pitched at 180 degrees with a yaw misalignment, an unstable situation occurred for yaw angles near 110 degrees. These conditions caused all present oscillations to be amplified and continually grow over time, hence this was clearly a problematic situation of SIV. How much the amplitude will grow was strongly correlated with the wind speed, as when the test was repeated with a lower windspeed, the oscillations did not become severe enough to halt the experiment early. While all modes were excited, the first tower modes were the most dominant. The dynamics under these test conditions thus mostly synced up with the first natural frequency of the tower.

While caution should be applied to prevent situations where SIV may be problematic, pitching the blades also caused a shift in several natural frequencies. This shift is only present when varying the pitch and is thus clearly affected by the interaction between the blade and the rest of the turbine. While taking advantage of this shift in natural frequencies may be possible, aero-elastic solvers may have some difficulty predicting these more complex interactions.

Throughout the experiments, an eye was kept on the possible presence of vortex shedding, but no vortex shedding was identified. The absence of a clear vortex-shedding frequency in the data does not mean there was no vortex-shedding. Instead, it may mean that the vortex shedding was either locked in with one of the natural frequencies or that the measurement equipment simply wasn't able to detect it. To obtain a better understanding of the possible presence of vortex shedding, having more pressure sensors or strain gauges along the length of the blade may be useful. While, of course, running the risk of determining that these blades indeed do not experience structured vortex shedding which could cause VIV.

The model used in simulating the experimental conditions was identified to have a few flaws. The symmetric edgewise mode which was identified to shift greatly in frequency in the pitch traverse experiments, failed to show a similar shift in frequency during the simulation. Also, the coupled mode between edge and flap wise which was observed in the experiments did not show up in the simulation. This showed that the damping and coupling within the structural model were not properly tuned to the real turbine. This fact severely limited the results that could be obtained from the simulations, but fully resolving these issues was sadly beyond the scope of this thesis. What did become clear from the simulations was the need for accurate inflow conditions. To obtain reasonably accurate results, the inflow conditions needed to be turbulent and preferably obtained from the actual experiment. Stochastically generated wind may also result in realistic simulations, but due to its inherently random nature, will not replicate experiments as nicely.

Lastly, the simulations in this report were unable to identify the situation where extreme SIV was found in the experiment. This is likely a combination of the structural differences between the model and the turbine, the limitations of BEM, and the limitations of the dynamic stall models used. It is important to realize that BEM assumes constant stream tubes and thus can not deal well with radial flow. Situations where the blade can experience large inclination angles are therefore limited by the assumptions of BEM and the reliability of any correction model. The situation where large vibrations occurred in the experiment was around 110 degrees yaw. In this situation, the top blade did not have an inclination angle, but the other blades did. And since it was found that the coupling between the blades is significant for the blade's natural frequencies, this likely has an impact on the dynamics of the extreme excitation as well.

6.2 Future recommendations

In order to help identify vortex shedding in future experiments, it is advised to equip a blade with pressure sensors on several radial locations. During the current experiment, no vortex shedding could be identified in any of the experiments (where the pressure data was available), but it can not be definitively said that these vortices were absent. With pressure sensors installed in several locations along the blade, a better idea may form on if and where vortex shedding can be problematic.

Another limitation these experiments faced was that only one blade could be pitched at a time. This resulted in a lot of interesting data, but since it was determined that some frequencies strongly varied due to the coupling between the blades, being able to do a pitch traverse with multiple blades at the same time would give a lot of insight.

For the inclination angle traverse, the rotor azimuth angle was rotated such that the blade with most instrumentation was turned away from the wind in steps of 15 degrees, resulting in flow from root to tip. For future tests, it would be nice to see an azimuth traverse where the reverse is investigated for angles where the radial flow goes from tip to root. These angles were neglected in the current experiments but may be very interesting, also because there would be no influence from a wake from a blade in front of it. A smaller step size for the azimuth angle would also be beneficial.

Lastly, it is important to stress the importance of repeated experiments. The turbulent and uncontrollable nature of the inflow conditions which is inherent to performing experiments in the field, causes a lot of additional uncertainty. It is impossible to keep parameters constant and every time an experiment is performed the results would be slightly different. Especially for aero-elastic behavior where the response is not only dependent on the current conditions but also on the conditions leading up to any one moment. Repeat experiments can give greater confidence in the results and identify outliers. Knowing under which conditions these ”outliers” occur may also be quite valuable. Due to the nature of field experiments, an exact repeat will be impossible but may still give very useful results.

Bibliography

[1] IEC. *61400-1 Ed.3: Wind turbines - Part 1: Design requirements*. Standard. Geneva: International Electrotechnical Commission, 2005. URL: `https://webstore.iec.ch/publication/29360`.

[2] M. Stettner et al. “Stall-Induced Vibrations of the AVATAR Rotor Blade”. In: vol. 753. Institute of Physics Publishing, Oct. 2016. DOI: `10.1088/1742-6596/753/4/042019`.

[3] D. I. Manolas, P. K. Chaviaropoulos, and V. A. Riziotis. “Assessment of Vortex Induced Vibrations on wind turbines”. In: vol. 2257. Institute of Physics, May 2022. DOI: `10.1088/1742-6596/2257/1/012011`.

[4] T. Sarpkaya. “A critical review of the intrinsic nature of vortex-induced vibrations”. In: *Journal of Fluids and Structures* 19 (4 2004), pp. 389–447. ISSN: 08899746. DOI: `10.1016/j.jfluidstructs.2004.02.005`.

[5] C. M. Leong and T. Wei. “Two-degree-of-freedom vortex-induced vibration of a pivoted cylinder below critical mass ratio”. In: *Proceedings of the Royal Society A: Mathematical, Physical and Engineering Sciences* 464 (2099 Nov. 2008), pp. 2907–2927. ISSN: 14712946. DOI: `10.1098/rspa.2007.0166`.

[6] C. H. K. Williamson and A. Roshko. *VORTEX FORMATION IN THE WAKE OF AN OSCILLATING CYLINDER*. 1988, pp. 355–381. DOI: `10.1016/S0889-9746(88)90058-8`.

[7] C.C. Feng. “The measurement of vortex induced effects in flow past stationary and oscillating circular and D-section cylinders”. PhD thesis. University of British Columbia, 1968. DOI: `10.14288/1.0104049`. URL: `https://open.library.ubc.ca/collections/ubctheses/831/items/1.0104049`.

[8] R. D. Blevins. *Flow-Induced Vibration*. second edition. Krieger Publishing Company, 1990. DOI: `10.1016/0894-1777(91)90027-O`.

[9] G. Arioli and F. Gazzola. “Torsional instability in suspension bridges: The Tacoma Narrows Bridge case”. In: *Communications in Nonlinear Science and Numerical Simulation* 42 (Jan. 2017), pp. 342–357. ISSN: 10075704. DOI: `10.1016/j.cnsns.2016.05.028`.

[10] F. Weber and M. Maślanka. “Frequency and damping adaptation of a TMD with controlled MR damper”. In: *Smart Materials and Structures* 21 (5 May 2012). ISSN: 09641726. DOI: `10.1088/0964-1726/21/5/055011`.

[11] J.-W. Seo et al. “Interference effect on vortex-induced vibration in a parallel twin cable-stayed bridge”. In: *Journal of Wind Engineering and Industrial Aerodynamics* 116 (2013), pp. 7–20. ISSN: 01676105. DOI: `10.1016/j.jweia.2013.01.014`.

[12] L. Zhao et al. “A fast on-site measure-analyze-suppress response to control vortex-induced-vibration of a long-span bridge”. In: *Structures* 35 (Jan. 2022), pp. 192–201. ISSN: 23520124. DOI: `10.1016/j.istruc.2021.10.017`.

[13] M. Jafari and A. Alipour. *Methodologies to mitigate wind-induced vibration of tall buildings: A state-of-the-art review*. Jan. 2021. DOI: `10.1016/j.jobe.2020.101582`.

[14] A. Kareem, T. Kijewski, and Y. Tamura. “Mitigation of motions of tall buildings with specific examples of recent applications”. In: *Wind and Structures, An International Journal* 2 (3 1999), pp. 201–251. ISSN: 12266116. DOI: `10.12989/was.1999.2.3.201`.

[15] K. Zhou, J.-W. Zhang, and Q.-S. Li. “Control performance of active tuned mass damper for mitigating wind-induced vibrations of a 600-m-tall skyscraper”. In: *Journal of Building Engineering* 45 (Jan. 2022). ISSN: 23527102. DOI: `10.1016/j.jobe.2021.103646`.

[16] J. T. Petersen et al. *Prediction of Dynamic Loads and Induced Vibrations in Stall.* Risø National Laboratory, 1998. URL: https://orbit.dtu.dk/en/publications/prediction-of-dynamic-loads-and-induced-vibrations-in-stall.

[17] F. Zou et al. "Analysis of vortex-induced and stall-induced vibrations at standstill conditions using a free wake aerodynamic code". In: *Wind Energy* 18 (12 Dec. 2015), pp. 2145–2169. ISSN: 10991824. DOI: 10.1002/we.1811.

[18] W. A. Timmer. "Aerodynamic characteristics of wind turbine blade airfoils at high angles-of-attack". In: *TORQUE* (2010). URL: http://resolver.tudelft.nl/uuid:7bc4ac3e-46d6-4113-8b47-2893ab0fe88e.

[19] M. H. Hansen. "Aeroelastic instability problems for wind turbines". In: *Wind Energy* 10 (6 2007), pp. 551–577. ISSN: 10991824. DOI: 10.1002/we.242.

[20] J. G. Holierhoek. "Aeroelasticity of large wind turbines." 2008. ISBN: 9789090236278. URL: http://resolver.tudelft.nl/uuid:6258fd96-2f6f-4cda-9c4a-a6dc7d981185.

[21] M. A. Khan et al. "Spectral analysis of New MEXICO standstill measurements to investigate vortex shedding in deep stall". In: *Wind Energy* 23 (1 Jan. 2020), pp. 31–44. ISSN: 10991824. DOI: 10.1002/we.2409.

[22] C. Chen et al. "Stall-induced vibrations analysis and mitigation of a wind turbine rotor at idling state: Theory and experiment". In: *Renewable Energy* 187 (Mar. 2022), pp. 710–727. ISSN: 18790682. DOI: 10.1016/j.renene.2022.01.078.

[23] P.K. Chaviaropoulos et al. *Stability analysis of parked wind turbine blades.* 2009. URL: https://www.researchgate.net/publication/229053423.

[24] A. Pellegrino and C. Meskell. "Vortex shedding from a wind turbine blade section at high angles of attack". In: *Journal of Wind Engineering and Industrial Aerodynamics* 121 (2013), pp. 131–137. ISSN: 01676105. DOI: 10.1016/j.jweia.2013.08.002.

[25] W. Skrzypiński et al. "Vortex-induced vibrations of a DU96-W-180 airfoil at 90° angle of attack". In: *Wind Energy* 17 (10 2014), pp. 1495–1514. ISSN: 10991824. DOI: 10.1002/we.1647.

[26] C. Grinderslev et al. "Forced-motion simulations of vortex-induced vibrations of wind turbine blades – a study of sensitivities". In: *Wind Energy Science* 8.10 (2023), pp. 1625–1638. DOI: 10.5194/wes-8-1625-2023.

[27] J.C. Heinz et al. "Vortex-induced vibrations on a modern wind turbine blade". In: *Wind Energy* 19 (11 Nov. 2016), pp. 2041–2051. ISSN: 10991824. DOI: 10.1002/we.1967.

[28] S.G. Horcas et al. "Suppressing Vortex Induced Vibrations of Wind Turbine Blades with Flaps". In: *Recent Advances in CFD for Wind and Tidal Offshore Turbines* (2019), pp. 11–24. DOI: 10.1007/978-3-030-11887-7_2.

[29] S. G. Horcas et al. "Vortex induced vibrations of wind turbine blades: Influence of the tip geometry". In: *Physics of Fluids* 32 (6 June 2020). ISSN: 10897666. DOI: 10.1063/5.0004005.

[30] S. G. Horcas et al. "Vibrations of wind turbine blades in standstill: Mapping the influence of the inflow angles". In: *Physics of Fluids* 34.5 (2022), p. 054105. DOI: 10.1063/5.0088036.

[31] Chandramouli Santhanam, Riccardo Riva, and Torben Knudsen. "Surrogate models for predicting stall-induced vibrations on wind turbine blades". In: vol. 2265. Institute of Physics, June 2022. DOI: 10.1088/1742-6596/2265/3/032005.

[32] C. Lindenburg and J.G. Schepers. *PHATAS-III aeroelastic modelling. Program for Horizontal Axis wind Turbine Analysis and Simulation version III.* July 1996. URL: https://www.osti.gov/etdeweb/biblio/371342.

[33] K. Boorsma et al. *Final Report of IEA Wind Task 29 Mexnext (Phase 3).* 2018. URL: http://resolver.tudelft.nl/uuid:251f749d-41dc-4091-a6fa-08704eae2bab.

[34] P. Bortolotti et al. *IEA Wind TCP Task 37: Systems Engineering in Wind Energy - WP2.1 Reference Wind Turbines.* NREL, 2019. DOI: 10.2172/1529216.

[35] LM Wind Power: WMC Laboratories. *Focus 6.* 2006. URL: https://www.wmc.eu/focus6.php.

[36] K. Boorsma, F. Grasso, and J. G. Holierhoek. *Enhanced approach for simulation of rotor aerodynamic loads.* Energy Research Center of the Netherlands, ECN-M-12-003, 2012. URL: https://api.semanticscholar.org/CorpusID:181613115.

[37] D. Winkelaar. *SWIFT Program for Three-dimensional Wind Simulation. Pt. 1. Model Description and Program Verification*. ECN, 1992. URL: `https://books.google.nl/books?id=MDUUnQEACAAJ`.

[38] T. Burton et al. *Wind energy handbook*. Third edition. John Wiley & Sons, Inc., 2021. DOI: `10.1002/9781119992714`.

[39] L. Prandtl. *Applications of modern hydrodynamics to aeronautics (Technical report No. 116)*. National Advisory Committee for Aeronautics (NACA), 1921. URL: `https://ntrs.nasa.gov/citations/19930091180`.

[40] J.G. Schepers. "An engineering model for yawed conditions developed on basis of wind tunnel measurements." In: Jan. 1999. DOI: `10.2514/6.1999-39`.

[41] H. Snel and J.G. Schepers. *Joule1: Joint investigation of dynamic inflow effects and implementation of an engineering model*. ECN, 1995. URL: `https://publicaties.ecn.nl/PdfFetch.aspx?nr=ECN-C--94-107`.

[42] H. Snel. "Heuristic modelling of dynamic stall characteristics". In: *Conference proceedings European Wind Energy Conference*. 1997, pp. 429–433.

[43] K. Truong. "A 2-d dynamic stall model based on a hopf bifurcation". In: *19th European rotorcraft forum*. 1993. URL: `http://hdl.handle.net/20.500.11881/2281`.

[44] N. Adema, M. Kloosterman, and G. Schepers. "Development of a second-order dynamic stall model". In: *Wind Energy Science Conference*. 2020, pp. 577–590. DOI: `10.5194/wes-5-577-2020`.

[45] J.G. Leishman and T.S. Beddoes. "A semiempirical model for dynamic stall". In: *Journal of the American Helicopter Society* (1989). DOI: `10.4050/JAHS.34.3.3`.

[46] S. Gupta and J.G. Leishman. "Dynamic stall modelling of the s809 aerofoil and comparison with experiments". In: *Wind Energy* (1989). DOI: `10.1002/we.200`.

[47] M. A. Khan. *Dynamic Stall Modeling for Wind Turbines*. TU Delft, 2018. URL: `http://resolver.tudelft.nl/uuid:f1ee9368-ca44-47ca-abe2-b816f64a564f`.

[48] J.W. Larsen, S.R.K. Nielsen, and S. Krenk. "Dynamic stall model for wind turbine airfoil". In: *Journal of Fluids and Structures* 23 (2007), pp. 577–590. ISSN: 08899746. DOI: `10.1016/j.jfluidstructs.2007.02.005`.

[49] T. Sant. "Improving BEM-based Aerodynamic Models in Wind Turbine Design Codes". 2007. ISBN: 978-99932-0-483-1. URL: `http://resolver.tudelft.nl/uuid:4d0e894c-d0ad-4983-9fa3-505a8c6869f1`.

[50] L. Pergod and E.K. Fritz. *Aeroelastic model of the TIADE turbine*. TNO, 2021.

Appendix A

Pressure sensor data from pitch traverse

This appendix shows the pressure sensor data of blade 3 which did a pitch traverse while it was aimed straight up in the sky. The red dot in the figures is the approximate location of the pressure sensor.

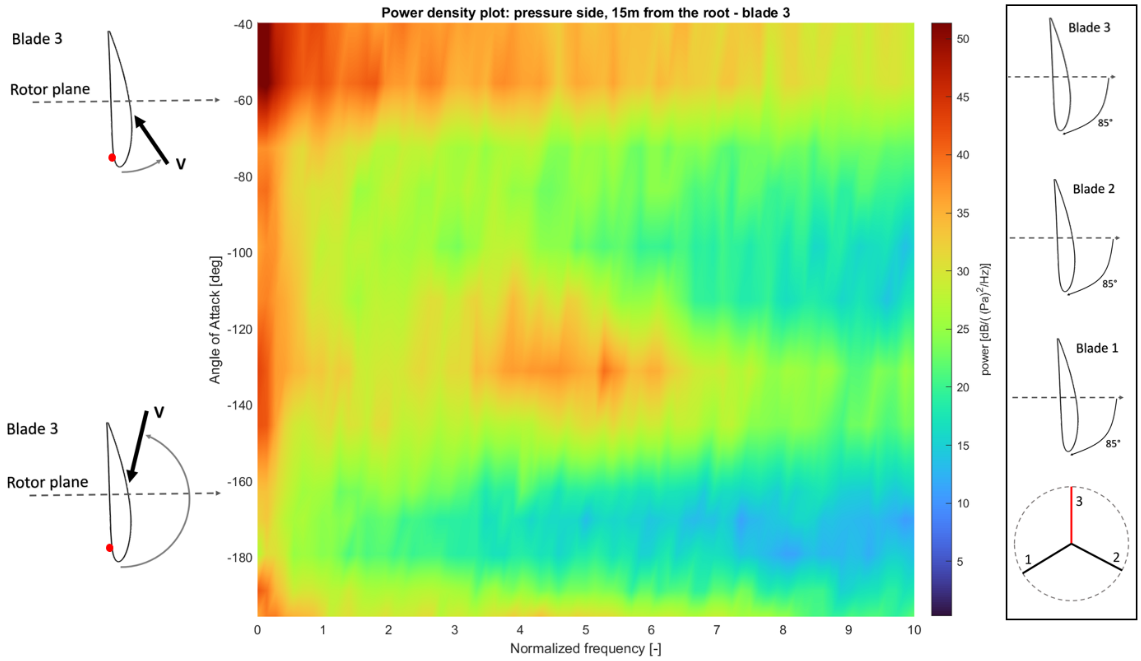

Figure A.1: PSD of the pressure fluctuations.

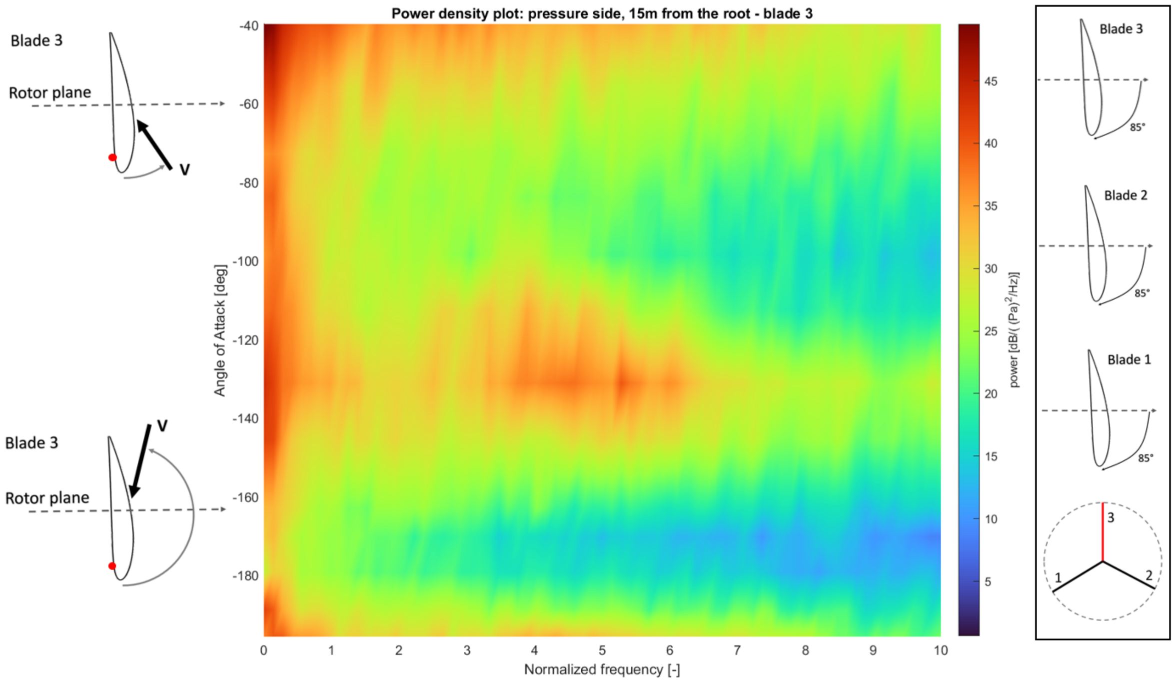

Figure A.2: PSD of the pressure fluctuations.

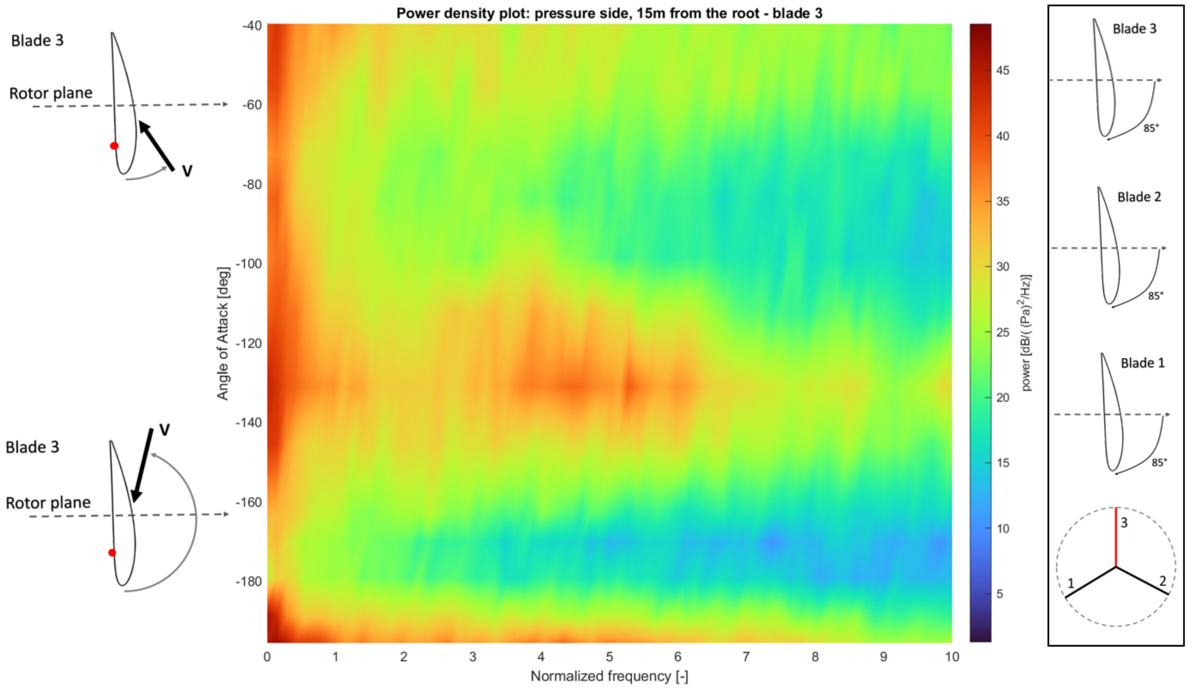

Figure A.3: PSD of the pressure fluctuations.

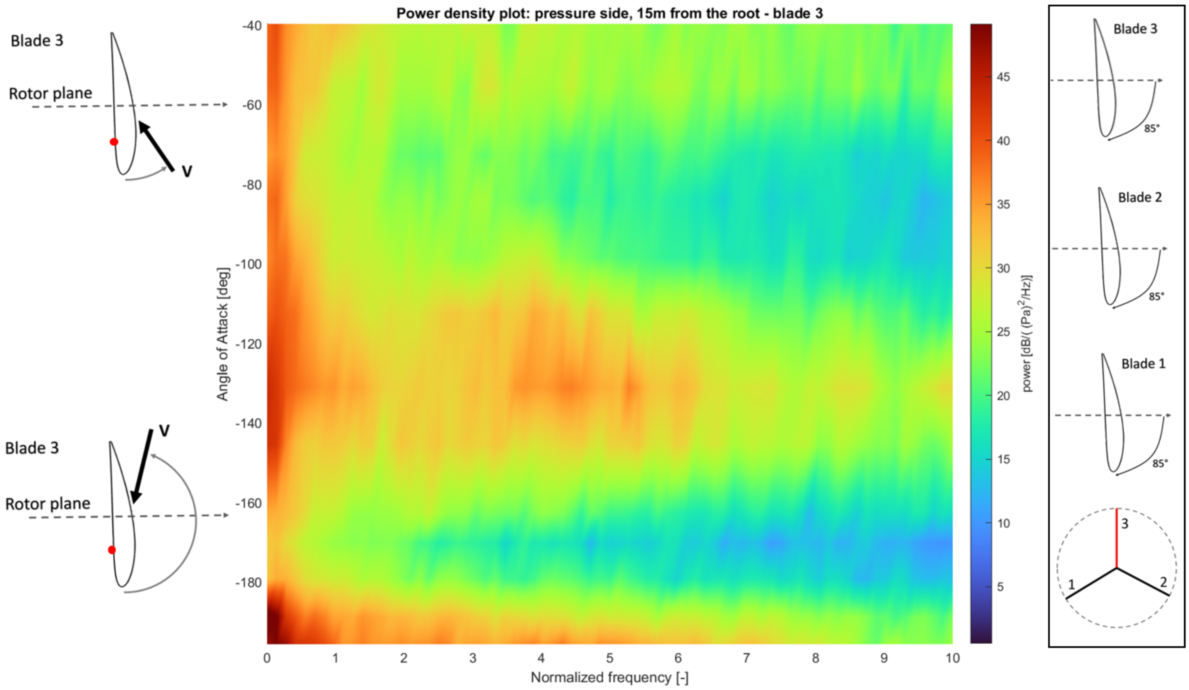

Figure A.4: PSD of the pressure fluctuations.

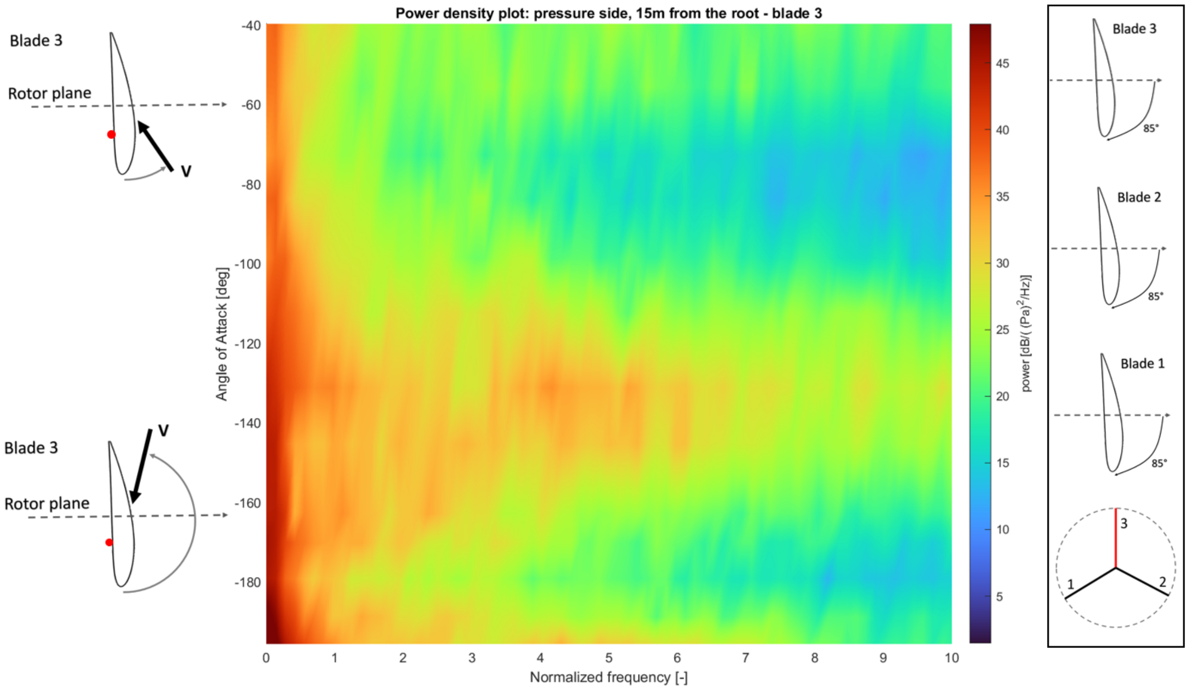

Figure A.5: PSD of the pressure fluctuations.

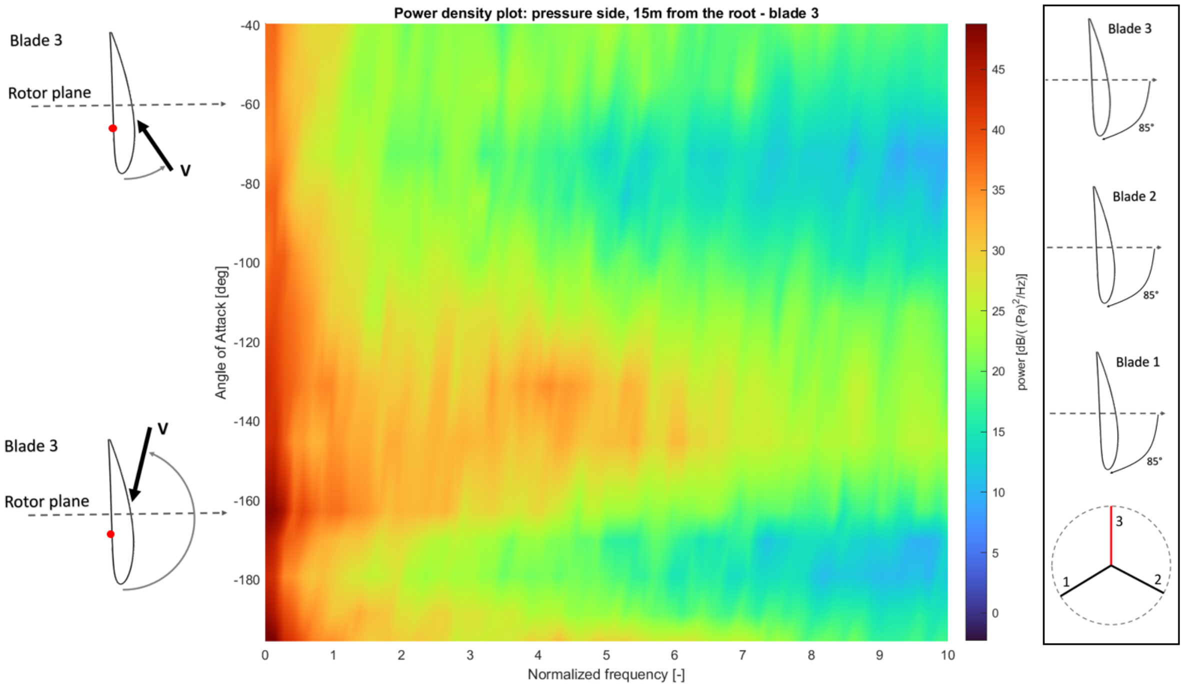

Figure A.6: PSD of the pressure fluctuations.

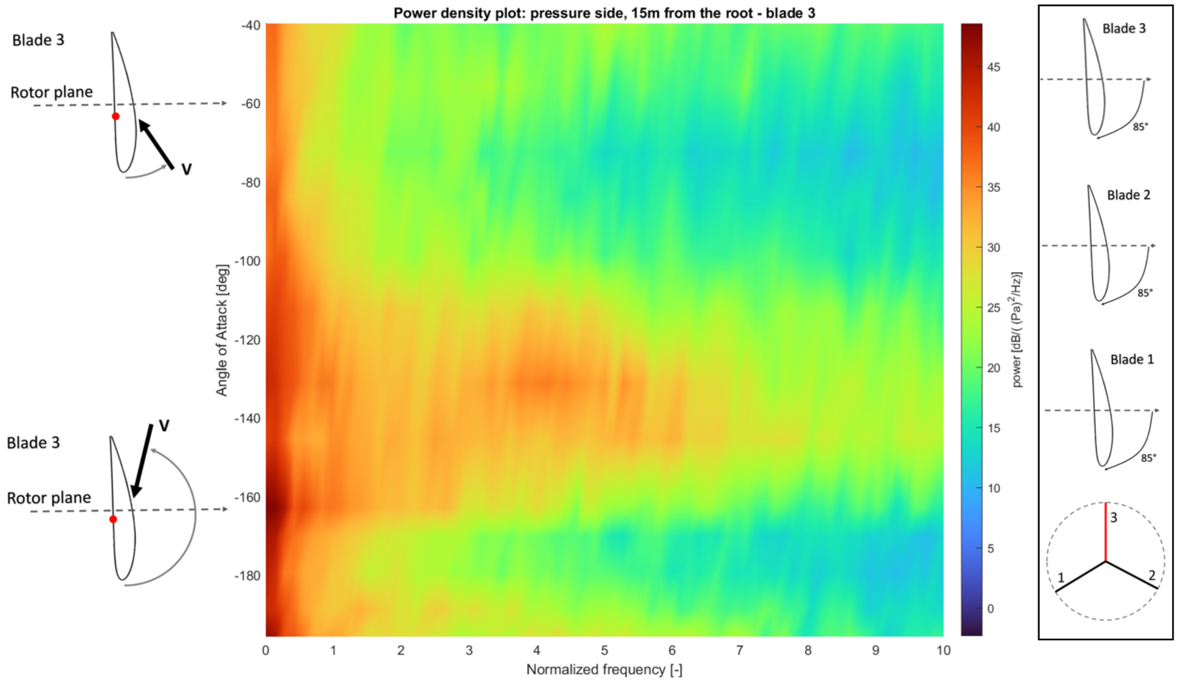

Figure A.7: PSD of the pressure fluctuations.

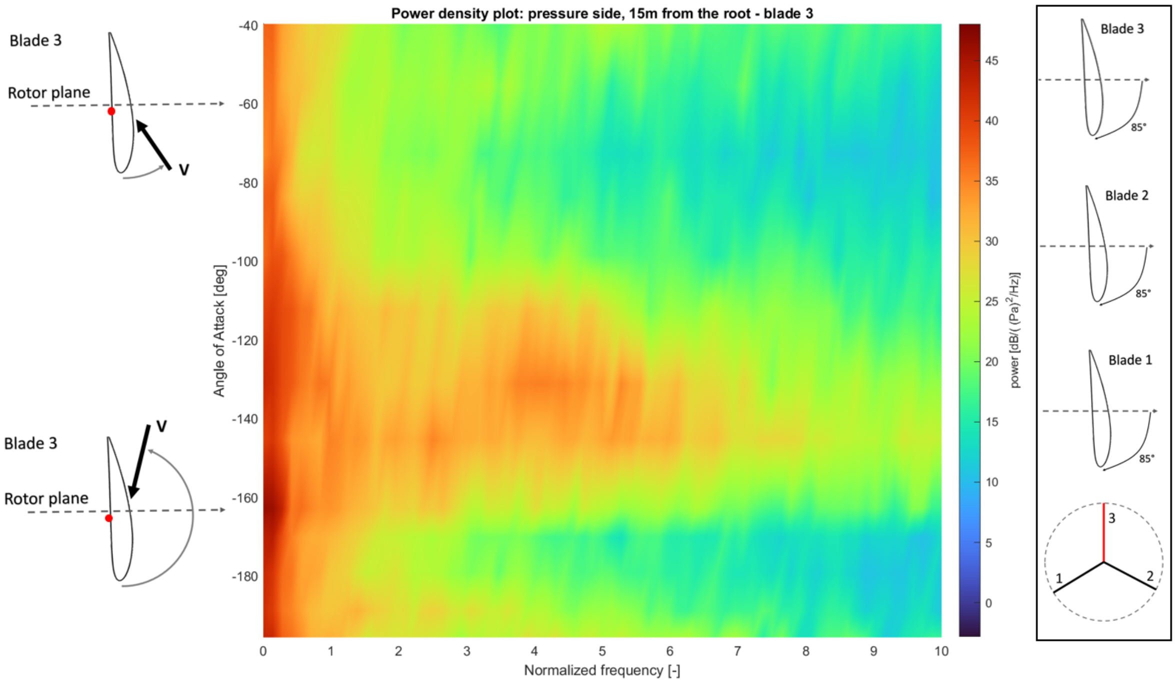

Figure A.8: PSD of the pressure fluctuations.

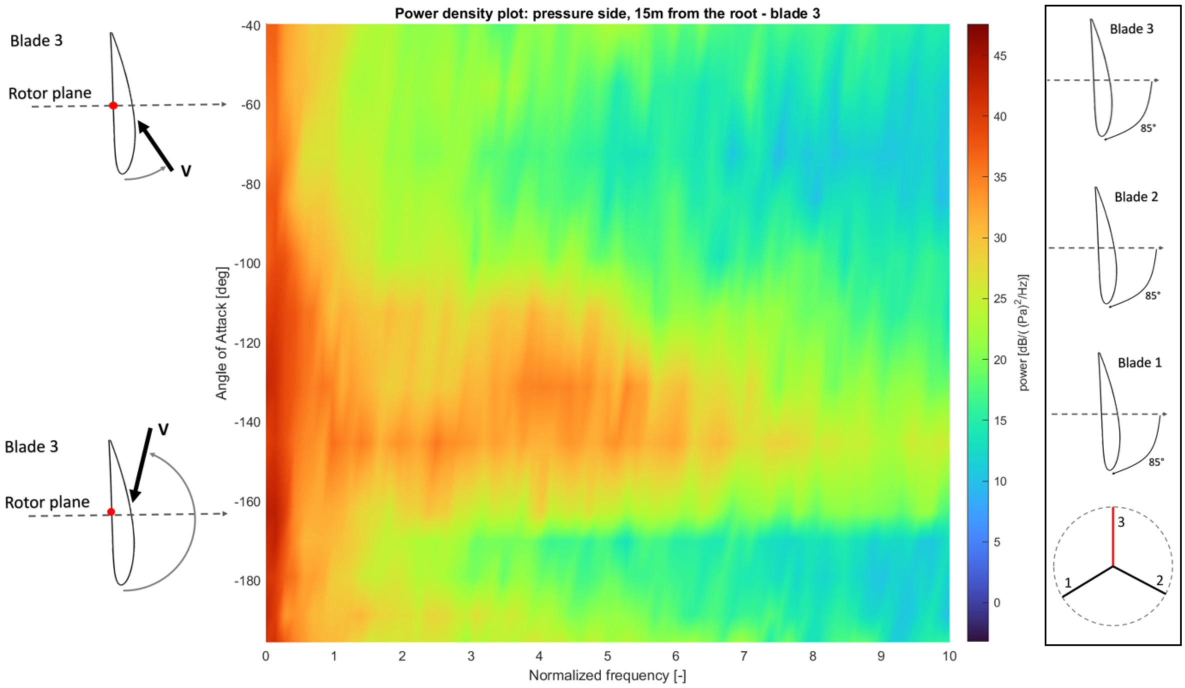

Figure A.9: PSD of the pressure fluctuations.

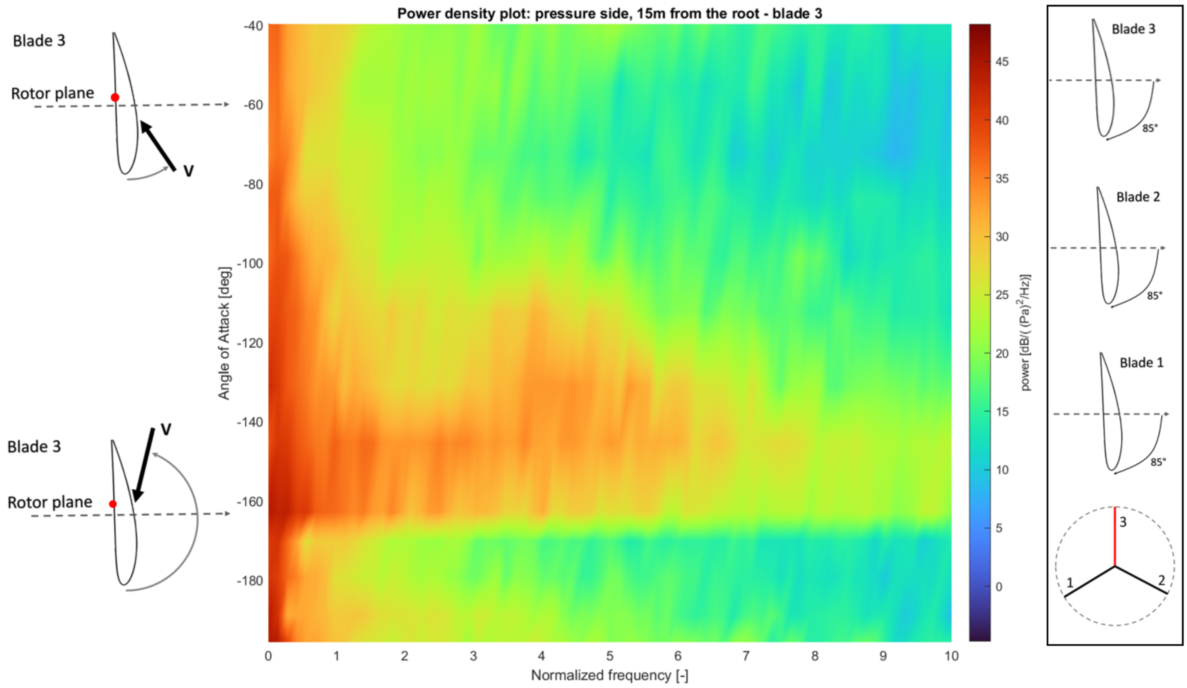

Figure A.10: PSD of the pressure fluctuations.

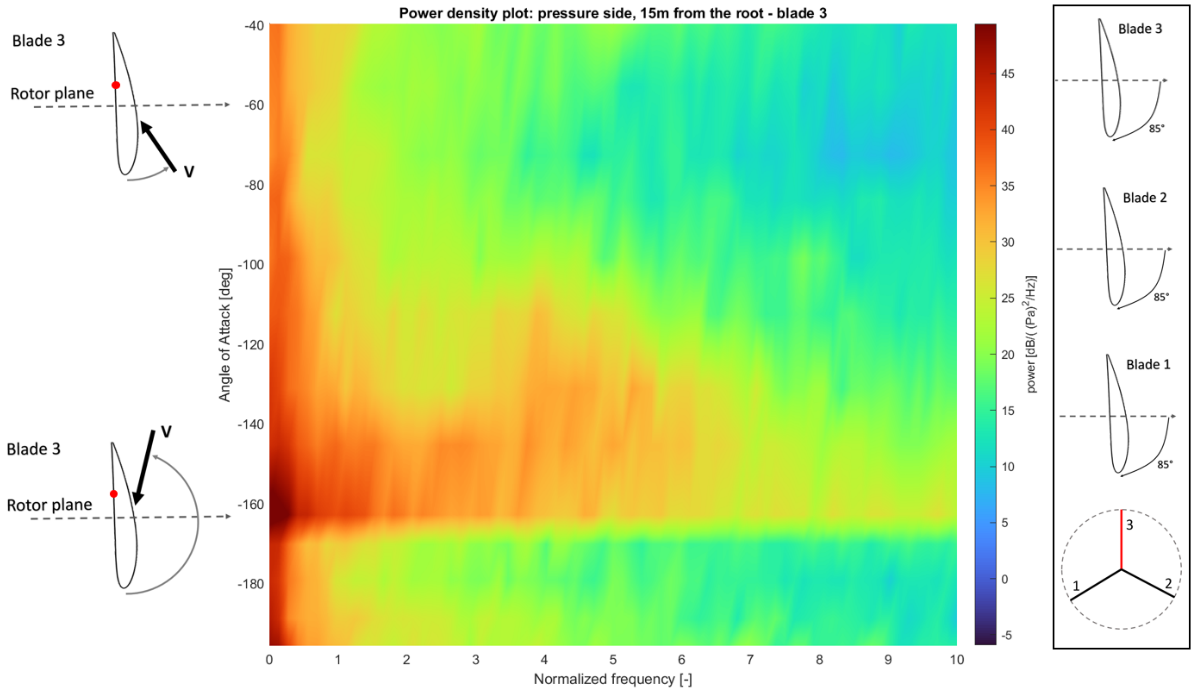

Figure A.11: PSD of the pressure fluctuations.

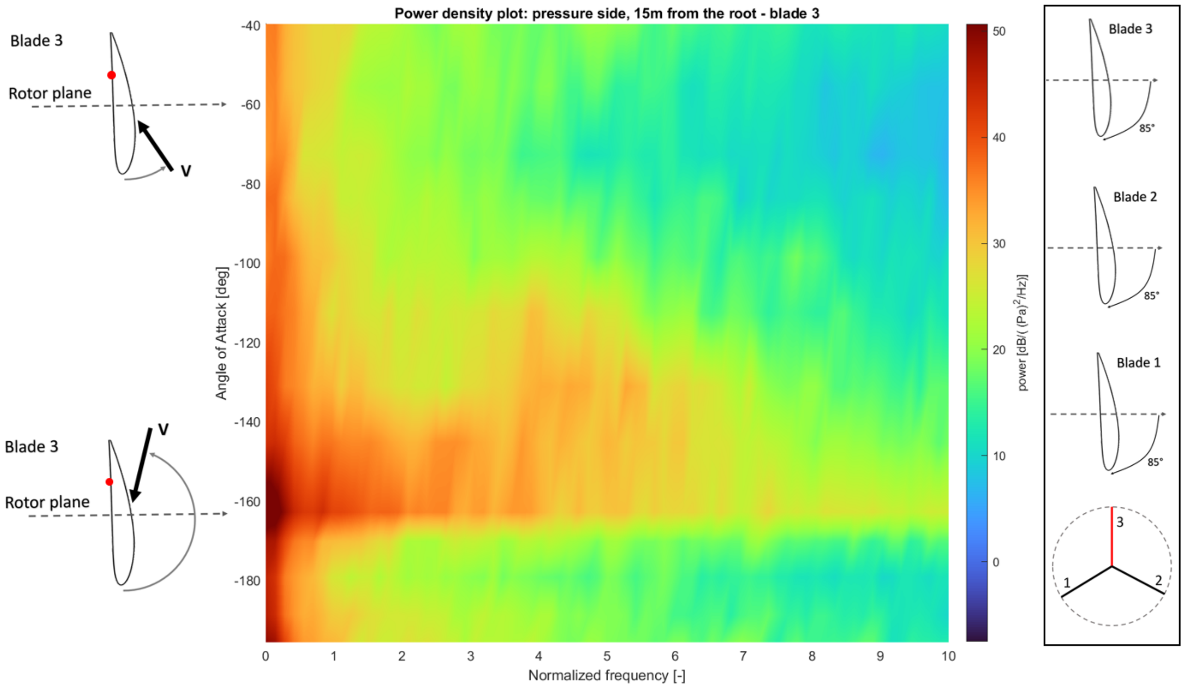

Figure A.12: PSD of the pressure fluctuations.

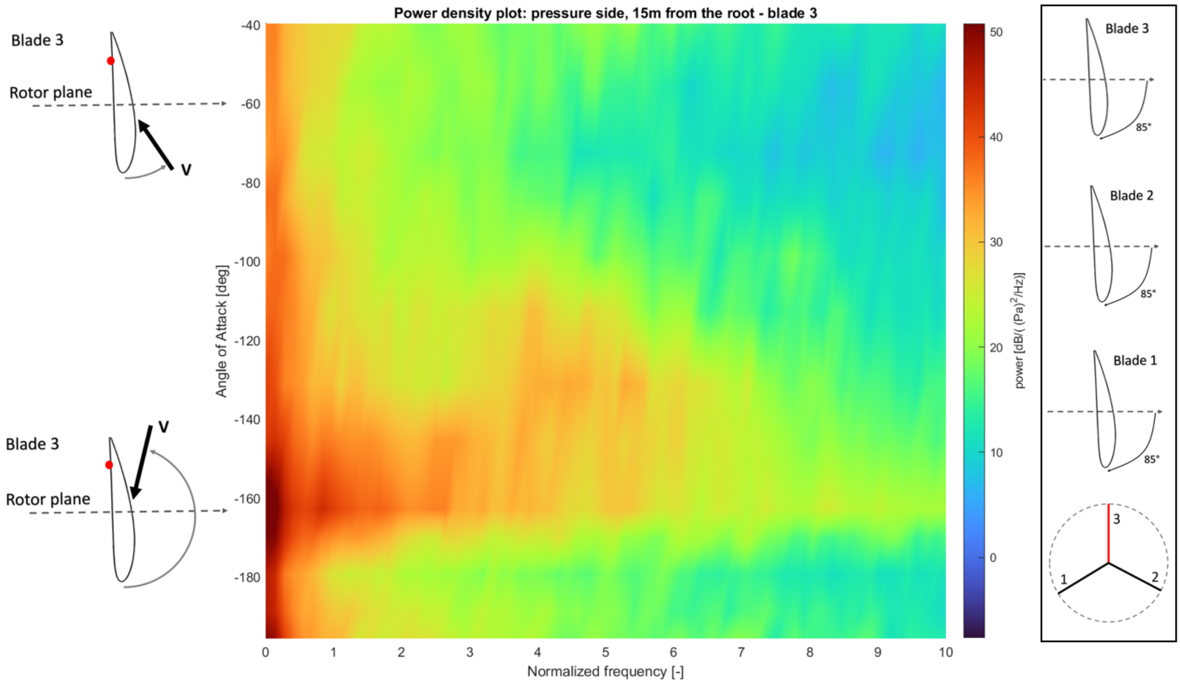

Figure A.13: PSD of the pressure fluctuations.

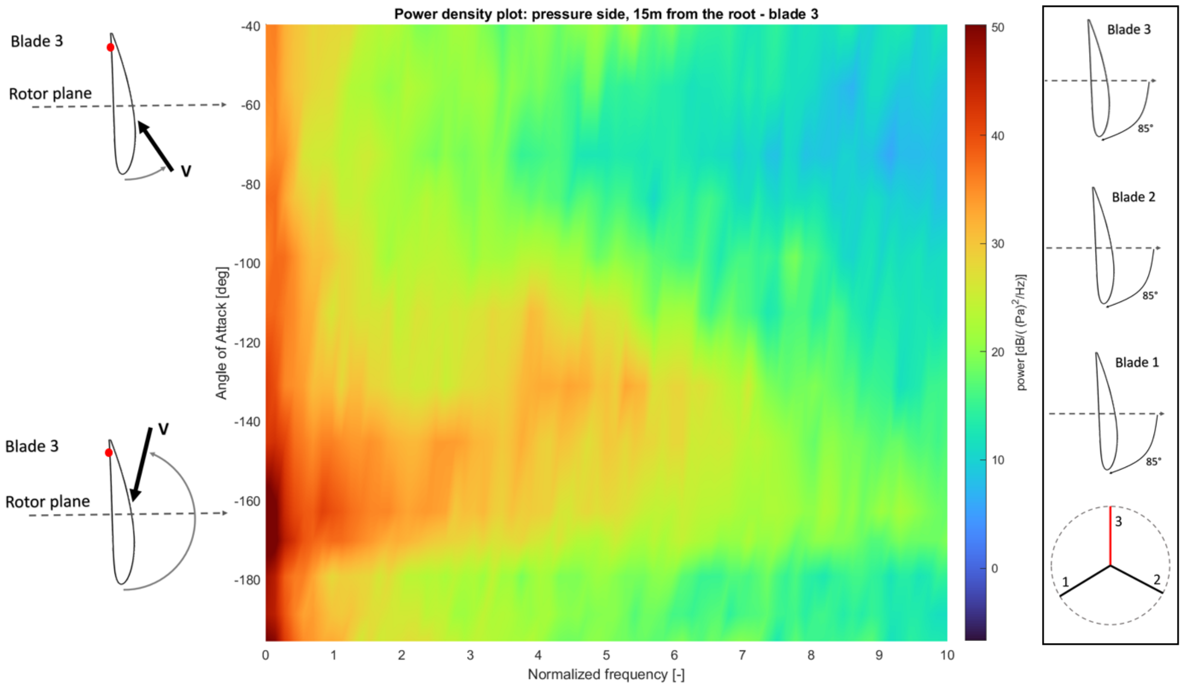

Figure A.14: PSD of the pressure fluctuations.